OLD AND NEW METHODS IN GEOMETRIC MORPHOMETRICS APPLIED TO THE STUDY OF HUMAN EVOLUTION: CASE-STUDIES

PhD thesis

Antonio Profico

Sapienza Università di Roma
Dipartimento di Biologia Ambientale
Corso di Dottorato di Ricerca in Biologia Ambientale ed Evoluzionistica
XXVIII Ciclo

A Dario

Contents

Abbreviations

CS	Centroid Size
GM	Geometric Morphometrics
PCA	Principal Components Analysis
PCs	Principal Components scores
TPS	Thin-Plate Spline
CT	Computerized Tomography

List of the Figures and Tables:

1 Introduction

Abstract

The main aim of this thesis is the application of Geometric Morphometric methods on different case-studies for the study of human evolution. When combined with techniques of acquisition of 3D models, Geometric Morphometrics allows us:

- to investigate different experimental designs;
- to analyse the interaction of several aspects on morphological adaptations detected within taxon-specific studies (e.g., allometry, phylogenetic signal, functional factors);
- to study fragmentary fossils and incomplete specimens, through estimation of missing data and 3D virtual restoration (e.g., surface and curve slid semilandmark);
- to plan, code and test new algorithms and/or methodological approaches.

The first part deals with the use of smoothing filters applied to 3D model for Geometric Morphometric studies. These algorithms are used to remove the background noise deriving from digital acquisition (e.g., photogrammetry, laser scan and computerized tomography scan). The effects of the different smoothing filters have been assessed. In particular have been defined guidelines for a correct use of these algorithms, besides the developing of an automatized tool, in R environment, to find the best combination between algorithm type, settings and number of iterations.
The second part consists of a protocol developed, with the collaboration of the University of Freiburg, for the digital retrodeformation of fossil specimens showing evidence of shearing, bending and compressing alterations due to taphonomic processes. Traditional methods of retrodeformation only use a sparse set of bilateral landmarks; the number of points appears to affects the success of retrodeformation. On the contrary, this method uses, in addition to the landmark configurations, the curve and surface semilandmarks, which allow us to capture morphological information more accurately. This protocol was applied here to the neanderthalian cranium of Saccopastore 1.
The third part reports the results of the first analysis on the specimen nicknamed "Pàus" (St.n.166623), recently discovered near Spinadesco in the Po Valley (Northern Italy). A set of 100 semilandmarks was built on the specimen and slid, using a set of 6 landmark, on a comparative sample including specimens dated to the Middle-to-Late Pleistocene. The results show how the morphology of "Pàus" is consistent with the variability observed in the Neanderthal lineage.
The fourth part concerns a Geometric Morphometric investigation performed on two human cranial fossil remains from Melka Kunture, dated to about 850 ka. The two cranial fragments consist in a partial left parietal (MK73/GOM II- 6769; formally Melka Kunture 1, or MK1) and a right portion of the frontal bone (MK76/GOM II - 576, or MK2). Specifically, evenly-spaced semilandmark sets were used acquired along the sagittal suture and the inferior temporal line on MK1 and MK2 respectively. The results of the analyses, in agreement with the chronology of the fossils, represent at present, evidence of one of the best candidates to be the most ancient example of *H. heidelbergensis*.
The fifth part treats with the external morphology of the cranial base in extant and living Hominoids in relation to ontogenetic, allometric, locomotor and phylogenetic factors. The sample selected consists of 3D landmark configurations acquired on specimens (male and female) including infant, sub-adult and adult individuals. The centroid size of the landmark set configuration was used as indicator of size while the pattern of dental eruption (at death) was used to define six age groups. The relation between morphology and locomotion was explored through the estimation of the position of the foramen magnum along the Frankfurt plane. Finally, a phylogenetic tree was build using molecular and paleontological data, with the phylogenetic signal investigated through centroid size and shape.

1.1 General framework

Thanks to improvements in both computer technology and 3D imaging techniques is possible to virtually acquire the morphology of a physical specimen (Bates, et al., 2010, Falkingham, 2012). Consequently, paleoanthropological studies often focused on anatomy, virtual reconstruction and on the development of algorithms to improve the digital acquisition (Cunningham, et al., 2014). In addition to CT scan other techniques have been introduced, such as laser scanner and photogrammetry. These methodologies allow to acquire only the external surface of an object but they require less expensive technical equipment (Friess, 2012), making digital acquisition possible despite the absence of very expensive tools. The increased availability of these methods in evolutionary biology studies have led to the emergence of virtual museums (e.g. Smithsonian museum, Kupri, Nespos, Digimorph, Morphosource) providing the use of large and worldwide comparison sample (Gilissen, 2009, Niven, et al., 2009). A digital comparative sample consists of 3D models of different resolution (intended as number of vertices) and quality, and a good practice is to uniform the resolution of 3D sample through a mesh decimation (Kobbelt, et al., 1998). Smoothing filters can be applied to reorganize the 3D geometrical structure, and several 3D imaging software (e.g., Amira, Avizo, Mimics, Geomagic Studio) have been embedded smoothing algorithms among their options. The smoothing filters are often applied, especially in 3D objects obtained by manual segmentation (e.g., Macrini, et al., 2007) of virtual cavity (e.g., endocast) where topological inaccuracies and artefacts occur frequently. In this thesis the first critical assessment on the effect of smoothing algorithms is reported, and a tool (developed in R environment Venables and Smith (2010)) is provided; the tool is designed to find the optimal combination of smoothing parameters for a specific 3D model.

The 3D imaging techniques allow to substitute a physical intervention with a virtual protocol aimed at restoring the original shape of a fossil specimen (Lyman, 1994, Shipman, 1981), guarantying at the same time the preservation of the fossil and the reparation of possible damages. Recently, palaeoanthropology benefited the contribution of new methodological approaches in studying shape and morphology, foremost GM. This methodology requires to approximate the shape of biological objects by defining and acquiring anatomical (landmarks) and geometrical points (semilandmarks) (Gunz, et al., 2005).

The GM approach is based on the concept of geometrical/anatomical "homology" meant as correspondence between two related forms in accord with ontogenetic or phylogenetic criteria (Bookstein, 1982). The biological configurations in related specimens are acquired as a series of "points" (landmarks) presumed to be "homologous" and comparable in all their histological and topological characteristics (Bookstein, 1978). In "The Measurement of Biological Shape and Shape Change" Bookstein distinguishes between "extremal" and "anatomical" landmarks: the former refers to geometrical points (points that mark maximum lengths, or points of maximal curvature), the latter refers to anatomical homologous "points" (Bookstein, 1978). Landmarks can be subdivided into three categories type 1 are discrete juxtapositions of tissue including points in space at which three structures meet; type 2 are points of

maximal curvature or other local morphogenetic processes, including tips of extrusions and valleys of invaginations; type 3 are defined as extremes of curvature of points furthest along (or away from) some structure (Bookstein, 1997b). Bookstein resumes the aims of the GM enunciating four principles (Bookstein, 1997b):

- ✓ **Landmark locations**; this concept is fundamental to assure the repeatability of the sampling procedure, determining an accurate definition.
- ✓ **Shape coordinates**; measurements of the shapes of configurations of landmark locations reduces to multiple vectors of shape coordinates. These come in pairs that represent the shape of one triangle of landmarks in a manner completely independent of size.
- ✓ **The form of questions;** submitting shape coordinates to multivariate analysis is possible to detect morphological variation between and within groups, effects of growth or age or size difference upon form.
- ✓ **The form of answers**; the results of a data analysis will exploit using several different diagrams each of which corresponds to one part of the covariance reported by a single statistical analysis.

GM can be applied to correct the asymmetry due to taphonomic events in the virtual restoration of digital models. GM protocols exploit the acquisition of two bilateral landmark sets on a specimen to extrapolate the geometrical pattern of asymmetry. Two bilateral configurations can be symmetrized (Klingenberg, et al., 2002) and the digital specimen can be forced to follow the new constraint, intended as landmark symmetrisation, through the application of TPS (Bookstein, 1989) and surface warping algorithms (Mark, et al., 1997): this procedure is usually referred to as retrodeformation. So far, the protocols published are based on the use of landmarks only and consequently the success of the procedure of retrodeformation is strictly dependent on the number of acquirable landmarks and on the state of preservation of the deformed specimen (Ghosh, et al., 2010, Tallman, et al., 2014). Another critical point is the presence of different landmark "densities" in different anatomical districts (e.g., more landmarks on the facial and cranial base regions than on the neurocranium). Thanks to the collaboration between the Laboratory of Palaeoanthropology and Bio-Archaeology (Sapienza University in Rome) and the University of Freiburg a new protocol for correcting for asymmetry has been defined, using landmark sets but also curves semilandmark and semilandmark sets. In this way, it a more accurate detection of the pattern of asymmetry is guaranteed, allowing a more precise retrodeformation procedure. In this thesis has been reported the application of this protocol, which has been recently developed using the neanderthalian skull of Saccopastore 1 and collecting 88 bilateral landmarks (44 on each side), 6 semilandmark curves (140 semilandmark) and 10 semilandmark patches (438 semilandmark), for a total of 666 anatomical/geometrical points (333 on each side).

The application of GM methods are used in this thesis to study the morphology of two cranial remains. The first, named Pàus, consists of the almost complete frontal bone of an adult individual, found on a sand bar of the left bank of the river, probably carried by the current from the upstream Middle-Late Pleistocene deposits (Profico, et al., 2015). The Pàus specimen is been studied through a multidisciplinary approach: ancient DNA, dating and morphology. In this thesis the results of shape analysis performed on Pàus are reported. Pàus has been studied using a comparative sample inclusive of specimens belonging to *Homo ergaster*, *Homo erectus*, *Homo heidelbergensis*, *Homo neanderthalensis* and *Homo sapiens*. The methodologies used consist of 3D slided Bèzier curves and semilandmark sets.

The second specimen studied is the cranial remains found in Melka Kunture (Ethiopia). The human remains consist of a partial right frontal bone (MK2) and a partial left parietal bone (MK1) (Chavaillon, et al., 1974, Chavaillon and Coppens, 1975). Both cranial fragments have been studied defining two sets of evenly-spaced semilandmark on the studied specimen and a comparative sample consisting of specimens belonging to *Homo ergaster*, *Homo erectus*, *Homo heidelbergensis*, *Homo neanderthalensis* and *Homo sapiens* species.

Besides the studies of digital restoration and of morphological/evolutionary contextualization of human remains, many researches focused on phenomena and adaptations that have characterized the evolution of the genus *Homo*. One of the most fascinating and studied to date is the morphology of the skull base. This district is articulated to the post-cranium and is functionally linked to the locomotor habits and adaptations. The early representatives of the Hominin clade (7 to 4 Ma approximately) possess few features that indicate bipedalism. The locomotor habit of the genus *Australopithecus* is commonly referred to facultative bipedalism, while that of the genus *Homo* to obligated bipedalism (Harcourt-Smith, 2016)

The study of the cranial base district plays a central role in the understanding the evolution of the genus *Homo* (Dean and Wood, 1984; Kimbel and Rak, 2010; Kimbel et al., 2014; Lieberman et al., 2000a; Lieberman et al., 2000b). Following the discovery of Taung's child (Dart, 1925), the cranial base morphology and the relative foramen magnum position were recognized as key factors in the evolution of bipedalism (Ahern, 2005, Ashton and Zuckerman, 1956, Biegert, 1963, Luboga and Wood, 1990). In this study, the morphology of cranial base of extant and fossil Hominoidea was studied by applying methods of geometric morphometry and multivariate analysis. In addition, in this study we calculated the central position of the foramen magnum along the mid-sagittal profile of the skull (oriented on the Frankfurt plane), in order to quantify the relationship between the morphology of the skull base and the position of the foramen magnum in an ontogenetic and evolutionary perspective. Finally, the overall shape variation on cranial base was related to allometric, functional and phylogenetic factors.

2 Methodological approaches

2.1 "R" environment and "ctrlR" package installing

In this thesis the statistical analyses were performed in R environment using packages published on CRAN (https://cran.r-project.org/) and code programmed to specific analyses and methodological approaches. Functions wrote in R (license gplv3) are stored in the R packages ("ctrlR") including data and code demos. The accessibility to the functions and data allows replicating the results illustrated in the various sections and at the same time permitting the implementation of the method.

The first step is the R package installing stored on the GitHub web platform (https://github.com/Arothron/ctrlR/).

```
require(devtools)
install_github("arothron/ctrlR", local=FALSE)
library(ctrlR)
```

The package contains R functions, demos and data (Table 2.1.1).

Table 2.1.1: List of R functions, demos and data stored in the "ctrlR" package.

Name	Description	Author
R functions stored in the ctrlR Package		
aro.clo.points	This function finds the vertices numbering nearest a landmark set	Profico A. & Veneziano A.
aro.smooth.tool	This function finds the optimal smoothing algorithm setting giving a mesh a landmark set and a semilandmark set.	Profico A., Veneziano A., Lanteri A. & Piras P.
bèzier.amira.path	This function find npoints evenly spaced from a surface path (ascii format) from Amira	Profico A.
bèzier .amira.set	This function find npoints evenly spaced from a landmark file set (.landmarkAscii)	Profico A.
Conte	Internal function	Julien Claude
dec.curve	This function find and order a series of intermediate points	Profico A.
export_amira	This function export a list of 3D landmark set in separate files (format landmarkAscii)	Profico A. & Veneziano A.
fingerprint.smooth	This function print the algorithm smooth fingerprint on an added mesh noise	Profico A.
imagematrix	Internal function	Nikon Digital Technologies
iter.one2four	This repeat iteratively the function one2four	Profico A.
landmark.addition	Internal function	Julien Claude
lista.amira.dir	This function create a list formed by files of landmark set of Amira stored in a folder	Profico A.

Name	Description	Author
mesh.smooth.tool	This function find the optimal smoothing algorithm setting giving a mesh using the mesh distance as estimator.	Profico A.
noise.mesh	This function add noise to a mesh	Profico A.
one2four	This function divide a mesh in 4 parts	Profico A.
order.open.outline	This function order an outline along the xz plane and eventually convert it in 2 dimensions	Profico A.
plot.imagematrix	Internal function	Julien Claude
read.amira.dir	This function read and store in array the coordinated allocated in a folder in separate files (.landmarkAscii)	Profico A.
read.amira.set	This function convert a file landmark set of Amira (.landmarkAscii) in a array	Profico A.
read.path.amira	This function extract and order the coordinate matrix from a surface path file deriving from Amira	Profico A.
regularradius	Internal function	Julien Claude
R Data		
chimera.mesh	Mesh of a *Homo heidelbergensis* chimera	Profico A.
chimera.set	Set on the chimera.mesh	Profico A.
chimera.SL.set	Semilandmark set on the chimera.mesh	Profico A.
exp.dog.Lset	Set on the exp.dog.mesh	Profico A.
exp.dog.mesh	Mesh of a dog model	Profico A.
exp.dog.SL.set	Semilandmark set on the exp.dog.mesh	Profico A.
exp.SCP1.Lset	Set on the exp.SCP1.mesh	Profico A.
exp.SCP1.mesh	Mesh of the cranium of Saccopastore 1	Profico A.
exp.SCP1.SLset	Semilandmark set on the exp.SCP1.mesh	Profico A.
exp.teeth.Lset	Set on the exp.teeth.mesh	Profico A.
exp.teeth.mesh	Mesh of a human tooth	Profico A.
exp.teeth.SLset	Semilandmark set on the exp.teeth.mesh	Profico A.
exp.venus.mesh	Mesh of the Venus of Willendorf	Profico A.
frankfurt.pan	Landmark set defining the Frankfurt plane of the pan.model.mesh	Profico A.
pan.landmark.type	Landmark type shown on the pan.model.mesh	Profico A.
pan.model.mesh	Mesh of a specimen of *Pan troglodytes*	Profico A.
pan.model.msp	Midsagittal landmark on the pan.model.mesh	Profico A.
pan.section	Section of the pan.model.mesh (.jpg)	Profico A.

2.2 Shape analysis using outline

Outline methods in GM consist in a procedure to detect and analyse the contour of a biological object through the definition of a series of landmarks acquired along its outline. This approach is preferred when few or no landmarks are available. As introduced in the "Blue Book" (Rohlf and Bookstein, 1990) the outlines are classified in two categories: the open outlines and the closed outlines. Softwares and R packages (e.g. tpsDIG1, "Momocs" R packages) (Bonhomme, et al., 2014, Rohlf, 2015) exploit the Bèzier curves to build a curve as low as intermediate points. Once acquired the perimeter of a biological structure is possible to acquire a set of evenly-spaced landmark. The acquisition of evenly-spaced landmarks entails an issue of homology, in facts more coordinates correlates each other.

Two critical points characterized the study of the outline's shape; the method of its acquisition and the definition of geometrical/anatomical homology.

In this subchapter, we report:

- ✓ the Fourier analysis introduced by Kaesler and Waters (1972) in literature for the study of biological shapes.
- ✓ the alpha-shape hull calculation (Edelsbrunner, et al., 1983).

2.2.1 Outline definition

The Elliptic Fourier analysis developed by Kuhl and Giardina (1982) finds the Fourier coefficients of a chain-encoded contour using a harmonic to describe the outline of an object (for further details see Claude, 2008). In the "ctrlR" package there is a function to acquire an outline starting from a picture in grey scale (jpeg format). The code is a wrapper of the R packages "jpeg" and "rimage". For illustration purposes was used a section (obtained in R) on the Frankfurt plane of a 3D model of *Pan troglodytes* (fig. 2.2.1).

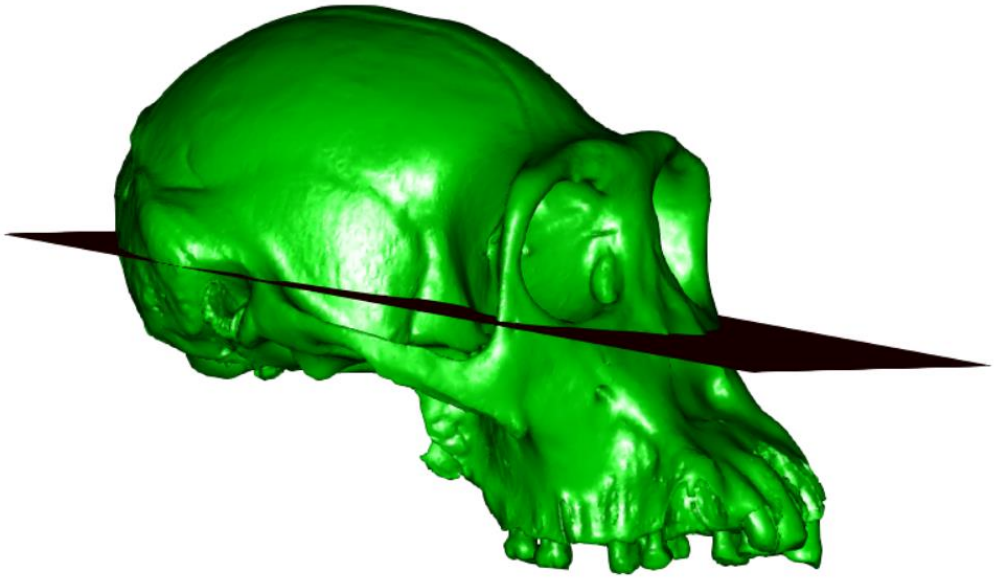

Figure 2.2.1: The section (in red) obtained, on a 3D model of *Pan troglodytes*, defined as the plane passing through the points right porion, left porion and left orbital (Frankfurt plane).

In detail, this function (`fourier.outline`) consists of the following steps:

- ✓ importing image (jpg format);
- ✓ conversion in a matrix associated to grey scale values;
- ✓ set the starting point of the outline;
- ✓ scale the outline to retrieve the raw coordinates;
- ✓ saving the outline as xy coordinates.

```
library("ctrlR")
data(pan.section)
section=section
section=cbind(1, section, 1)
section=rbind(1,section, 1)
section_junk<-imagematrix(section, type="grey")
section_junk[which(section_junk<0.95)]<-0
plot(section_junk)
cont<-Conte(round(unlist(locator(1)),0),section_junk)
scalecoord<-locator(2, type="p",pch=4,lwd=2)
scalepixsize<-sqrt(diff(scalecoord$x)^2+diff(scalecoord$y)^2)
X<-cont$X*30/scalepixsize
Y<-cont$Y*30/scalepixsize
Xc <- mean(X)
Yc <- mean(Y)
plot(X,Y,type="l")
```

The second method (function `alpha.outline`) uses a procedure based on the alpha shape calculation (Edelsbrunner, et al., 1983).

The alpha shape is a linear simple curve in the Euclidean plane associated with the shape of a set of points; in our case, the shape is the set of points resulted by the crossing of the anatomical plane to the 3D model as shown in figure 2.2.2. The method was introduced by Edelsbrunner, et al. (1983). A crucial parameter for a correct obtaining of the outline through this method is the setting of the α parameter:

- ✓ If $\alpha = 0$, it is a closed half-plane and the alpha-shape associated is its ordinary convex hull;
- ✓ If $\alpha > 0$, it is closed disk of radius $1/\alpha$;
- ✓ If $\alpha < 0$, it is the closure of the complement of a disk of radius $-1/\alpha$.

The two methods, described above, return similar results, the Fourier approach requires a ".jpeg" file as input, while the alpha.hull process requires a proper definition for alpha value. The function reported below allow obtaining 3D outline (fig. 2.2.2), in fact this function do not need a 2D object as input, but also a 3D model.

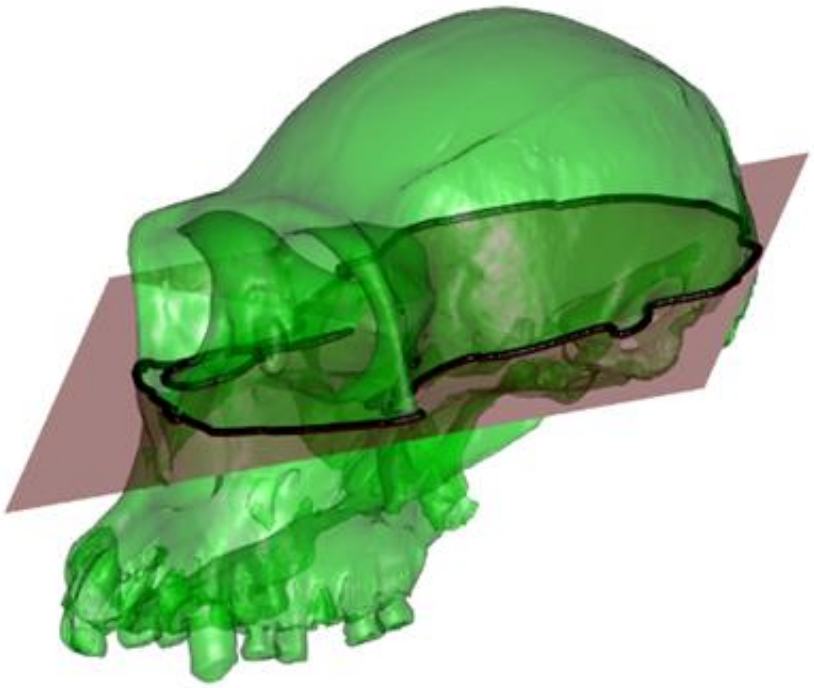

Figure 2.2.2: Are reported a 3D model of *Pan troglodytes* crossed by a plane (along the Frankfurt plane) and its 3D outline respectively.

```
library("ctrlR")
data(pan.model.mesh)
data(frankfurt.pan)
surf=pan.model.mesh
lms=frankfurt.pan
eucl=dist(lms,method="euclidean")
newP1=c(0,0,0)
newP2=c(eucl[1],0,0)
newP3=c(((eucl[1]^2)+(eucl[2]^2)-(eucl[3]^2))/(2*eucl[1]),
sqrt((eucl[2]^2)-(((eucl[1]^2)+(eucl[2]^2)-
(eucl[3]^2))/(2*eucl[1]))^2), 0)
tar=rbind(newP1,newP2,newP3)
rot=rotmesh.onto(surf,lms,as.matrix(tar))
rotmesh=rot$mesh
nset=rotonmat(lms,lms,as.matrix(tar))
v1=nset[1,];v2=nset[2,];v3=nset[3,]
normal <- crossProduct(v2-v1,v3-v1)
zeroPro <- points2plane(rep(0,3),v1,normal)
sig <- sign(crossprod(-zeroPro,normal))
d <- sig*norm(zeroPro,"2")
inter=meshPlaneIntersect(rotmesh, v1, v2, v3)
open3d()
shade3d(rotmesh,col=3,alpha=0.4)
planes3d(normal[1],normal[2],normal[3],d=d,col=2,alpha=0.5)
X=inter[,1]
Y=inter[,2]
ash=ashape(X,Y,alpha=0)
ext=cbind(X[ash$alpha.extremes],Y[ash$alpha.extremes])
plot(ext,pch=19)
```

2.2.2 Acquisition of semilandmark on the outline

Once acquired an outline, the next step consists of definition of the set of semilandmark. At the time, different approach have been proposed and commonly used in literature, among the most used:

- ✓ points definition along the total number of x coordinates;
- ✓ points definition along the intersection of equally spaced radii with the outline;
- ✓ points definition as evenly-spaced along the outline.

The problem was introduced in literature by Bookstein, et al. (1982), in this subchapter are shown the examples of these different methodological approaches.

```
library("ctrlR")
data(pan.section)
section=section
section=cbind(1, section, 1)
section=rbind(1,section, 1)
section_junk<-imagematrix(section, type="grey")
section_junk[which(section_junk<0.95)]<-0
plot(section_junk)
cont<-Conte(round(unlist(locator(1)),0),section_junk)
scalecoord<-locator(2, type="p",pch=4,lwd=2)
scalepixsize<-sqrt(diff(scalecoord$x)^2+diff(scalecoord$y)^2)
X<-cont$X*30/scalepixsize
Y<-cont$Y*30/scalepixsize
Xc <- mean(X)
Yc <- mean(Y)
plot(NA,xlim=c(0,100),ylim=c(0,100),main="outline method 1",
  xlab="x coordinates",ylab="y coordinates")
matrix_c=cbind(X,Y)
n=30
X_sampled=round(seq(1, length(X), len = n + 1)[-(n +1)])
XY_sampled=matrix_c[X_sampled, ]
points(XY_sampled,pch=19,col="red")
```

In the example shown below (fig. 2.2.3) were obtained 30 semilandmarks evenly-spaced from the range of the x coordinates.

A second method to define the xy coordinates of semilandmark is that of "equally spaced angles" (Claude, 2008). The central angles formed by the intersection of a pair consecutive radii, departing from the centroid of an open or a closed outline, are equals. The point on the intersection between the outline and the radius will be a semilandmark (fig. 2.2.3). This approach was introduced by and commonly used, in Palaeoanthropology, for the study of dental morphology (e.g., Benazzi, et al., 2011, Benazzi, et al., 2012).

```
library("ctrlR")
data(pan.section)
section=section
section=cbind(1, section, 1)
section=rbind(1,section, 1)
section_junk<-imagematrix(section, type="grey")
section_junk[which(section_junk<0.95)]<-0
plot(section_junk)
cont<-Conte(round(unlist(locator(1)),0),section_junk)
scalecoord<-locator(2, type="p",pch=4,lwd=2)
scalepixsize<-sqrt(diff(scalecoord$x)^2+diff(scalecoord$y)^2)
X<-cont$X*30/scalepixsize
Y<-cont$Y*30/scalepixsize
Xc <- mean(X)
Yc <- mean(Y)
plot(NA,xlim=c(0,100),ylim=c(0,100),main="outline method 2",
  xlab="x coordinates",ylab="y coordinates")
matrix_c=cbind(X,Y)
n=30
XY_sampled_r=regularradius(X,Y,n)
points(XY_sampled_r$coord[,1]+Xc,XY_sampled_r$coord[,2]+Yc,pch=19,
col="red")
for (i in 1:n){
segments(0+Xc,0+Yc,XY_sampled_r$coord[,1]+Xc,XY_sampled_r$coord[,2
]+Yc)}
```

A third method applied on 2D or 3D outline is that of Bèzier curve approach. A Bèzier curve consists of a polynomial curve built from two points and a line vector. For the definition of a Bèzier curve is necessary to define a series of control points, ranging from P_0 to P_n (respectively, the first and last point) and that, once joined together, define a polygon that will contain the curve. The connection points for the realization of the so-called control polygon (or Bézier), occurs through the segments, starting from P_0 and coming to P_n. Recall that P_0 and P_n are the points that define the start and the end of the curve. The intermediate control points, on the other hand, normally do not lie in its path, but are used in the interpolation of the curve, to define the direction (Forrest, 1972). The degree of the Bèzier curves (n) is dependent on the number of control points which are the vertices of the polygon (v), according to a simple relationship $v = n - 1$. Bèzier curves can be defined from a set of Cartesian coordinates in 2 or 3 dimensions obtaining a parametric curve interpolation in a plane or in a three dimensional space. Furthermore, by defining appropriately the values of t you will be able to obtain the new coordinates of points evenly spaced.

Using the R codes reported in Claude (2008) and embedded in "bezier" R package (Olsen, 2015) can be acquired evenly-spaced semilandmark defining the intermediate points (fig. 2.2.3).

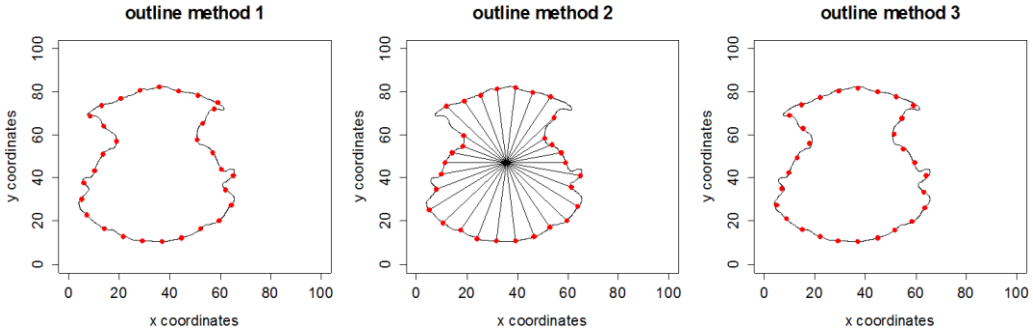

Figure 2.2.3: Semilandmark obtained after applying the first (on the left), second (on the middle) and third (on the right) method.

```
library("ctrlR")
data(pan.section)
section=cbind(1, section, 1)
section=rbind(1,section, 1)
section_junk<-imagematrix(section, type="grey")
section_junk[which(section_junk<0.95)]<-0
plot(section_junk)
cont<-Conte(round(unlist(locator(1)),0),section_junk)
scalecoord<-locator(2, type="p",pch=4,lwd=2)
scalepixsize<-sqrt(diff(scalecoord$x)^2+diff(scalecoord$y)^2)
X<-cont$X*30/scalepixsize
Y<-cont$Y*30/scalepixsize
Xc <- mean(X)
Yc <- mean(Y)
plot(NA,xlim=c(0,100),ylim=c(0,100),main="outline method 3",
  xlab="x coordinates",ylab="y coordinates")
A=cbind(X,Y)
bez.points=pointsOnBezier(A[unique(seq(1,dim(A)[1],length=999)),],30
)
points(bez.points,type="l")
```

To facilitate the use of 3D Bèzier curve from a landmark set or a curve acquired in Amira have been developed different functions and integrated in the ctrlR package. Using the module "SurfacePathSet" (connector on PlaneCut) in Amira 5.4.5 has been acquired a curve on a 3D model along the inferior temporal line (fig. 2.2.4).

The "curve" object is saved as AmiraMesh ASCII Lineset format; successively, this file is imported in R through the function `read.path.amira`.

The function `bezier.amira.set` contains an option to increase the number of intermediate points. It is reasonable to project the evenly-spaced landmark on surface through the function `projRead` (fig. 2.2.5) of the Morpho package (Schlager, 2013).

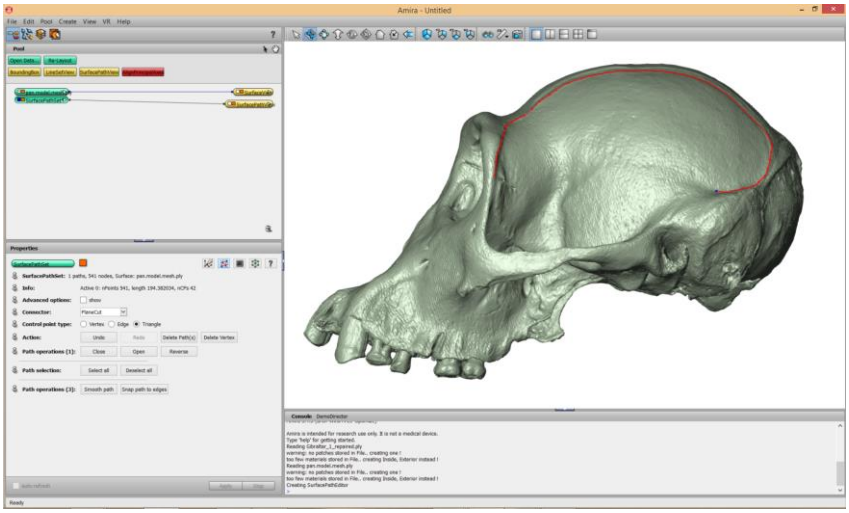

Figure 2.2.4: SurfacePathSet acquired in Amira (version 5.4.5).

```
library("ctrlR")
data(pan.model.mesh)
model.curve=bezier.amira.path("pan.model.curve.am",30,NULL)
proj_points=t(projRead(model.curve,pan.model.mesh)$vb)
open3d()
plot3D(model.curve,bbox=FALSE)
shade3d(pan.model.mesh,col=3,alpha=0.7)
```

The methods commonly used are:

- ✓ the Procrustes distance criterion: the semilandmarks are slided the along their tangent directions using the Procrustes distance (Rohlf, 2010);
- ✓ the TPS approach: the semilandmarks are slided based on minimizing bending energy (Bookstein, 1997a, Gunz, et al., 2005).

Figure 2.2.5: Definition of a set of evenly-spaced semilandmark after acquisition of a "path curve" in Amira (version 5.4.5).

2.3 Digital reconstructions

Virtual procedures, concerning digital reconstruction, are frequently applied to restore the human fossil specimens. Virtual imaging techniques allow acquiring a 3D digital version of a physical object. The approaches commonly used for the 3D modelling acquisition are:

- ✓ CT to different resolutions (e.g. CT-scan, Micro-Ct scan);
- ✓ Synchrotron radiation;
- ✓ Laser scanning;
- ✓ Photogrammetry.

An exhaustive literature is present on this matter on the application and functioning (e.g. Abel, et al., 2011, Friess, 2012, Mathys, et al., 2013, Slizewski, et al., 2010, Urbanová, et al., 2015, Weber, 2014).

A digital operation on virtual specimen is appropriate and/or necessary when the object is fragmented/damaged and/or deformed. In this subchapter of the thesis are reported the opportune methodological approaches. At the same time each reconstruction is not a correct copy of original shape, but some methods are reproducible others not.

2.3.1 Reconstruction by Bèzier surface

A fragmented specimen is a fossil composed by different fragmentary pieces, which may have points or margins of contacts. In the past, fragmented specimens were reassembled using bonding adhesive and/or plaster filler making it impossible or difficult to change the recomposition of the fragments (de León and Zollikofer, 2001, Ogihara, et al., 2006). Using 3D imaging techniques is possible to acquire the digital version of the specimen, to isolate the different materials using density filters or on the contrary proceeding with a manually segmentation (e.g., calvarium of Ceprano) (Di Vincenzo, et al., 2014). Once isolated virtually the various fragments, it is possible to proceed with a digital reconstruction. In this subchapter, are described the virtual reconstruction performed using computer techniques.

A recent reconstruction of the neanderthalian cranium of Amud 1 (Amano, et al., 2015) was performed through a method developed by Kikuchi and Ogihara (2013). The method based on parametric Bèzier surface extrapolates the surface of each fragment and mathematically predicts the shape of neighbouring fragments (fig. 2.3.1).

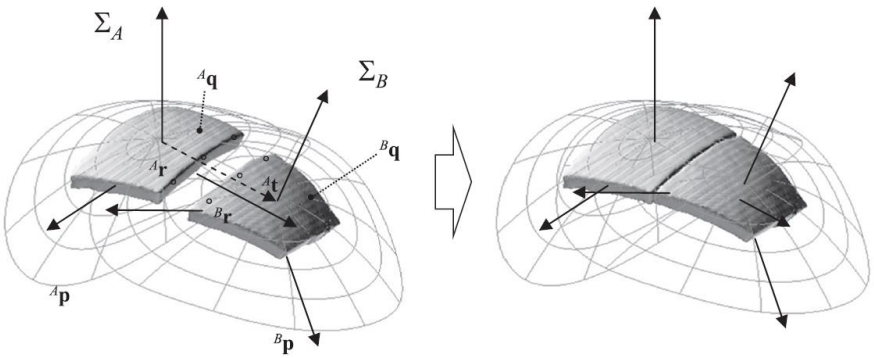

Figure 2.3.1: Representation and extrapolation of fragment surface. A bicubic Bèzier surface is fitted to the surface of a fragment. Adapted from "Computerized assembly of neurocranial fragments based on surface extrapolation" by Kikuchi and Ogihara (2013).

This procedure is complete automatized but so far used for regions of the skull that approximate an ellipse or a sphere such as the neurocranium; this method is undoubtedly modern, innovative and implementable. To date a manual intervention and human control is necessary in order to align regions particularly topological complex. An approach valid and commonly accepted and used in virtual reconstruction is that proposed by Zollikofer, et al. (2005) applied on the specimen TM 266-01-60-1 (*Sahelanthropus tchadensis*) through a partially computer-assisted reconstruction. In details, after a high-resolution computed tomography scan the cranium was dissembled along major cracks, cleaned (manual segmentation) and re-assembled manually. Some fragments were re-oriented along anatomical axes (for example the basioccipital along the midsagittal plane) while the deformed portions were retro-deformed using published methods.

2.3.2 Restore by retrodeformation

Vertebrates are, more or less, symmetric with respect to the sagittal plane, which divides the body into a right and left half (Mardia, et al., 2000). In addition to biological asymmetry, a fossil specimen often suffers by "flattening", "bending" and "shearing" that can be viewed as a series of locally affine deformations due to taphonomic processes (Lyman, 1994, Shipman, 1981). In the past, the reconstructions and the deformation corrections usually were performed manually by skilled expert anatomist or palaeontologists (Ogihara, et al., 2006, Ponce De León and Zollikofer, 1999). The upcoming of CT in the last two decades and 3D modelling techniques such as laser scanning and photogrammetry allows to apply different approaches to restore the bilateral symmetry of a digital model (Cunningham, et al., 2014, Weber, 2001). The standard techniques to restore virtually the missing parts is named "virtual restoration" (Gunz, et al., 2009); the protocols to correct the asymmetry between the right and the left side are called "symmetrization" (Bookstein and Mardia, 2003, Bookstein, 2005, Mardia, et al., 2000). A common approach, in order to restore the symmetry of a digital

model, uses the placement of two sets of landmarks, one on each side. The landmark sets are reflected/relabelled to compute a symmetric average of both original and mirrored sets. and subsequently the 3D model will be warped to the landmark sets thus obtained using TPS (Bookstein, 1989); this approach can be used to remove uniform shearing (Gunz, et al., 2009). Recently, a non-linear symmetrisation method, to restore bending and/or compression landmark-based, was proposed by Ghosh, et al. (2010) and evaluated by Tallman, et al. (2014).

All the methodological approaches depend on the amount of available landmarks that can be acquired on both sides; the landmark numerosity and the distribution affect the quality of the retrodeformation obtained. The quality of the retrodeformation depends heavily on the number (and its distribution on 3D model) of landmarks used (Gunz, et al., 2009).

2.3.3 Reconstruction by digital alignment

The digital alignment consists of the extrapolation of the rotation matrix to translate, rotate, and scale a fragment (or bone) using another object as reference.

In this subchapter are reported two different examples:

- ✓ Alignment by mirroring along the midsagittal plane;
- ✓ Alignment by landmark correspondence.

A restoration of the overall morphology by mirroring of the preserved side can be performed to restore the deficient side. This type of virtual reconstruction is very useful in that case when the GM analysis involves both sides. If the specimen is not deformed, this correction is desirable.

The protocol used to align a side along its mirrored version consists of different reproducibly steps:

- ✓ Definition of the midsagittal plane by 3 landmark;
- ✓ Cut of the mesh along the midsagittal plane;
- ✓ Maintaining the most preserved side;
- ✓ Mirroring of the maintained side;
- ✓ Moving each landmark on the closest vertex;
- ✓ Extracting numbering of the new vertices from the mesh matrix;
- ✓ Define a set on mirrored side using the same numbering of vertices;
- ✓ Rotation of the mirrored side on the preserved side using the rotation matrix calculating on the two landmark sets (on vertices);
- ✓ Merging of the both sides (fig. 2.3.2).

Figure 2.3.2: 3D model of *Pan troglodytes* mirrored along the midsagittal plane. The original side in green and its mirrored and aligned version in red.

This protocol is stored in the demo `digital.aligning.simm` in the R "ctrlR" package.

This procedure can be performed for graphical and didactic purposes, to align a specimen (often damaged) on a reference model.

```
library("ctrlR")
data(pan.model.mesh)
data(pan.model.msp)
sur=pan.model.mesh
sur_half=cutMeshPlane(sur, set[1,,1], v2 = set[2,,1], v3 =
set[3,,1],
normal = NULL,keep.upper = TRUE)
sur_mirr=mirror(sur_half, icpiter=10,subsample = 30)
points=aro.clo.points(t(sur_half$vb)[,-4], set[,,1])
rot_sur_mirr=rotmesh.onto(sur_mirr, t(sur_mirr$vb)[points,-4],
t(sur_half$vb)[points,-4])
shade3d(rot_sur_mirr$mesh,col=2)
shade3d (sur_half,col=3)
```

The figure 2.3.3 shows the digital alignment of the human remains labelled MK1 and MK2 (see subchapter 3.4). The MK1 is a left parietal fragment while MK2 is a frontal fragment (only almost complete the right side).

For each fragment is used the following protocol:

- ✓ Scaling of the reference specimen on Gombore fragment size;
- ✓ Mirroring of the fragment;
- ✓ Acquisition of a set of semilandmark on the fragment;
- ✓ Moving each semilandmark on most nearly vertex;
- ✓ Acquisition of the corresponding semilandmark set on mirrored fragment using the vertices numbering;
- ✓ Acquisition of the corresponding semilandmark set on reference specimen on both sides;
- ✓ Symmetrisation of bilateral semilandmark set on reference specimen;
- ✓ Rotation of the mirrored side on the preserved side using the rotation matrix between the two landmark sets (on vertices);
- ✓ Merging of both sides.

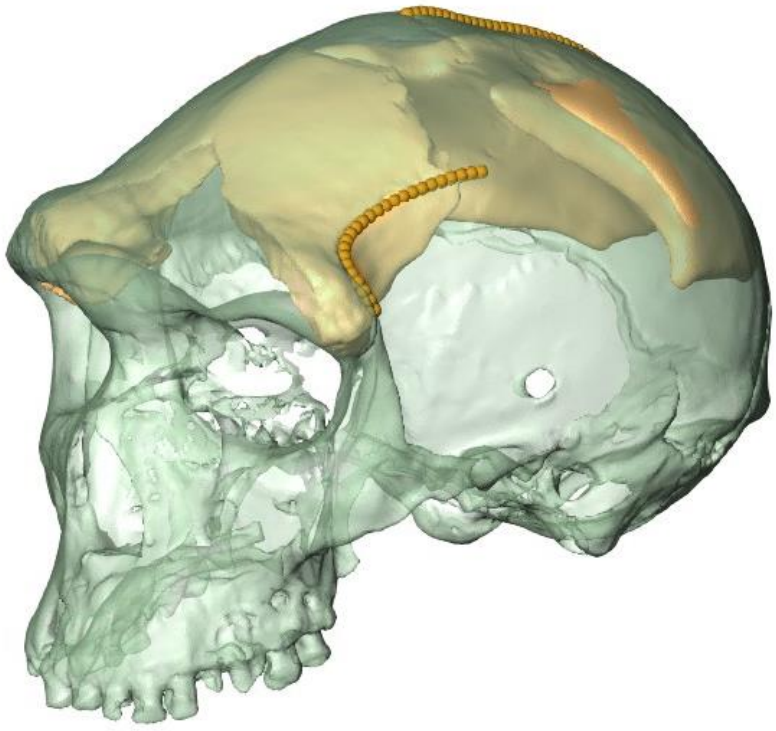

Figure 2.3.3: Digital alignment of the Melka Kunture cranial fragments on the 3D scaled model of Kabwe 1 (only the semilandmark configuration on Kabwe are shown).

2.3.4 Reconstruction by TPS and surface warping

Specimens often are damaged and some parts can be absent. In these case is desirable a Geometric Reconstruction via interpolant TPS paired to surface warping procedures (Gunz, et al., 2009). The protocol described by Gunz et colleagues (2009) uses a reference model complete and comparable to the target (damaged specimen) for morphology and phylogeny. A homologous landmark sets on both models (reference and target) are used to superimpose a semilandmark set (built on the reference) on the target specimen. The TPS is performed between the two surfaces using the (semi-) landmark sets as reference. The warped surface corresponding to the damage portions on the reference model can be cut out and merged to the target model.

Below an example is shown on the cranium of Saccopastore 1.

```
library("ctrlR")
data(exp.SCP1.mesh)
data(exp.SCP1.Lset)
data(chimera.mesh)
data(chimera.set)
data(chimera.SLset)
tar.set=chimera.set
ref.set= SCP1.Lset[c(1:15,24,19,26:35,44,39),]
temp.set=array(NA, dim = c(29, 3, 2))
temp.set[, , 1] = array(tar.set,dim=c(29,3,1))
temp.set[, , 2] = array(ref.set,dim=c(29,3,1))
tar.mesh=SCP1.mesh
ref.mesh=chimera.mesh
dir.create("temp.mesh")
mesh2ply(ref.mesh,paste("temp.mesh/","ref",sep=""))
mesh2ply(tar.mesh,paste("temp.mesh/","tar",sep=""))
P.set=chimera.SLset[,,1]
first_atl = createAtlas(ref.mesh, temp.set[,,1], P.set)
plotAtlas(first_atl)
open3d()
plot3D(temp.set[,,1],add=TRUE)
plot3D(P.set,add=TRUE,col=2)
shade3d(ref.mesh,col=3)
```

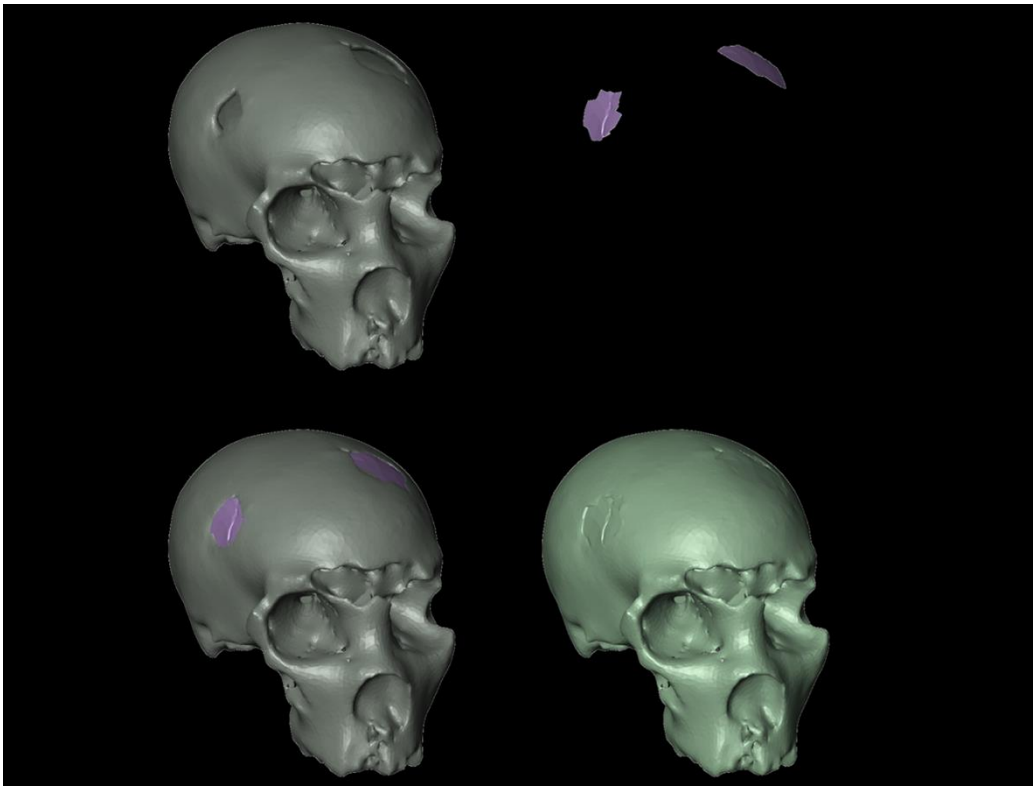

Figure 2.3.4: Reconstruction by TPS and surface warping performed on the 3D model of Saccopastore 1.

The warped surface of the `chimera.mesh` (stored in the ctrlR package), performed via TPS, was cut out to the corresponding damaged regions of Saccopastore 1. In Geomagic Studio (version 12) the surfaces were merged and filled. The virtual reconstruction is shown in the figure 2.3.4.

2.3.5 Semantics of the procedures related to the «Digital Morphological Recovery»

The recovery of digital morphological information includes all these procedures involving GM approaches on 3D models. Some protocols use the information only preserved on the deficient specimen other need a comparative sample. If the specimen is fragmented a manual intervention is necessary driven by expert anatomist; at the same time the use, in a second step, of the digital morphological recovery procedures can be useful to validate the fragments assembly.

In many studies, the terms "restoration" and "reconstruction" are often used as synonyms: the term "restoration" could be used in that case which the repaired regions of the specimen are obtained from the same deficient specimen; the term "reconstruction" could be used when the repaired region are obtained from a reference or a comparative sample. Small hole or localized damaged on regular and uniform region (e.g., cranial vault) often are repaired thanks the application of "filling" algorithm.

The digital restoration include retrodeformation (see 2.3.2), Bèzier surface (see 2.3.1) and mirroring procedures (see 2.3.3), while the digital reconstruction is referred to TPS method applied on a reference model (see 2.3.4) or using a comparative sample. The digital alignment is appropriate in that case, which we are interested to align a reference specimen on a target specimen (see `rotmesh.onto` function of the Morpho R package) (Schlager, 2013). Besides using of anatomical landmark is possible to align a damaged specimen through the definition of geometrical homologous points (semilandmark curves and semilandmark sets) on anatomical trait (e.g., neurocranium, cranial suture, temporal lines). The acquisition of two homologous (semi) landmark sets can be used to scale the reference model to the dimension of the target model, through the CS, the Euclidean distance calculated between two points or the length of a curve. Combining the procedures of mirroring and digital aligning is possible to mirror a side of a specimen defining just 3 point along the midsagittal plane to merge the original side and its mirrored version.

Table 2.3.1: Summary of the procedure used to recovery the morphological information.

Digital Morphological Recovery		
GM methodologies		
Digital Restoration	Retrodeformation	
	Bèzier surface	
	Mirroring	
Digital Reconstruction	Thin-plate spline	Reference model
		Comparative sample
Digital Alignment	By mirroring	
	By landmark correspondence	
No GM methodologies		
Auto fill		
Manual alignment		

2.4 Smoothing algorithms

In this subchapter are reported the fundamental mesh smoothing algorithm that are commonly applied to medical surface model and embedded in the main imaging 3D softwares (e.g. Mimics, Amira, Avizo, MeshLab). The Laplace filter is the simplest smoothing algorithm. This type of algorithm iteratively moves all surface vertices into the geometric centre of its topological neighbours (Bade, et al., 2006).

A neighbour of a reference vertex consists of all vertices connected with the first. We can distinguish topological neighbourhood (umbrella operator) of first and second order.

Figure 2.4.1: Neighbours of first (on the left) and second (on the right) type.

The laplacian smoothing algorithm products shrinkage and uses the follow smoothing operation:

$$p' = p + \frac{1}{n}\sum_{i=0}^{n-1}(q_i - p)$$

The new smoothed position p' of all vertices P results from its old position p and its neighbours q as shown in equation (1).

A different version of laplacian smoothing include in the algorithm a weighting factor λ (see equation 2).

$$p' = p + \frac{\lambda}{n}\sum_{i=0}^{n-1}(q_i - p)$$

The umbrella operator suffers of large inaccuracies for irregular meshes as the same supposedly constant parameterization is used. Fujiwara (FujiLaplace algorithm) presents the following formula (equations 3, 4):

$$L(x_i) = \frac{2}{E} \sum_{j \in N_i(i)} \frac{x_j - x_i}{|e_{ij}|}$$

with,

$$E = \sum_{j \in N_i(i)} |e_{ij}|$$

where $|e_{ij}|$ is the length of the edge e_{ij}, x_j are the neighbors of the vertex x_i. Therefore, when all edges are of size 1, this reduces to the umbrella operator (equation 5):

$$L(x_i) = \frac{i}{m} \sum_{j \in N_i(i)} x_j - x_i$$

where *m* is the number of the neighbors (Desbrun, et al., 1999).

Taubin algorithm fulfils a first a laplacian step with a positive scale factor λ (from 0 to 1) and then a second laplacian smoothing with a negative scale factor μ (from -1 to 0), greater in magnitude than λ (Taubin, 2002).

The angWeight smoothing algorithm executes an angle-based operation, making adjacent angles equal or in a certain ratio (Jin, et al., 2005, Zhou and Shimada, 2000).

3 Case-studies

3.1 Smoothing procedures in Geometric Morphometrics

3.1.1 Introduction

In recent years, the use of 3D biological models has become widespread in GM applications, thanks to sophisticated imaging techniques (e.g., CT-scan, micro CT, laser scanner, and photogrammetry) borrowed from fields other than biology. These technologies allow to virtually reproduce real specimens with settable values of image resolution, as well as to extract structures usually not available (brain endocasts, semicircular canals, etc) (Ni, et al., 2012, Weber, 2013) or difficult to study, if the integrity of the item has to be pursued (Friess, et al., 2002).

As a result, high levels of detail are permitted and morphology can be studied beyond the overall shape of a specimen. During the last years, morphological studies have increasingly focused on local and small scale variability, continually requiring higher resolutions, and this trend does not seem to be changing direction in the near future. landmark-based GM can be of limited use if the aim is to record small scale variability: for this purpose, semilandmark sliding has been developed, as it allows an extensive analysis of locally determined structures, by means of homologous geometrical landmarks superimposed through a set of anatomical points (Gunz, et al., 2005).

Although of countless usefulness, high levels of detail generate massive amounts of data, increasing the computational effort required for visualization and analysis: the higher the resolution of the item is, the more the percentage of computer memory that will be committed in manipulating the virtual specimen. Consequently, analysis carried out on high-resolution objects can be time-consuming. In these cases, the usual routine involves a digital simplification of the item, decimating the total number of facets through one of the algorithms commonly available in 3D visualization software packages. Another critical point relies on the discrete nature of both acquisition and geometrical simplification of specimens: real smooth surfaces are approximated by polyhedral ones, the scanned object appearing faceted (Friess, et al., 2002, Friess, 2012).

This problem is usually overcome through the application of a smoothing algorithm to the virtual object, whose outcome is an evenly curved surface (Taubin, 1995, Vollmer, et al., 1999).

These procedures provide lighter virtual reconstructions, more suitable for virtual handling, but the resulting models are inevitably a transformation of data, which, even if scarce, represent the structure of the real object. Although a number of works has focused on the efficiency of different procedures for both geometrical simplification

and smoothing algorithms (Bade, et al., 2006), their effect on GM analysis has not been taken in consideration so far. Choosing a smoothing algorithm is a crucial point in GM preliminary steps: if not correctly selected, it can entail a loss of information through shape and size distortion, introducing a bias on the entire analysis.

In order to evaluate the efficiency of different smoothing algorithms there are performed the following analysis/test:

- ✓ mesh distance performed between a 3D noised model and the same without disturbance after 3 smoothing iteration using the default setting based on the VCGLIB API (VCG for short), present in the Rvcg R package (Schlager, 2014);
- ✓ the previous analysis performed using different algorithm settings;
- ✓ effect of smoothing using algorithms scale-dependent on scaled models;
- ✓ definition of a method to define the optimal combination of smoothing algorithm type and parameters settings given 3D virtual specimen, and the facets desired reduction; its development in R environment, in order to achieve a simplified model as close as possible to the starting object (Profico, et al., 2014);
- ✓ evaluation of loss/retrieval of anatomical information in the 3D model after smoothing procedures in GM study semilandmark based using the R smoothing tool introduced above;
- ✓ general guidelines to smooth.

3.1.2 A preliminary smoothing algorithms test

A first comparison of smoothing algorithms efficiency was performed using a decimated surface model to 50000 faces of Saccopastore 1 specimen (decimated model). A first step consists in the definition of a noised model (noised model) from the decimated model moving each vertex to a casual distance extracted by a normal distribution centred in 0 with a standard deviation of 0.025. The noised model is subject to smoothing procedures using the algorithms embedded in the VCG library (Schlager, 2014) using the default settings reported in the Table 3.1.1 (results in fig. 3.1.1).

```
library("ctrlR")
data(exp.SCP1.mesh)
SCP1.noised=noise.mesh(SCP1.mesh)
shade3d(SCP1.noised,col=3)
mesh.dist=meshDist(SCP1.mesh,SCP1.noised)
mesh.threshold=sum(abs(mesh.dist$dists))
mesh.smoo.hcl=vcgSmooth(SCP1.noised,iter=3,type="hclaplace")
mesh.hcl.dist=meshDist(SCP1.mesh,mesh.smoo.hcl)
hcl.dist=sum(abs(mesh.hcl.dist$dists))
```

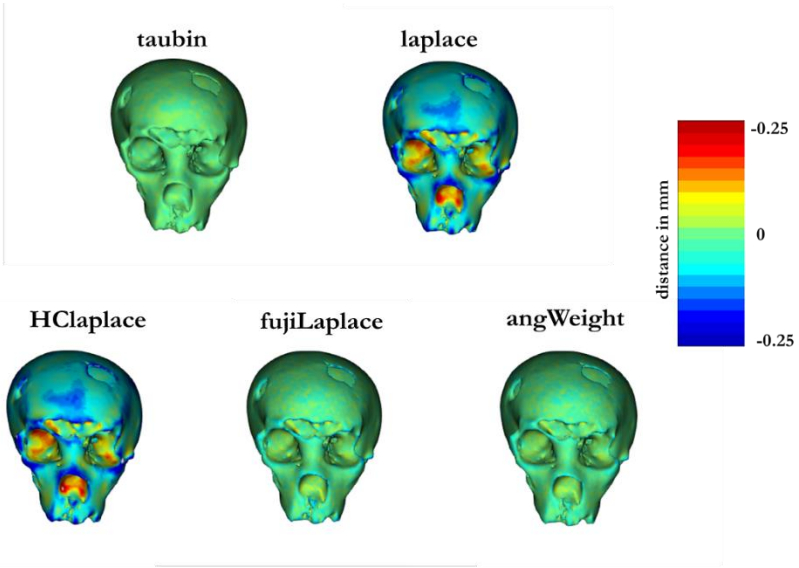

Figure 3.1.1. Locally mesh distance performed between the smoothed (iterations=3) and the noised 3D model of Saccopastore 1. The rainbow palette, reported in the legend, is ranged between -0.25 (blue) to 0.25 mm (red). The algorithm are set by default values reported in the vcgSmooth function (R package Rvcg).

Table 3.1.1: Smoothing settings performed on the 3D noised model of Saccopastore 1; mesh distance obtained between the Saccopastore 1 and noised smoothed version. In the last column are reported the percentage of entail/loss of anatomical information.

Algorithm type	Iter	Delta	Lambda	Mu	Mesh Distance	Entail(+)/Loss (-) anatomical information
laplace	3	-	-	-	2082.81	-322.94%
HClaplace	3	-	-	-	2170.24	-340.69%
angWeight	3	-	-	-	877.67	-78.21%
fujilaplace	3	0.10	-	-	1105.95	-124.57%
taubin	3	-	0.50	-0.53	304.60	38.14%

In the next step, the mesh distances have been calculated between the decimated and the noised models to define a threshold. When a noised model is smoothed with a specific algorithm and its relative settings, the mesh distance between the decimated and the smoothed models is calculated.

```
library("ctrlR")
data(exp.SCP1.mesh)
SCP1.noised=noise.mesh(SCP1.mesh)
Scp1_d=SCP1.mesh
scale_factor=c(0.25,0.50,1,2,4)
lambda=round(seq(0.01,0.30,length=10),2)
mu=-(lambda+0.001)
dist_smoothed_tau=NULL
thr=NULL
for (i in 1: length(scale_factor)){{
Scp1_d_s=scalemesh(Scp1_d,size=scale_factor[i])
Scp1_d_s_n=noise.mesh(Scp1_d_s, noise = (0.25/(1/scale_factor[i])),
seed = 123)
thr_eu=sum(abs(meshDist(Scp1_d_s,Scp1_d_s_n,plot=F)$dists))
thr=c(thr,thr_eu)
for (j in 1:length(lambda)){
smoothed=vcgSmooth(Scp1_d_s_n,type="tau",it=3,mu=mu[j],lambda=lambd
a[j])
dist_smoothed_tau=c(dist_smoothed_tau,sum(abs(meshDist(smoothed,Scp
1_d_s,plot=F)$dists)))}}}
result_tau=(1-(matrix(dist_smoothed_tau,ncol=10,byrow=T)/thr))*100
rownames(result_tau)=scale_factor
colnames(result_tau)=paste("lambda",lambda)
fix(result_tau)
```

In this way, an estimation of the associated recovery or loss of information is reported: this is shown as a percentage, where 100% represents the maximum recovery achievable (the smoothed model matches completely to the decimated model), while 0% indicates no recovery (the smoothed model matches the noised model). A negative percentage is associated to a loss of information, while positive values indicate a recovery. These values, mesh distance and loss/retrieval percentage, are calculated and reported in the table 3.1.1 for the default setting used.

The scale dependence properties of smoothing algorithms have been assessed using 5 different version of decimated model to 0.25, 0.50, 1, 2, and 4 size scales. In order to have the same added noise level, in geometric proportion, this is calibrate by multiplying the noise standard level (0.025) by the respective scale factor for each scaled model. After smoothing procedures (see table 3.1.2) for each pair of scaled/noised

model has been calculated the mesh threshold and this is used to evaluate the rate of loss or retrieval of anatomical information (see table 3.1.3).

Table 3.1.2: Smoothing settings performed on the 3D noised model of Saccopastore 1.

Algorithm type	Delta/Lambda	Algorithm type	Delta/Lambda	Mu
angWeight	0.010	fujiLaplace	0.171	
angWeight	0.042	fujiLaplace	0.203	
angWeight	0.074	fujiLaplace	0.236	
angWeight	0.107	fujiLaplace	0.268	
angWeight	0.139	fujiLaplace	0.300	
angWeight	0.171	taubin	0.010	-0.0101
angWeight	0.203	taubin	0.042	-0.0421
angWeight	0.236	taubin	0.074	-0.0741
angWeight	0.268	taubin	0.107	-0.1071
angWeight	0.300	taubin	0.139	-0.1391
fujiLaplace	0.010	taubin	0.171	-0.1711
fujiLaplace	0.042	taubin	0.203	-0.2031
fujiLaplace	0.074	taubin	0.236	-0.2361
fujiLaplace	0.107	taubin	0.268	-0.2681
fujiLaplace	0.139	taubin	0.300	-0.3001

Table 3.1.3: Percentages of entail/loss of anatomical information obtained after smoothing filter applied on the 3D noised model of Saccopastore 1.

taubin algorithm										
mesh size	**lambda 0.01**	**lambda 0.04**	**lambda 0.07**	**lambda 0.11**	**lambda 0.14**	**lambda 0.17**	**lambda 0.2**	**lambda 0.24**	**lambda 0.27**	**lambda 0.3**
0.25	-109,73	-108,37	-105,64	-101,61	-96,4	-90,14	-83,02	-75,24	-66,98	-58,48
0.5	-109,73	-108,37	-105,64	-101,61	-96,4	-90,14	-83,02	-75,24	-66,98	-58,48
1	-109,73	-108,37	-105,64	-101,61	-96,4	-90,14	-83,02	-75,24	-66,98	-58,48
2	-109,73	-108,37	-105,64	-101,61	-96,4	-90,14	-83,02	-75,24	-66,98	-58,48
4	-109,73	-108,37	-105,64	-101,61	-96,4	-90,14	-83,02	-75,24	-66,98	-58,48
fujiLaplace algorithm										
mesh size	**delta 0.01**	**delta 0.04**	**delta 0.07**	**delta 0.11**	**delta 0.14**	**delta 0.17**	**delta 0.2**	**delta 0.24**	**delta 0.27**	**delta 0.3**
0.25	-12,61	-63,64	-170,68	-251,25	-318,34	-398,29	-484,99	-575,54	-669,14	-764,63
0.5	-68,17	-11,33	-9,2	-20,93	-41,47	-65,6	-94,16	-122,83	-149,18	-172,24
1	-94,59	-66,36	-43,51	-27,52	-16,68	-11,09	-8,39	-8,26	-8,29	-9,31
2	-101,59	-94,07	-86,68	-79,49	-72,56	-65,91	-59,53	-53,6	-48,16	-43,17
4	-103,35	-101,46	-99,58	-97,69	-95,82	-93,95	-92,09	-90,24	-88,39	-86,56
angWeight algorithm										
mesh size	**delta 0.01**	**delta 0.04**	**delta 0.07**	**delta 0.11**	**delta 0.14**	**delta 0.17**	**delta 0.2**	**delta 0.24**	**delta 0.27**	**delta 0.3**
0.25	-70,16	0,62	19,06	11,88	-4,84	-28,18	-59,17	-95,49	-136,61	-180,79
0.5	-86,46	-38,65	-6,28	11,36	18,46	18,19	13,76	7,07	-1,71	-12,27
1	-95,07	-68,43	-45,12	-25,71	-10,3	1,31	9,43	14,72	17,88	19,08
2	-99,47	-85,52	-72,35	-59,99	-48,5	-37,95	-28,46	-19,97	-12,43	-5,86
4	-101,7	-94,58	-87,64	-80,89	-74,34	-68	-61,86	-55,92	-50,22	-44,75

Only the AngWeight and Fujilaplace algorithms are scale dependent. This aspect suggests being careful when we use these algorithm; a critical choice is the set of scale factor delta. Therefore in all those cases in which the mesh is small in size (e.g., teeth, small skull, inner ear) is highly recommended to use very small values for delta.

In order to analyse the efficiency for each algorithm, the Saccopastore 1 noised model (decimated to 50000 face) has been subjected to a iteratively smoothing procedure (ten iterations) using the following algorithms "laplace", "HClaplace", "fujiLaplace", "angWeight" and "taubin", available in "Rvcg" R package (Schlager, 2014) using the setting reported in the table 3.1.4.

Table 3.1.4: Smoothing algorithm settings.

Algorithm type	Delta/Lambda	Algorithm type	Delta/Lambda	Mu
Laplace	-	fujiLaplace	0.14	
HClaplace	-	fujiLaplace	0.17	
AngWeight	0.01	fujiLaplace	0.20	
AngWeight	0.04	fujiLaplace	0.24	
AngWeight	0.07	fujiLaplace	0.27	
AngWeight	0.11	fujiLaplace	0.30	
AngWeight	0.14	Taubin	0.01	-0.02
AngWeight	0.17	Taubin	0.04	-0.05
AngWeight	0.20	Taubin	0.07	-0.08
AngWeight	0.24	Taubin	0.11	-0.12
AngWeight	0.27	Taubin	0.14	-0.15
AngWeight	0.30	Taubin	0.17	-0.18
fujiLaplace	0.01	Taubin	0.20	-0.21
fujiLaplace	0.04	Taubin	0.24	-0.25
fujiLaplace	0.07	Taubin	0.27	-0.28
fujiLaplace	0.11	Taubin	0.30	-0.31

In the figures 3.1.2-6 are reported the fingerprint for each algorithm setting (see table 3.1.5) for the first 10 iterations.

```
library("ctrlR")
data(exp.SCP1.mesh)
tau=fingerprint_smooth(ref.mesh=SCP1.mesh,noise=0.25,alg="taubin",
  lambda=round(seq(0.01,0.3,length=10),2),
  delta=NULL,iter=10,range=10)
fuj=fingerprint_smooth(ref.mesh=SCP1.mesh,noise=0.25,alg="fujilaplace"
,
  lambda=NULL,
  delta=round(seq(0.01,0.3,length=10),2),iter=10,range=10)
ang=fingerprint_smooth(ref.mesh=SCP1.mesh,noise=0.25,alg="angweight",
  lambda=NULL,
  delta=round(seq(0.01,0.3,length=10),2),iter=10,range=10)
lap=fingerprint_smooth(ref.mesh=SCP1.mesh,noise=0.25,alg="laplace",
  lambda=NULL,
  delta=NULL,iter=10,range=10)
hcl=fingerprint_smooth(ref.mesh=SCP1.mesh,noise=0.25,alg="hclaplace",
  lambda=NULL,
  delta=NULL,iter=10,range=10)
plot(tau);plot(fuj);plot(ang);plot(lap);plot(hcl)
```

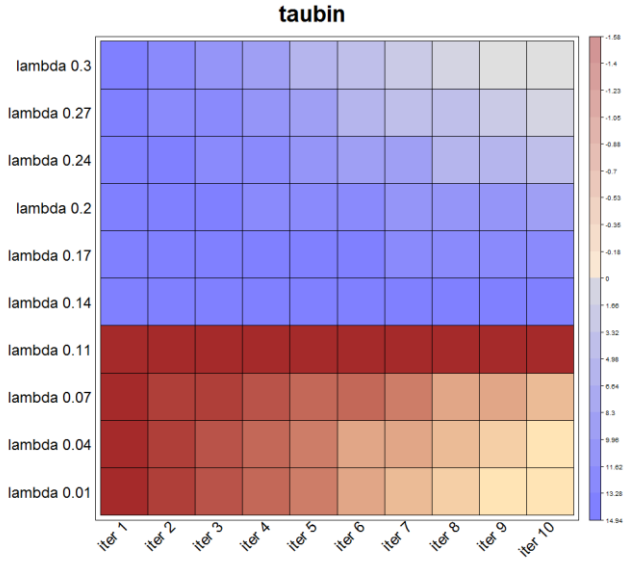

Figure 3.1.2: Fingerprint of retrieval/loss of anatomical information for Taubin algorithm (iteration=10) calculated through mesh distance between decimated and smoothed noised models. Colour red indicates loss, the blue recovery.

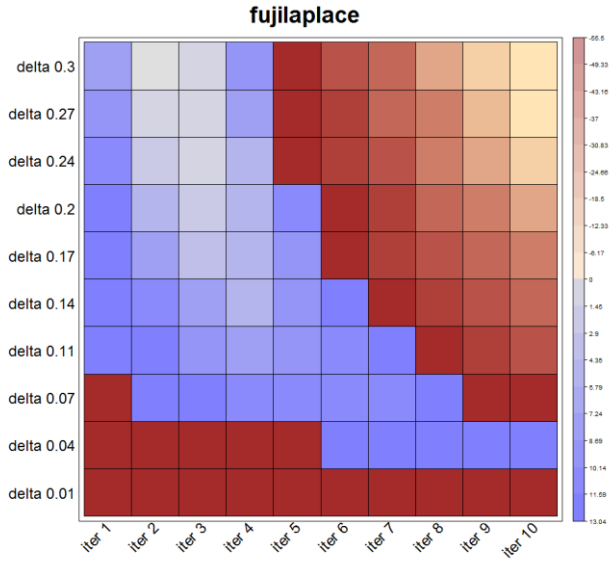

Figure 3.1.3: Fingerprint of retrieval/loss of anatomical information for fujiLaplace algorithm (iteration=10) calculated through mesh distance between decimated and smoothed noised models. Colour red indicates loss, the blue recovery.

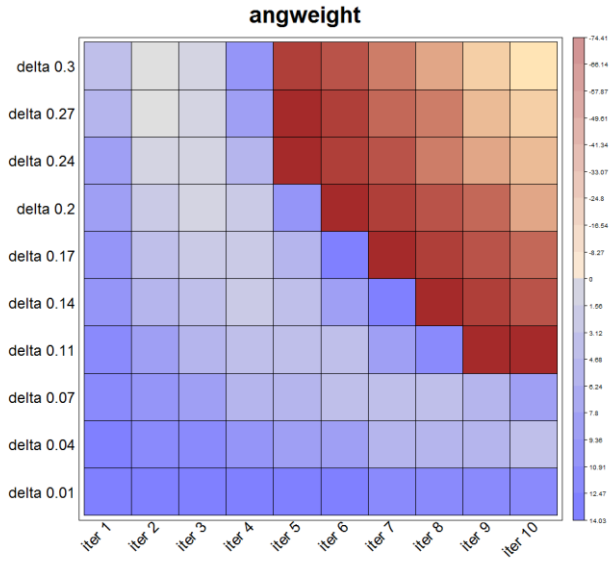

Figure 3.1.4: Fingerprint of retrieval/loss of anatomical information for angWeight algorithm (iteration=10) calculated through mesh distance between decimated and smoothed noised models. Colour red indicates loss, the blue recovery.

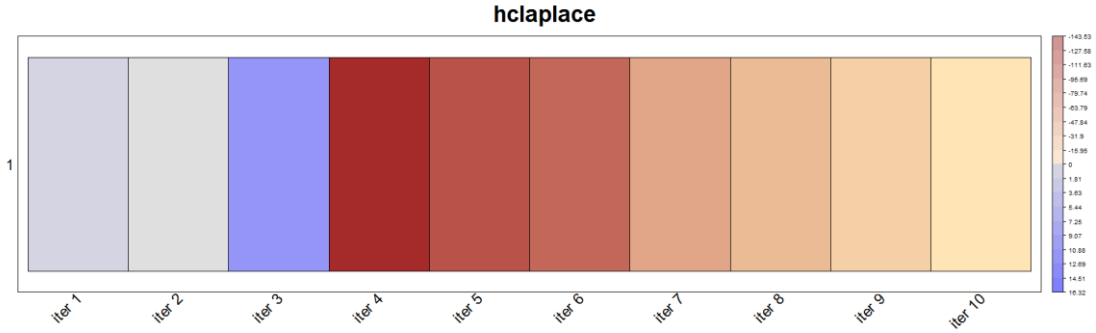

Figure 3.1.5: Fingerprint of retrieval/loss of anatomical information for HClaplace algorithm (iteration=10) calculated through mesh distance between decimated and smoothed noised models. Colour red indicates loss, the blue recovery.

.

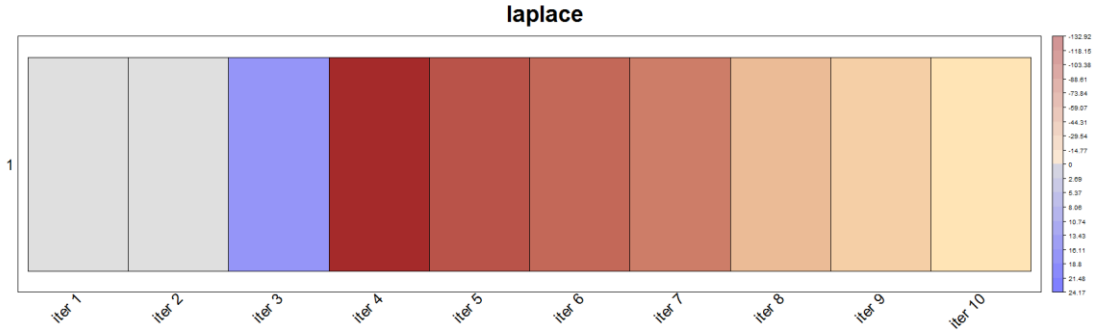

Figure 3.1.6: Fingerprint of retrieval/loss of anatomical information for laplace algorithm (iteration=10) calculated through mesh distance between decimated and smoothed noised models. Colour red indicates loss, the blue recovery.

3.1.3 Topological noise removal through decimation and smoothing procedures

The techniques of 3D acquisition involve the generation of topological noise due to beam hardening (CT-scan), light refraction (photogrammetry) and shadow areas (laser scanner and photogrammetry) (Brooks and Di Chiro, 1976, Friess, 2012, Guskov and Wood, 2001, Slizewski, et al., 2010).

These modifications, also referred to as topological artefacts or errors, are common when dealing with 3D models and can deform the reconstructed specimen locally, eventually concealing features of interest. As shown by Wood and colleagues (2002), the topological simplification, by decimating vertices and facets of a mesh, can solve these problems facilitating the subsequent steps in surface processing. One critical point of this decimation relies on the discrete nature of geometrical simplification: real smooth surfaces are approximated by polyhedral ones, and the decimated object appears therefore faceted (Friess, 2012). Smoothing algorithms are usually applied to counteract the problems linked to acquisition, rendering and decimation (Bade, et al., 2006, Guskov and Wood, 2001, Taubin, 1995, Vollmer, et al., 1999, Wood, et al., 2002, Zhou and Shimada, 2000). These algorithms act by relocating the vertices constituting the virtual specimen in order to achieve an evenly curved surface (Vollmer, et al., 1999, Weyrich, et al., 2004).

The results of the subchapter 3.2.1 highlight as the application of an appropriate smoothing filter involves a recovery of anatomical information reducing the topological noise.

The evaluation of the recovery of the anatomical information through decimation has been assessed on a noised version of a 3D model. 100 values of decimation were calculated in order to obtained the mesh distance from the higher to the lower-resolution decimated noised models. These values were been compared with the mesh distance calculated on the higher and noised model to assessed the reduction or increasing of topological disturbance (Table 3.1.5).

```
library("ctrlR")
data(exp.venus.mesh)
sur=venus.mesh
noi=noise.mesh(sur,0.075)
thr.h_n=sum(abs(meshDist(sur,noi,plot = F,method = "m")$dists))
dec.factor=seq(500,50000,length=100)
thr.d_n=NULL
for(i in 1:length(dec.factor)){
dec=vcgQEdecim(noi, factor [i])
thr.d_n[i]=sum(abs(meshDist(sur,dec,plot = F,method = "m")$dists))}
plot(1:length(thr.d_n), thr.d_n,pch=19)
thr.d_n [which(thr.d_n < thr.h_n)]
round((1-( thr.d_n / thr.h_n))*100,2)
```

Table 3.1.5: Cumulative absolute mesh distance expressed as percentage (d (%)) between the high resolution and decimated models (S) at different number of traiangles (D).

S	D	d (%)	S	D	d (%)	S	D	d (%)	S	D	d (%)
1	500	-728,69	26	13000	-13,16	51	25500	0,39	76	38000	1,06
2	1000	-397,21	27	13500	-11,69	52	26000	0,47	77	38500	1,03
3	1500	-280,16	28	14000	-10,08	53	26500	0,58	78	39000	0,97
4	2000	-210,99	29	14500	-8,99	54	27000	0,48	79	39500	0,92
5	2500	-165,06	30	15000	-8,22	55	27500	0,69	80	40000	0,93
6	3000	-133,74	31	15500	-7,18	56	28000	0,82	81	40500	0,98
7	3500	-113,82	32	16000	-6,6	57	28500	0,87	82	41000	0,97
8	4000	-97,59	33	16500	-5,61	58	29000	0,92	83	41500	0,99
9	4500	-84,76	34	17000	-4,89	59	29500	0,91	84	42000	0,86
10	5000	-74,93	35	17500	-4,59	60	30000	0,89	85	42500	0,72
11	5500	-65,04	36	18000	-4,37	61	30500	1,13	86	43000	0,64
12	6000	-56,99	37	18500	-3,78	62	31000	1,35	87	43500	0,69
13	6500	-49,97	38	19000	-3,5	63	31500	1,33	88	44000	0,68
14	7000	-43,95	39	19500	-3,17	64	32000	1,32	89	44500	0,68
15	7500	-39,12	40	20000	-2,67	65	32500	1,25	90	45000	0,61
16	8000	-36,14	41	20500	-2,24	66	33000	1,34	91	45500	0,58
17	8500	-31,93	42	21000	-1,91	67	33500	1,25	92	46000	0,5
18	9000	-28,39	43	21500	-1,62	68	34000	1,21	93	46500	0,43
19	9500	-26	44	22000	-1,46	69	34500	1,23	94	47000	0,34
20	10000	-23,09	45	22500	-1,18	70	35000	1,29	95	47500	0,29
21	10500	-20,48	46	23000	-0,71	71	35500	1,22	96	48000	0,26
22	11000	-18,92	47	23500	-0,61	72	36000	1,22	97	48500	0,25
23	11500	-17,27	48	24000	-0,38	73	36500	1,11	98	49000	0,25
24	12000	-15,84	49	24500	-0,14	74	37000	1,07	99	49500	0,23
25	12500	-14,35	50	25000	0,23	75	37500	1,06	100	50000	0,12

In order to evaluate the effect of decimation alone and paired to a smoothing filter has been applied the following protocol:

- ✓ Adding noise to an high resolution model;
- ✓ Calculation of the mesh distance between the high resolution and noised model;
- ✓ Decimation of the mesh to 31000 triangles (from 74495);
- ✓ Calculation of the mesh distance between the high resolution and decimated model;
- ✓ Identification of the optimal smoothing parameters through the `mesh.smooth.tool` function on the decimated model;
- ✓ Calculation of the mesh distance between the high resolution and smoothed decimated model.

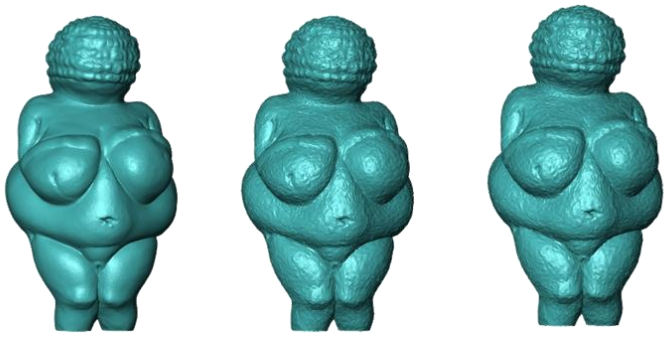

Figure 3.1.7: Model of the Venus of Willendorf on the left, its noised version on the middle and its decimated noised (to 50000 triangle) on the right.

Table 3.1.6: Values of the cumulative absolute mesh distance expressed as mm and percentage after smoothing filter applying.

Model	Triangles	Mesh distance (mm)	%	Smoothing filter
Full resolution	74495	0	0	
Noised	74495	1869.58	100	
Smoothed high resolution	74495	1253.74	32.94	Alg='Tau Lambda=0.38 Iter=8
Noised Decimated	31000	1844.75	1.33	
Smoothed decimated	31000	1649.68	11.76	Alg='Tau Lambda=0.19 Iter=10

The model tested is a digital version of the Willendorf venus (fig. 3.1.7) scanned using the NextEnging 3D laser scanner. The model consists of 74495 triangles. A background noise has been added moving each vertex by a casual distance extracted by a normal distribution centred in 0 with standard deviation equals to 0.075. The mesh distance between the starting and noised models is equals to 1869.58 mm; after decimation to 31000 triangles

this distance is lowered to 1844.75 mm. The estimation of optimal smoothing parameters (Table 3.1.6) occurs in two steps:

- The range of the parameters of taubin, angweight and fujilaplace algorithms on which a recovery of anatomical information is obtained through the calculation of the mesh distance between the original model and the smoothed decimated model after 1 smoothing iteration. Using a iterative procedure the smoothing parameter is multiplied by a scale factor until it reaches a value of mesh distance lower than 1869.58 (indicating a recovery of anatomical information);
- The range between 0 and the value of the parameter which a recovery of anatomical information occurred is used to define 10 values for the smoothing parameter;
- The `mesh.smooth.tool` function tests the smoothing filters using the smoothing values found in the previous steps in an iterative procedure (iteration = 20).

We demonstrate as the topology simplification (alone or paired to smoothing procedures) on several complex models, and show its benefit for subsequent surface processing.

```
library("ctrlR")
data(exp.venus.mesh)
run.tool=mesh.smooth.tool(sur=venus.mesh,tarface=NULL,noise=0.075)
run.tool.dec= mesh.smooth.tool(sur=venus.mesh,tarface=NULL,
noise=0.075,lambda=run.tool$tau.par,delta_AW=run.tool$ang.par)
min(run.tool$matrix)
min(run.tool.dec$matrix)
round((1-(run.tool$thr_n / min(run.tool$matrix)))*100,2)
round((1-(run.tool$thr_n / run.tool.dec$thr_n))*100,2)
round((1-(run.tool$thr_n / min(run.tool.dec$matrix)))*100,2)
```

3.1.4 Assessment of the effect of smoothing in Geometric Morphometric applications

To evaluate the effect of smoothing procedures in GM study a sample of 10 specimens of *Pan troglodytes* have been sampled acquiring on each individual a set of 6 landmark (Table 3.1.7). A semilandmark set (42 points) built on the reference specimen (USNM174700) and it was superimposed on the comparative sample, through a Procrustes step with sliding to minimise the bending energy (fig. 3.1.8) (Gunz, et al., 2005).

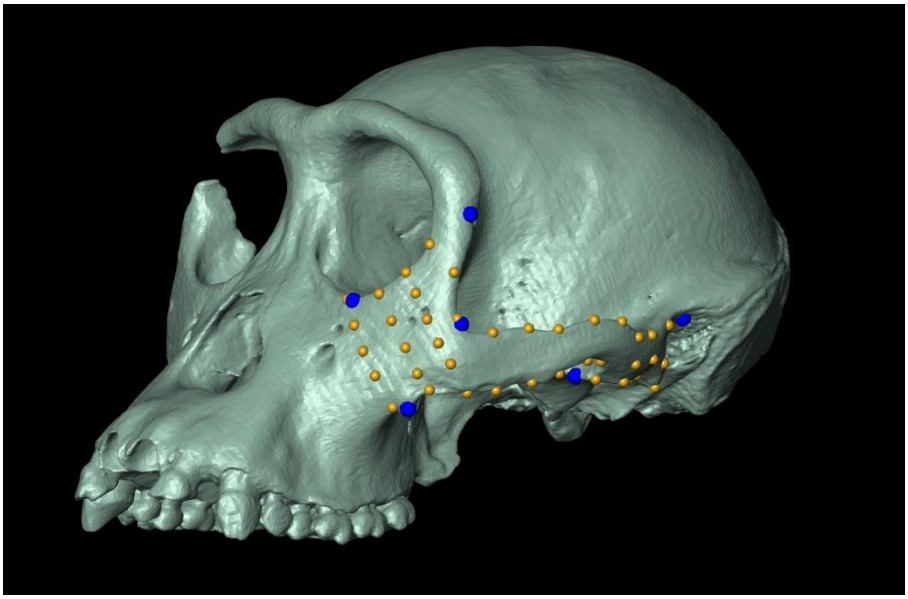

Figure 3.1.8: Landmark (in blue) and semilandmark (in yellow) are shown.

Table 3.1.7: Landmark descriptions.

Landmark	Definition
1	The point located at the upper margin of ear canal
2	The point where the zygomatic-frontal suture meets the external margin of the orbit
3	The point where the zygomatic-maxillare suture meets the external margin of the orbit
4	The most inferior point of the maxillary process
5	The innermost point located in the infratemporalis fossa
6	The point of major curvature placed on the superior margin of the zygomatic arch

Successively, the smoothing filters (11 settings) reported in the table 3.1.6 were applied on each specimen. After the procedure of sliding were obtained 120 specimens (10 original + 110 smoothed versions).

Table 3.1.8: Series of smoothing filters applied on each specimen.

Algorithm type	Delta/Lambda	Mu	Iter
Laplace	-	-	5
HClaplace	-	-	5
taubin	0.10	-0.011	5
taubin	0.30	-0.301	5
taubin	0.50	-0.501	5
angWeight	0.10	-	5
angWeight	0.30	-	5
angWeight	0.50	-	5
fujiLaplace	0.10	-	5
fujiLaplace	0.30	-	5
fujiLaplace	0.50	-	5

The landmarks on the smoothed surfaces occupy the same vertices as on the original model, the number of each vertex being known. In this way, all the possible sources of error are prevented: the new landmark set (the one on the smoothed mesh) is shifted relative to the landmarks on the original model only because of smoothing. Once all the smoothed surfaces have their own landmark sets, these can be used in the semilandmarks sliding procedure.

The semilandmark sets thus obtained were subjected to GPA and PCA.

In order to evaluate the effect of smoothing, during the sliding procedure, the values of the PC scores corresponding to the original specimen were compared with those of smoothed version. The table 3.1.7 shows, for each series of specimen, how many times the values of PC scores observed in the smoothed versions are more close to another specimen rather than no-smoothed corresponding specimen. In addition, a simultaneous mismatch for paired PCs is reported in the Table 3.1.9 a plot of the first two PCs is reported in the figure 3.1.9 for graphical purpose.

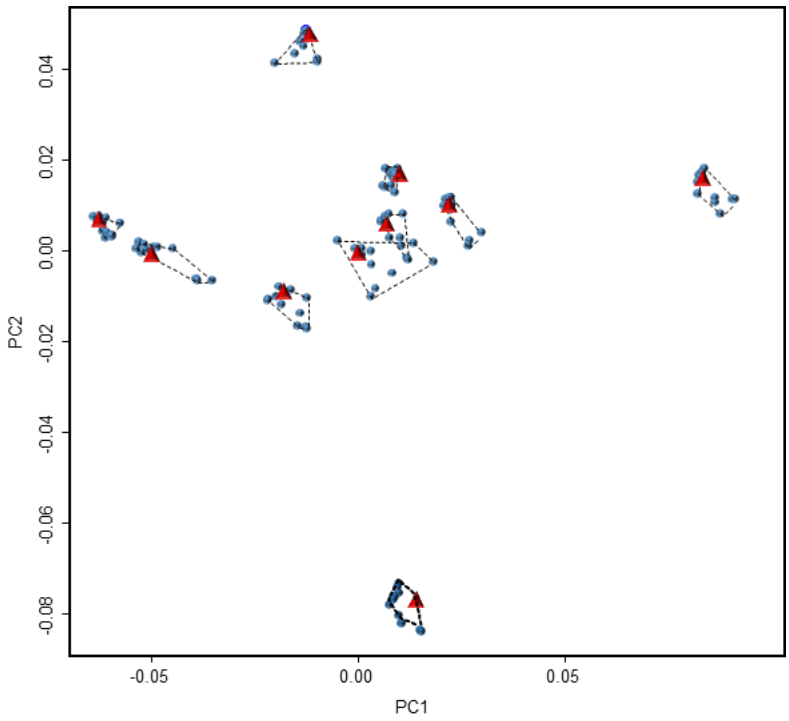

Figure 3.1.9: Principal component analysis performed on the semilandmark set slid on original and smoothed specimens.

Table 3.1.9: Error (%) expressed as ratio of mismatch count of the series of smoothed models on the original series (not smoothed).

PC	% error	Mismatch count
PC 1	29.09	32/110
PC 2	50.00	55/110
PC 3	48.18	53/110
PC 4	35.45	39/110
PC 5	30.00	33/110
PC1/PC2	13.64	15/110
PC1/PC3	18.18	20/110
PC1/PC4	15.46	17/110
PC1/PC5	10.91	12/110
PC2/PC3	24.55	27/110

3.1.5 Definition and development of the smoothing tool

The results for the smoothing algorithms efficiency using the mesh distance between the noised and decimated models show as some algorithms and settings, than other, recover more anatomical information than others; in particular using some settings for "taubin", "angWeight", and "FujiLaplace" algorithms. The mesh distance records the Euclidean distance between the compared surfaces.

In GM studies semi landmark-based, normally, the attention is placed on a single anatomical district. For this reason, it is interesting to analyse the interaction between different anatomical districts and smoothing procedures. The reference model can be decimated to a definite facets number in order to facilitate the sliding procedures (GPU effort). On the decimated surface were applied different smoothing algorithm settings in order to if it is possible to retrieve part of anatomical information loss during decimation process.

For the scale dependent smoothing algorithm (angWeight and FujiLaplace), in our method, there is a preliminary estimation of the scale dependent parameter through the evaluation of anatomical retrieval smoothing the decimated model using a progressive scale for dependent parameter. The estimation will stop if the parameter of scale dependent algorithm allows to recovery anatomical information calculated of the mesh distance between the reference and the smoothed models. A threshold value is calculated performing a mesh distance among the reference and the decimated models, above which the smoothing algorithm with a specific setting entails a recovery of anatomical information loss during the decimation process.

This methodological approach is addressed to GM study semilandmark based, and therefore are necessary a landmark (L-set) and semilandmark set (SL-set). At this point, the landmark set, built on the imported reference surface, is passed on the simplified model, in order to use it for sliding the semilandmarks on it: this is achieved by moving each point from its position on the reference to the closest vertex on the model. The so obtained set is moved back onto the reference surface by projection and these coordinates will be used as the new reference landmark set hence on. This projection makes the landmarks on the two surfaces to be geometrically homologous; also, it permits to estimate the error due to the movement of the points from the reference to the simplified model (fig. 3.10): when the initial and the final position of the landmarks on the reference are compared, they account for a very slight displacement, in the order of microns.

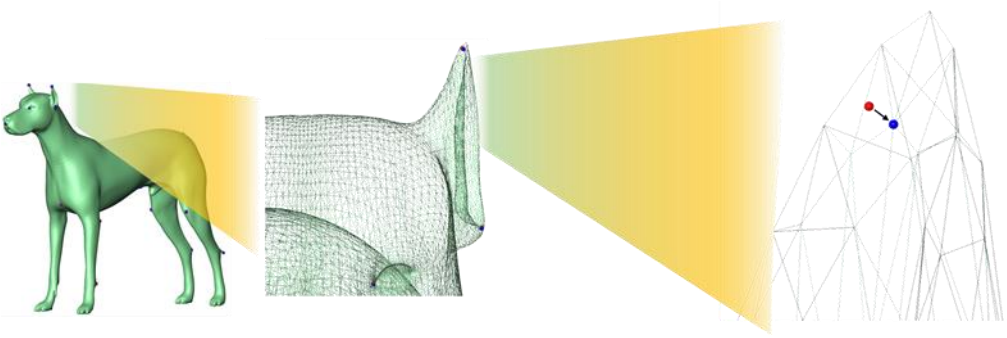

Figure 3.1.10: Scheme of the landmarks moving on the nearest vertex: in this 3D model the mean landmark shifting is equal to 5.7124 μm and the total is ranged between 0.4013 μm and 13.1534 μm.

This procedure allows preserving geometrical information for both the models and the reference sets, while keeping the loss of anatomical information at a minimum. In facts, the "error" due to landmark shifting is reasonable smaller than accuracy in landmark re-sampling. Smoothed surfaces has not undergone the same process, because here the landmarks effectively occupy the same vertex as in the models surfaces, the number of each vertex being known: in this way, all the possible sources of error due to sampling or projection are prevented.

The next step consists in the superimposition/sliding procedure of the SL-set on the decimated model. The Euclidean distance between the two sets returns a value directly proportional to the rate of anatomical information loss/recovered.

The procedure described has been adapted to build a tool (`aro.smooth.tool`) producing an optimized model to be exploited in semilandmark based GM applications, when specimens simplification and smoothing are desirable to perform analysis (Profico, et al., 2014).

With the end of the sliding step the iterative process stops and the data obtained are used for the estimation of the optimal smoothing settings. The shape alteration due to smoothing is calculated as the Euclidean distance between the "reference" and the "smoothed" semilandmarks. In order to discriminate the algorithms and iterations resulting in a loss and a recovery of information, these distances are compared to the threshold value described above: this value is calculated as the Euclidean distance between the simplified model and the reference surface. The threshold defines an upper limit of information loss: the semilandmark sets lying under this threshold represent smoothing settings generating surfaces closer to the reference than the simplified model is. The algorithm and its iteration which result in the smallest distance from the reference surface, will be considered the optimal smoothing settings in the

given conditions. If no iteration is lying under the threshold value, the optimal settings are considered the ones resulting in the smallest loss of information. In addition, an estimation of the surface size alteration due to smoothing is performed. Size is calculated in terms of CS of the semilandmark sets: a threshold is used as in the shape estimation.

Once the tool finishes the estimation, a series of outputs are made available to the user. First of all, the optimal smoothing settings are printed in the R workspace, indicating the algorithm, the iteration and the scale factors values used. Also, an estimation of the associated recovery or loss of information is printed: this is shown as a percentage where 100% represents the maximum recovery achievable (the smoothed surface matches completely the reference), while 0% indicates no recovery (the smoothed surface matches the simplified model). A negative percentage is assigned to loss of information while a positive value indicates the recovery. The estimation of CS modification for the optimal smoothing settings is printed as well: it is calculated through the same approach used for the shape estimation. A matrix containing the results of the overall analysis is provided: the percentages of loss/recovery of information are displayed for all the algorithms and the iterations; the ranges of the scale factors adopted in the analysis are shown in the results matrix. The optimal smoothing settings are not only printed in the workspace: they are also used to generate the surface resulted from the best smoothing performance in the analysis. This smoothed surface is automatically saved in the folder set as the working directory. The landmarks and semilandmark sets belonging to the optimally smoothed surface are provided as well.

This tool is conceived to supply the user with a simplified specimen starting from a surface in Polygon file format (PLY); number or percent of facets for simplification process will be set up by the user, who will also provide landmark and semilandmark sets to be later used for his/her own next analysis. For what concerns smoothing algorithms and related parameters, the tool is provided with the default settings used for the above described analysis: users are however allowed to change them and perform a more specific control on what could be the best values needed for their own purposes.

3.1.6 Application of the smoothing tool

In this section are reported the full version of two example integrated in the R package Arothron (Profico and Veneziano, 2015). In particular, the `aro.smooth.tool` it can be started completely automatized set only the number of triangles desidered (decimation of reference model), the number of iteration and providing a landmark and a semilandmark sets. All parameter for “taubin”, “angWeight” and “fujiLaplace” algorithms will be estimated automatically.

Alternatively, `aro.smooth.tool` can be set fully by the user defining the algorithms parameter.We provide a short example to explain the step-by-step procedure of application of the tool.

The surfaces considered are a model of the Neanderthal skull of Saccopastore 1 (50000 triangles, 26359 points). The landmarks and semilandmark sets were collected in Amira (version 5.4.5) and then used to generate the semilandmark sets.

```
library("ctrlR")
data(exp.SCP1.mesh)
data(exp.SCP1.SLset)
data(exp.SCP1.Lset)
example=aro.smooth.tool(model=SCP1.mesh,SL.set=SCP1.SLset,L.set=SCP
1.Lset,iter=10,tarface=10000,lambda.iter =
```

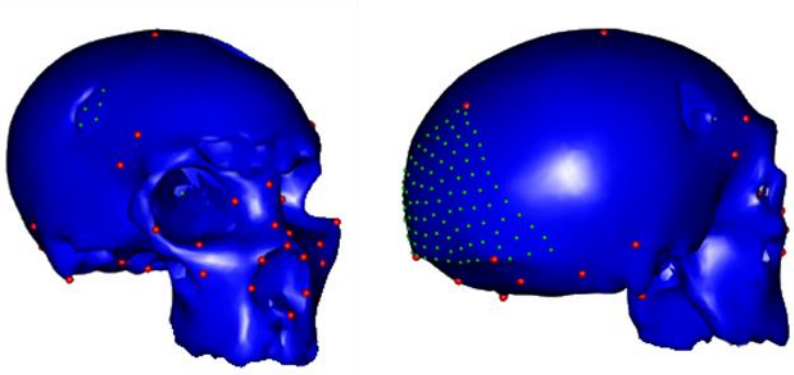

Figure 3.1.11: Graphical output of the smoothing tool applied on the neanderthalian skull of Saccopastore 1.

The best settings found on the 3D model of Saccopastore (fig. 3.1.11) is a smoothing filter of Taubin algorithm (at the first iteration) with the lambda set to 0.15; the percentage of anatomical information recovered is equals to 12.25% (other result specification in Table 3.1.10). The results of all combinations performed is reported in the Table 3.1.11.

Table 3.1.10: Result of the aro.smoo.tool performed on the 3D models of Saccopastore 1.

L-set mean shifting	0.545 mm
L-set range shifting	(0.0578-1.55) mm
CS original model	120.5684
CS decimated model	120.5745
CS smoothed model	120.5725

Table 3.1.11: Detailed results (entail/loss of anatomical information) of the aro.smoo.tool performed on the 3D models of Saccopastore 1 decimated to 20000 triangles.

Iter	tau_0.01	tau_0.05	tau_0.1	tau_0.15	tau_0.2	ang_0.08	ang_0.15	ang_0.22	ang_030
1	-8,52	-4,31	6,52	12,25	0,63	-18,89	-71,50	-135,62	-206,71
2	-19,34	-9,88	9,44	2,68	-62,79	-71,13	-203,56	-341,18	-478,45
3	-28,11	-17,02	10,57	-24,96	-138,71	-133,82	-338,96	-540,76	-736,40
4	-43,09	-21,04	8,59	-60,61	-211,58	-202,28	-472,40	-732,24	-978,28
5	-60,09	-30,69	4,02	-98,88	-282,08	-270,95	-601,83	-914,47	-1197,30
6	-78,45	-41,36	-2,89	-137,98	-349,69	-336,88	-728,19	-1088,48	-1417,95
7	-97,88	-52,92	-11,82	-175,90	-413,88	-402,67	-850,30	-1248,10	-1624,85
8	-117,81	-66,04	-22,34	-213,42	-474,80	-469,74	-968,05	-1410,20	-1822,90
9	-138,53	-80,58	-34,02	-250,49	-532,90	-534,53	-1083,22	-1571,83	-2011,99
10	-159,51	-94,37	-47,02	-286,85	-593,23	-598,59	-1186,39	-1717,68	-2202,09
Iter	ang_0.37	fuj_0.15	fuj_0.29	fuj_0.44	fuj_0.58	fuj_0.73	lap	hcl	
1	-278,36	-18,64	-63,21	-119,68	-181,37	-245,71	-4127,35	-1313,07	
2	-613,04	-61,96	-173,91	-292,53	-408,94	-521,44	-4592,56	-2504,50	
3	-925,18	-114,88	-287,31	-454,71	-611,79	-760,25	-5263,33	-3574,52	
4	-1203,23	-170,62	-395,82	-604,08	-797,29	-979,76	-6095,04	-4554,31	
5	-1479,49	-226,81	-498,74	-744,52	-972,41	-1188,31	-6875,61	-5466,13	
6	-1727,57	-282,47	-596,94	-878,92	-1140,39	-1389,03	-7642,68	-6333,07	
7	-1972,54	-336,83	-691,02	-1007,96	-1303,15	-1583,89	-8387,10	-7194,76	
8	-2204,24	-390,00	-782,69	-1133,89	-1462,43	-1774,86	-9140,10	-8032,43	
9	-2415,26	-441,90	-871,66	-1256,88	-1617,31	-1960,04	-9893,24	-8858,83	
10	-2647,46	-492,36	-958,75	-1377,72	-1769,27	-2140,28	-10616,61	-9675,17	

3.1.7 Guidelines to smooth

As described in the previous subchapters the smoothing algorithms have been developed to counteract the negative effect of faceting produced by both acquisition and simplification of virtual objects. Nevertheless, smoothing algorithms can have detrimental effects. Different algorithms have been built for particular geometric structure: angweight to eliminate severely distorted elements (reduce high angle) (Zhou and Shimada, 2000); taubin for shrinkage reduction (Taubin, 1995). All these types of algorithm are versions less generalist than "Laplace" type from which deriving. The application of algorithms "Laplace" and "HClaplace" involves a large geometric modification of the mesh, causing episodes of shrinkage; furthermore does not present settable parameters. The algorithms "fujiLaplace" and "angWeight" are both scale dependent therefore a same setting applied to a model and its scaled version will bring to a different output for the mesh distance. The "taubin" smoothing algorithm type was conceived to prevent excessive modification of the surface smoothed in the local regions of greater curvature. Usually the only parameter taken in account is the "mesh distance", in paleontological and paleoanthropological studies, between the reference model and its smoothed version, when the quantification of geometric changing is required. Obviously, the mesh distance is the mean distance between the coordinates of the two compared meshes.

The smoothing filter are applied in the paleoanthropological field to reduce the topological artefact due to digital acquisition techniques. As described above the smoothing tool can be used only when a highest resolution model is available in order to acquire the anatomical distance loss during a process of simplification (e.g., decimation, background noise, highest interslice distance). In GM studies semilandmark based a decimation process is desirable jointly to uniform the geometric complexity of comparison sample and to remove topological artefact. In addition, biomechanical studies specifically through Finite Element Analysis (FEA) require a decimation procedure to permits the solving of stationary model tested (e.g., Piras, et al., 2015). The smoothing tool can be used in these studies.

In order to clarify the critical choice of the smoothing algorithm a surface model was separated in 16 patch dividing in an iterative (i=2) process a surface in 4 quarters (fig. 3.1.12). On each single isolated quadrant of surface was applied in a first step the adding of background noise, moving each vertex by a casual distance extracted by a normal distribution centred in 0. Successively each patch was smoothed with the same algorithm settings (reported in Table 3.1.12), the results are reported in the Table 3.1.13.

Table 3.1.12: Smoothing settings (first column) performed on 3D model listed in the first row.

	Skull model	Neanderthal teeth	M499
Iter	2	2	2
Noise	0.025	0.0005	0.0005
Taubin	0.50	0.30	0.30
fujiLaplace	0.05	0.0000001	0.00001
angWeight	0.20	0.0001	0.0001

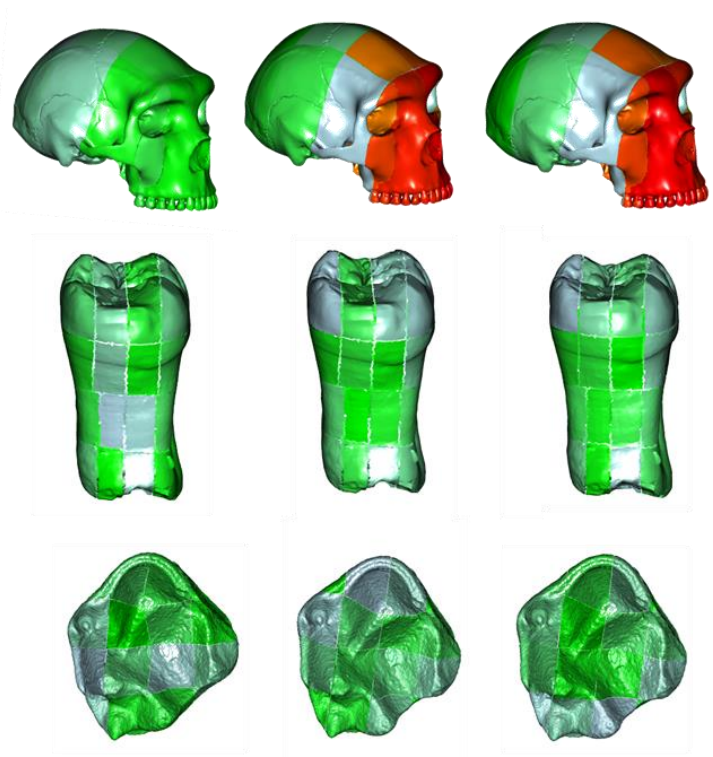

Figure 3.1.12: Graphical representation of the results of the smoothing filters applied on 3D model parcelled in 16 parts.

Table 3.1.13: Detailed results of smoothing procedures (entail/loss of anatomical information) performed on each portion of the 3D models (first row) smoothed with the setting reported in the table 3.1.10.

	Skull model			Neanderthalian teeth			M499		
Patch	T	F	A	T	F	A	T	F	A
1	**35,57**	**37,51**	**51,37**	**17,62**	**14,36**	**18,47**	**14,21**	**16,79**	**4,39**
2	**34,85**	**37,21**	**43,34**	**17,15**	**14,47**	**18,38**	**13,71**	**15,16**	**4,59**
3	**33,63**	**37,97**	**45,81**	**16,65**	**14,31**	**17,90**	**15,15**	**16,45**	**4,49**
4	**35,66**	**36,47**	**39,82**	**16,34**	**14,64**	**18,63**	**14,53**	**15,66**	**4,85**
5	**38,38**	**17,60**	**26,17**	**17,15**	**14,34**	**17,99**	**14,42**	**14,54**	**4,55**
6	**37,86**	**-82,50**	**-67,21**	**16,88**	**14,05**	**17,91**	**14,56**	**17,73**	**4,65**
7	**38,06**	**-48,85**	**-44,65**	**17,77**	**15,08**	**19,34**	**15,67**	**15,28**	**4,89**
8	**39,66**	**-367,83**	**-143,24**	**17,21**	**14,29**	**18,27**	**14,76**	**14,33**	**4,74**
9	**34,43**	**37,03**	**46,15**	**17,92**	**14,62**	**18,88**	**14,92**	**15,03**	**4,38**
10	**35,77**	**36,73**	**40,32**	**15,97**	**15,12**	**18,82**	**14,07**	**15,24**	**4,85**
11	**32,45**	**36,37**	**44,47**	**16,89**	**14,39**	**18,17**	**14,53**	**17,32**	**4,80**
12	**36,20**	**37,68**	**44,03**	**17,16**	**14,43**	**18,54**	**14,49**	**14,78**	**4,45**
13	**38,10**	**-50,16**	**-41,15**	**16,70**	**14,62**	**18,65**	**14,79**	**15,82**	**4,59**
14	**39,72**	**-371,84**	**-142,68**	**16,85**	**14,47**	**18,13**	**14,87**	**14,73**	**4,54**
15	**37,78**	**23,37**	**30,07**	**17,27**	**14,86**	**18,79**	**15,20**	**15,45**	**4,58**
16	**37,74**	**-34,16**	**-33,76**	**17,10**	**13,92**	**17,64**	**15,34**	**18,46**	**4,93**

3.2 Retrodeformation of the Saccopastore 1 cranium

3.2.1. The Saccopastore 1 cranium

Two Neanderthalian fossil crania were found between 1929 and 1935 within the gravels and sands of a quarry near Rome; these were referred to a Late Pleistocene deposit of the last interglacial dated about 130 ka (Breuil and Blanc, 1936, Caloi, et al., 1998, Condemi, 1992, Manzi and Passarello, 1991, Sergi, 1929, Sergi, 1944, Sergi, 1948) and recently re-dated to 250 ka (MIS 7) (Marra, et al., 2015). They are named respectively Saccopastore 1 and Saccopastore 2.

Saccopastore 1 represents a morphotype belong to the wurmian variability of Neanderthals mixed to structures shared with more archaic and less derived European Middle Pleistocene samples (e.g., Arsuaga, et al., 1997). Saccopastore 1 was assigned to an adult female. The skull is almost complete, lacking the mandible and the zygomatic arches. Some damages are localised to the supraorbital region and some dental crowns; in addition, two holes in the vault were produced at the time of the discovery by the cave workers.

The endocranial cavity is partially filled with stone matrix, and the cranial capacity estimated by S. Sergi (1944) is close to 1200 ml – 1174 ml. "The vault shows a marked platicephaly, associated to a rounded occiput. In posterior view, the typically Neandertal elliptical (or en bombe) profile is observed. Facial size of Scp-1 is rather large, without presence of a canine fossa, with pronounced alveolar height, marked orthognathism, and midfacial prognathism. Pyriform aperture is wide, the orbits are large and circular, and the high, broad, and rectangular nasal bones show a gradual but deep curvature in transverse section. The palate is narrow and high, with a palato-dental area and teeth rather small viewed in the range of the Neandertal variability" (Bruner and Manzi, 2006).

3.2.2. Virtual retrodeformation

The quantitative and qualitative analyses of the fossil play a central role in the understanding and study the evolution and adaptation of living or extinct taxa. Vertebrates are, more or less, symmetric with respect to the sagittal plane, which divides the body into a right and left half (Mardia, et al., 2000). In addition to biological asymmetry, a fossil specimen often suffers by "flattening", "bending" and "shearing" that can be viewed as a series of locally affine deformations due to taphonomic processes (Lyman, 1994, Shipman, 1981). In the past, skilled expert anatomist or paleontologists (de León and Zollikofer, 2001, Ogihara, et al., 2006) performed reconstruction and deformation correction manually. The upcoming of computerized tomography (CT) in the last two decades and 3D modelling techniques such as laser scanning and photogrammetry allows for applying different approaches to restore the bilateral symmetry of a digital model (Cunningham, et al., 2014, Weber, 2001). The standard techniques to restore virtually the missing parts is named "virtual restoration" (Gunz, et al., 2009); the protocols to correct the asymmetric between right and left side are called

"symmetrization" (Bookstein and Mardia, 2003, Bookstein, 2005, Mardia, et al., 2000). A common approach, in order to restore symmetry in a digital model, two sets of landmarks are placed, one on each side. The landmark sets are reflected and relabeled in order to compute a symmetric average of both the original and the mirrored set of landmarks, and subsequently the 3D model is warped to the landmark sets thus obtained with Thin-Plate-Spline (TPS) (Bookstein, 1989); this approach can be used to remove uniform shearing (Gunz, et al., 2009). Recently, a non-linear symmetrization method to restore bending and/or compression landmark-based was proposed by Ghosh et al. (2010) and evaluated by Tallman et al. (2014). Both methodological approaches are restricted by the amount of available landmarks that can be reliably placed on both sides, because the number and distribution of landmark affects the quality of the retrodeformation. The denser the landmarks, the better the retrodeformation works, and on all parts of the structure there are landmarks needed to ensure a reasonable retrodeformation.

The cranium of Saccopastore 1 was retrodeformed applying a new protocol developed thanks to the collaboration between the Laboratory of Palaeoanthropology and Bio-Archaeology (Sapienza University in Rome) with the University of Freiburg. The new method involves bilateral semilandmark sets, curves and landmark sets to represent the entirely anatomy of a 3D object allowing a more accurate restoration of symmetry. In particular we used 88 bilateral landmark (44 on each side), 6 curve (140 semilandmark) and 10 patches (438 semilandmark) for 666 anatomical/geometrical points (333 on each side) (fig. 3.2.1).

Remember that a landmark correspond to an anatomical point; a curve is sequence of consecutive point along a close or open outline; a patch of semilandmark is a group of geometrical points.

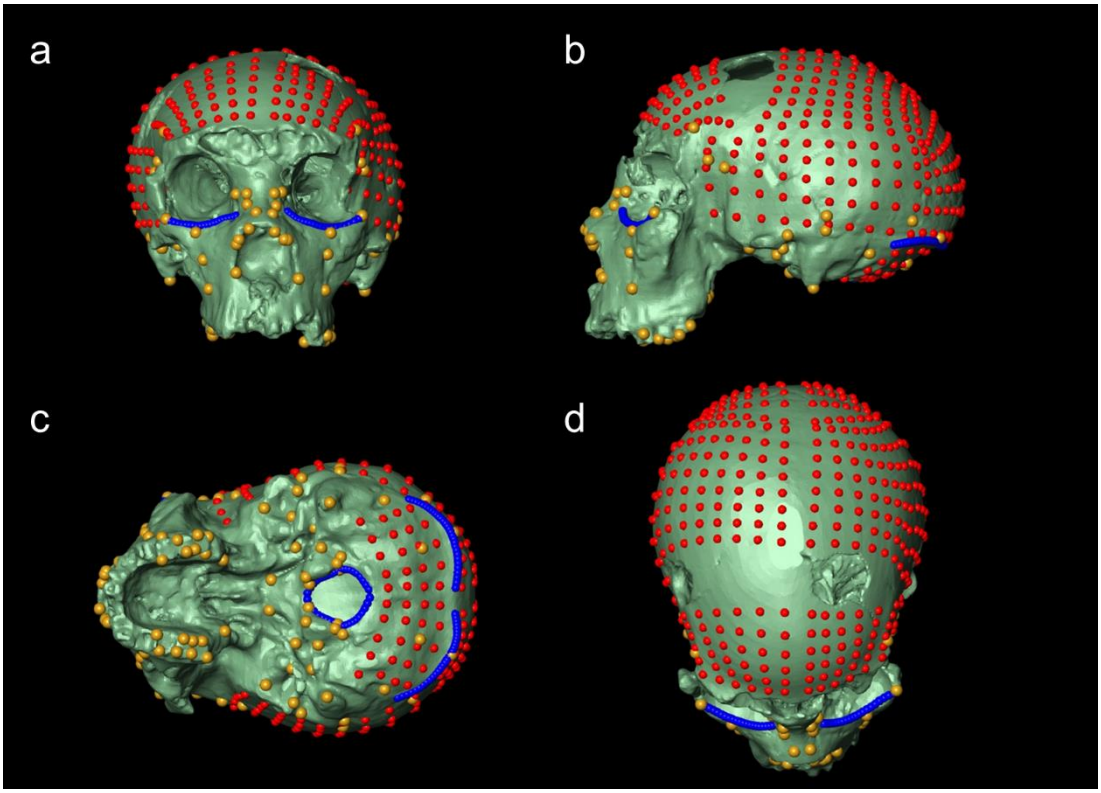

Figure 3.2.1: Landmark (in yellow), curve semilandmark (in blue) and patch semilandmark (in red) sets used to the retrodeformation procedure of the skull of Saccopastore 1 showed in frontal (a), lateral (b), basal (c) and superior views.

3.2.3. Models comparison

In the table 3.2.1 are reported the distance between the 44 landmark pairs while in the figure 3.2.2 is shown the vector distances between the original and retro-deformed models. As shown in figure 3.2.2 the principal axes of variation, due to taphonomic processes, crosses the region of left parietal, portions of mastoid region of right temporal bone and part of the right side of maxilla, suggesting that a phenomenon of compression occurred during post-depositional processes.

Number	Original (mm)	Correct (mm)	Number	Original (mm)	Correct (mm)
1	103,48	107,07	23	131,24	135,15
2	46,44	48,44	24	48,21	49,25
3	62,95	65,53	25	105,08	107,98
4	48,72	50,54	26	64,46	66,12
5	46,34	48,05	27	37,86	39,10
6	59,18	61,77	28	26,94	28,52
7	63,95	66,66	29	24,06	25,57
8	13,73	14,74	30	71,19	73,95
9	101,19	104,33	31	61,10	63,68
10	123,95	127,85	32	65,50	68,22
11	112,23	115,66	33	8,56	9,57
12	103,12	105,91	34	14,94	16,17
13	16,19	16,12	35	14,36	15,73
14	34,69	35,31	36	23,86	25,40
15	50,78	51,94	37	93,51	96,33
16	80,04	82,42	38	40,82	41,74
17	23,70	23,97	39	99,66	102,67
18	51,42	52,47	40	40,23	41,32
19	12,87	12,38	41	60,14	62,66
20	28,92	29,40	42	33,14	34,52
21	74,90	76,91	43	110,39	113,84
22	136,29	140,32	44	106,80	110,13

Table 3.2.1: Distances in mm between the right and left landmark set on the original and retrodeformed model of Saccopastore 1.

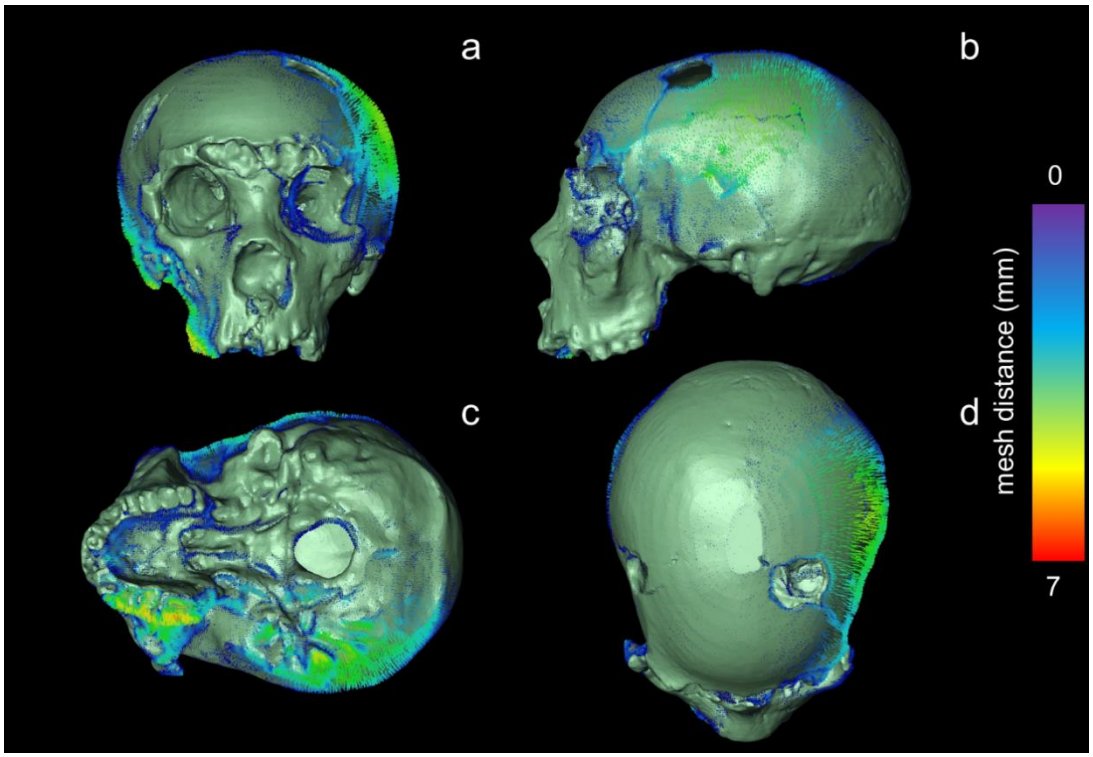

Figure 3.2.2: Vector of mesh distance computed between the retrodeformed and original skull models of Saccopastore 1 showed in frontal (a), lateral (b), basal (c) and superior views, besides is reported the legend (rainbow palette).

3.3 The Neanderthal-like frontal bone from the Po Valley

3.3.1 Introduction

The specimen, nicknamed "Pàus", consists of the almost complete frontal bone of an adult individual (fig. 3.3.1), found on a sand bar of the left bank of the river, probably carried by the current from the upstream Middle-Late Pleistocene deposits. Its discovery was made casually, thanks to a passionate amateur. Actually is preserved in the Museo Paleoantropologico of San Daniele Po near Cremona. This frontal bone represents the unique non-modern human fossil evidence discovered so far in the Po valley. Pàus was found on the left bank of the river Po, probably the specimen has been transported from the sedimentary deposition placed on Adda or Po River, up to the secondary formation (fig. 3.3.1). Its particular coloration is due to the oxidation of iron sulphides, the rust coloration is more evident on the spongy tissue. Neither lithic tools nor faunal remains were found in association with the human finding. Nevertheless, a very abundant fossil fauna came from the same area in the past (Bona and Corbetta, 2009), and is mainly characterized by cold-adapted Mammals (e.g., *Mammuthus primigenius*, *Megaloceros giganteus*, *Stephanorhinus kirchbergensis*, *Elephas antiquus*).

On 2013 was carried out a CT-scan with a resolution of 0.625 mm in Rome before to bone sample removal for ancient DNA studies. Subsequently thanks to the collaboration with the International Centre for Theoretical Physics in Trieste was performed an X-ray microtomography (μCT) and the final volume was reconstructed with an isotropic voxel size of 41 μm.

The human frontal bone appears somewhat modified in its exocranial aspect by taphonomic actions related to water transport and sediment erosion, while its inner surface is better preserved, suggesting that it remained protected for a certain period of time, before its separation from the other cranial bones and from the sediment. This is also evident from the information of curvature shown in the figure for the inner and outer portions. The specimen is broken anteriorly, in correspondence of an area around the glabella, lacking the nasal spine and most of the orbital plate; nevertheless, it preserves the superior and middle-lateral components of the supraorbital torus and large part of the sinuses. Laterally and posteriorly the sutures have been only partially worn. The endocranial morphology is well distinguishable; it notably includes the superior sagittal sulcus and the frontal crest, while some convolutions and sulci of the frontal lobe of the brain are also visible (fig. 3.3.2).

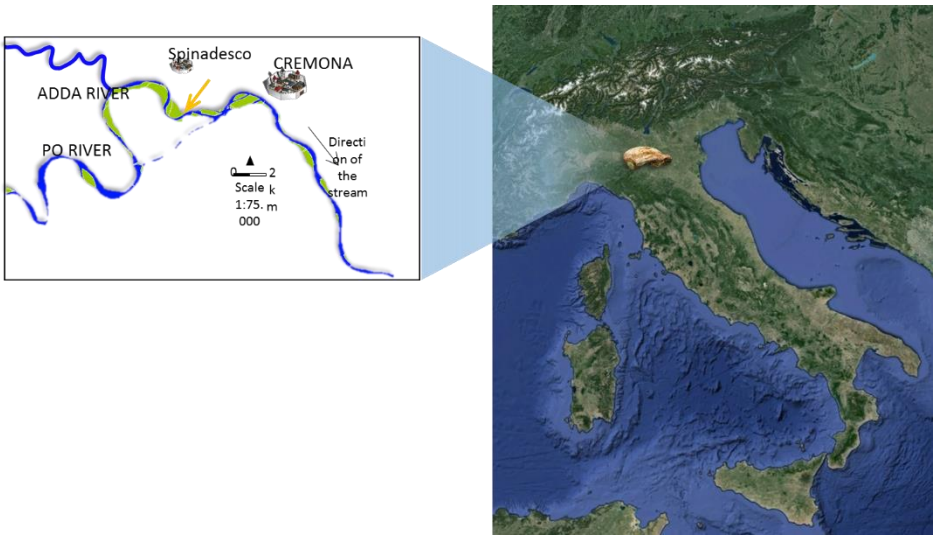

Figure 3.3.1: Place of the discovery of the human fossil specimen (Pàus).

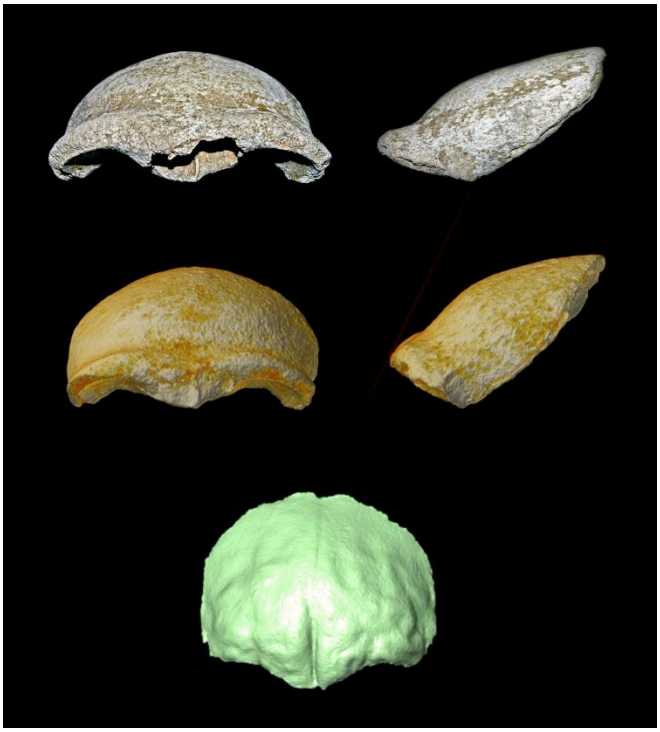

Figure 3.3.2: The Pàus frontal bone specimen: above pictures of the original specimen, in the middle and below are reported respectively the rendering for the esocranial and endocranial surfaces.

In Hominins, the pattern of the frontal bulging detects a taxonomic significance (Bruner, et al., 2013); the curvature of the midsagittal profile can be quantified as the ratio between the chord and the arc.

The aim of this study is to analyse, by applying methods of GM and multivariate analysis, the overall and midsagittal morphology of Pàus and compared with those of a comparative sample including *Homo ergaster*, *Homo heidelbergensis*, *Homo erectus*, *Homo neanderthalensis* and *Homo sapiens* specimens.

For the first time has been applied on a case-study the smoothing tool illustrated and discussed in the subchapter 3.1.

3.3.2 The midsagittal curvature of the frontal bone

The comparative sample consists of 54 specimens belonging to *Homo ergaster* (N=2), *Homo erectus* (N=5), *Homo heidelbergensis* (N=9), *Homo neanderthalensis* (N=8) and *Homo sapiens* (N=30) species (Table 3.3.2). The sex of the specimens was not taken into account. The midsagittal profile of the frontal bone has been acquired from the supratoral sulcus to the bregma through the definition on 21 evenly spaced semilandmark after the acquisition of a surface path in Amira. Successively, the arc was divided into three portion in order to detect the curvature on each trait. The boxplots of the values species pooled of the ration between chord and arch are reported in figure 3.3.3-4. The differences between the values observed in *Homo sapiens*, *Homo neanderthalensis*, *Homo heidelbergensis* and *Homo erectus* were been evaluated using the Wilcoxon test (Wilcoxon and Wilcox, 1964) (Table 3.3.1).

Table 3.3.1: Wilcoxon test performed on paired species for the three midsagittal frontal traits. ERE=*Homo erectus*, HEI= *Homo heidelbergensis*; NEA= *Homo neanderthalensis*; SAP= *Homo sapiens*.

1st, 2nd,3rd traits	ERE	HEI	NEA	SAP
ERE	-			
HEI	0.519	-		
NEA	0.833	0.481	-	
SAP	**<0.001**	**<0.001**	**<0.001**	
1st trait	ERE	HEI	NEA	SAP
ERE	-			
HEI	0.898	-		
NEA	**0.002**	**0.036**	-	
SAP	**<0.001**	**<0.001**	**<0.001**	-
2nd trait	ERE	HEI	NEA	SAP
ERE	-			
HEI	0.112	-		
NEA	0.943	**0.093**	-	
SAP	0.141	**0.001**	0.265	-
3rd trait	ERE	HEI	NEA	SAP
ERE	-			
HEI	0.519	-		
NEA	0.222	**0.027**	-	
SAP	**0.054**	0.107	**<0.001**	-

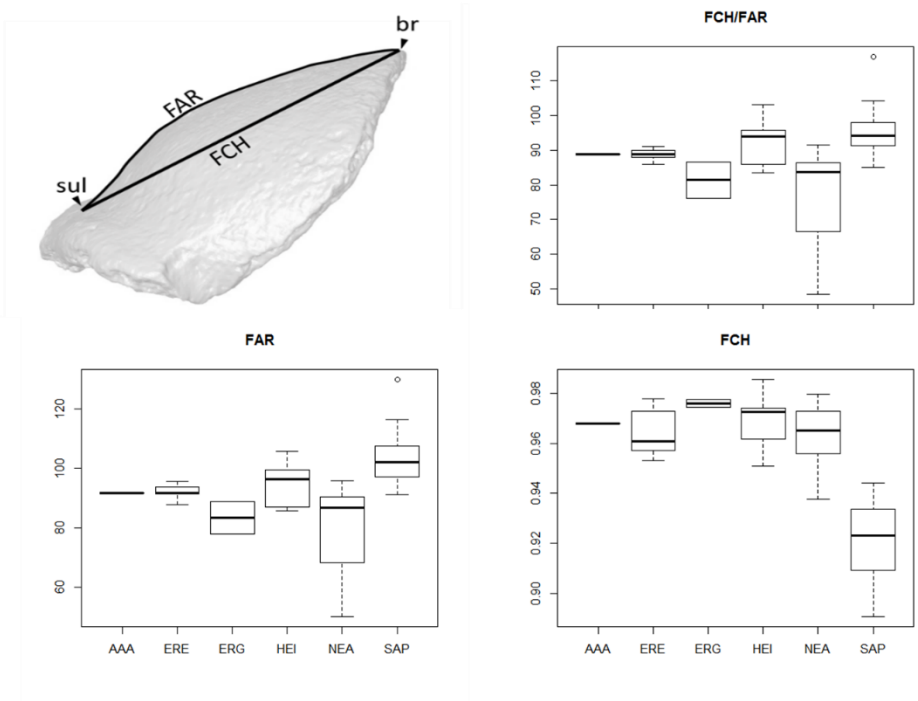

Figure 3.3.3: Schematic picture of the acquisition of arch (FAR) and chord (FCH) acquired between the deepest midpoint on the supratoral depression (sul) and bregma (br). The boxplots relative the FCH, FAR and FCH/FAR species pooled are reported.

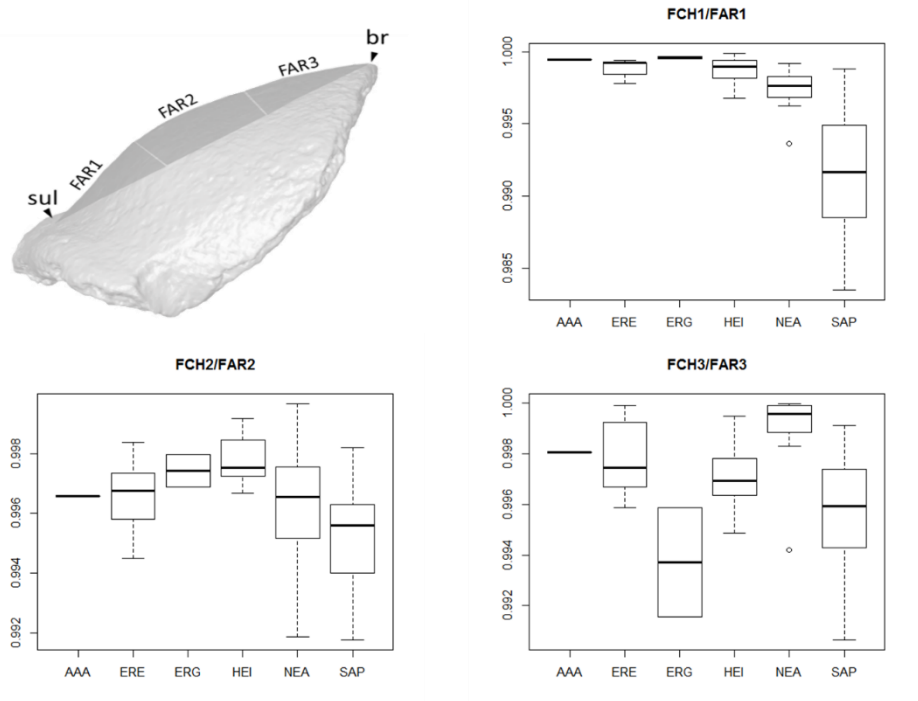

Figure 3.3.4: Schematic picture of the acquisition of arch (FAR) and chord (FCH) acquired on each trait of the frontal midsagittal profile. The boxplots relative to the ratio between FCH and FAR species pooled are reported.

Table 3.3.2: Sample used in this study in traditional and geometric morphometrics (frontal squama and frontal midsagittal profile).

Specimen	Species	OTU	Metric	GM (midsagittal)	GM (frontal squama)
Pàus		PAU	*	*	*
Ngandong 7	*Homo erectus*	ERE	*	*	*
Ngandong 12	*Homo erectus*	ERE	*	*	*
Sambungmacan 3	*Homo erectus*	ERE	*	*	*
Zhoukoudian 8	*Homo erectus*	ERE	*	*	*
Zhoukoudian EI 3	*Homo erectus*	ERE	*	*	*
D2280	*Homo ergaster*	ERG	*	*	*
KNM-ER 3883	*Homo ergaster*	ERG	*	*	*
Arago XXI	*Homo heidelbergensis*	HEI	*	*	*
Bodo	*Homo heidelbergensis*	HEI	*	*	*
Ceprano	*Homo heidelbergensis*	HEI	*	*	*
Dali	*Homo heidelbergensis*	HEI	*	*	*
Jebel Irhoud 1	*Homo heidelbergensis*	HEI	*	*	*
Kabwe	*Homo heidelbergensis*	HEI	*	*	*
LH18	*Homo heidelbergensis*	HEI	*	*	*
Petralona	*Homo heidelbergensis*	HEI	*	*	*
Saldhana	*Homo heidelbergensis*	HEI	*	*	*
SH4	*Homo heidelbergensis*	HEI	*	*	*
Amud 1	*Homo neanderthalensis*	NEA	*	*	*
Le Chapelle	*Homo neanderthalensis*	NEA	*	*	*
Le Moustier 4	*Homo neanderthalensis*	NEA	*	*	*
Neanderthal 1	*Homo neanderthalensis*	NEA	*	*	*
Shanidar 1	*Homo neanderthalensis*	NEA	*	*	*
Spy 1	*Homo neanderthalensis*	NEA	*	*	*
Spy 2	*Homo neanderthalensis*	NEA	*	*	*
Tabun	*Homo neanderthalensis*	NEA	*	*	*
Bolognese 2524	*Homo sapiens*	SAP	*	*	*
Bolognese 2525	*Homo sapiens*	SAP	*	*	*
Bolognese 2526	*Homo sapiens*	SAP	*	*	*
Bolognese 2527	*Homo sapiens*	SAP	*	*	*
Bolognese 2528	*Homo sapiens*	SAP	*	*	*
Bolognese 2529	*Homo sapiens*	SAP	*	*	*
Bolognese 2530	*Homo sapiens*	SAP	*	*	*
Bolognese 2531	*Homo sapiens*	SAP	*	*	*
Bolognese 2532	*Homo sapiens*	SAP	*	*	*
Bolognese 2533	*Homo sapiens*	SAP	*	*	*
Bolognese 2534	*Homo sapiens*	SAP	*	*	*
Bolognese 2535	*Homo sapiens*	SAP	*	*	*
Bolognese 2536	*Homo sapiens*	SAP	*	*	*
Bolognese 2537	*Homo sapiens*	SAP	*	*	*
Bolognese 2538	*Homo sapiens*	SAP	*	*	*
Bolognese 2539	*Homo sapiens*	SAP	*	*	*
Bolognese 2540	*Homo sapiens*	SAP	*	*	*
Bolognese 2541	*Homo sapiens*	SAP	*	*	*
Bolognese 2542	*Homo sapiens*	SAP	*	*	*
Bolognese 2543	*Homo sapiens*	SAP	*	*	*
Bolognese 2544	*Homo sapiens*	SAP	*	*	*
Bolognese 2545	*Homo sapiens*	SAP	*	*	*
Bolognese 2546	*Homo sapiens*	SAP	*	*	*
Bolognese 2547	*Homo sapiens*	SAP	*	*	*

Bolognese 2548	*Homo sapiens*	SAP	*	*	*
Bolognese 2549	*Homo sapiens*	SAP	*	*	*
Bolognese 2550	*Homo sapiens*	SAP	*	*	*
Bolognese 2551	*Homo sapiens*	SAP	*	*	*
Bolognese 2552	*Homo sapiens*	SAP	*	*	*
Bolognese 2553	*Homo sapiens*	SAP	*	*	*

The curvature of the entire midsagittal profile (fig. 3.3.3) of the frontal bone discriminates the species *Homo sapiens* from the other taxonomic units considered in this study. It is interesting the significance difference in the third trait (in proximity of the bregma) (fig. 3.3.4) between *Homo heidelbergensis* and *Homo neanderthalensis*. The latter presents the flatter last trait between the species considered, and Pàus is characterized by ad intermediate curvature between the species *Homo neanderthalensis* and *Homo heidelbergensis*.

3.3.3 The sample and the (semi) landmark configurations

The midsagittal profile was acquired by defining a continuous curve ranging from the median landmark lying on the deepest point of the supratoral depression to the bregma. The vertices of points forming each 3D curve were set up as intermediate point for the definition of a Bèzier curve and the subsequent definition of acquired 21 evenly spaced landmark.

Table 3.3.3: Landmark description

Landmark	Side	Definition
Sul	Middle	The deepest point on the supratoral depression along the midsagittal plane
Br	Middle	The intersection between the coronal and the sagittal suture
Ft	R/L	The point where the temporal line reaches its most anteromedial position on the frontal
Uo	R/L	The upper point on the orbital margin

The landmarks, thus obtained merged to the four lateral landmark (the upper point on the orbital margin and the fronto-temporal point on left/right sides). The set of 25 landmarks (4 landmark + 21 curve semilandmark) were used for the GPA (fig. 3.3.5). The 21 semilandmark (except the first and the last on the curve) have been slid minimizing the bending energy (Gunz, et al., 2005).

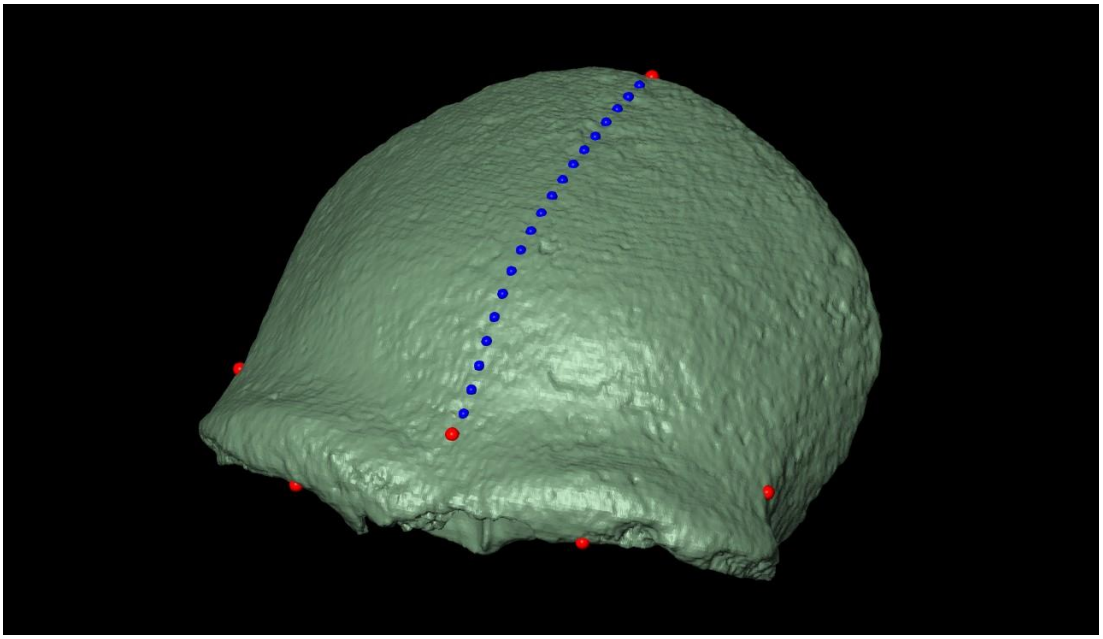

Figure 3.3.5: The landmark (in red) and curve semilandmark (in blue) sets showed on Pàus.

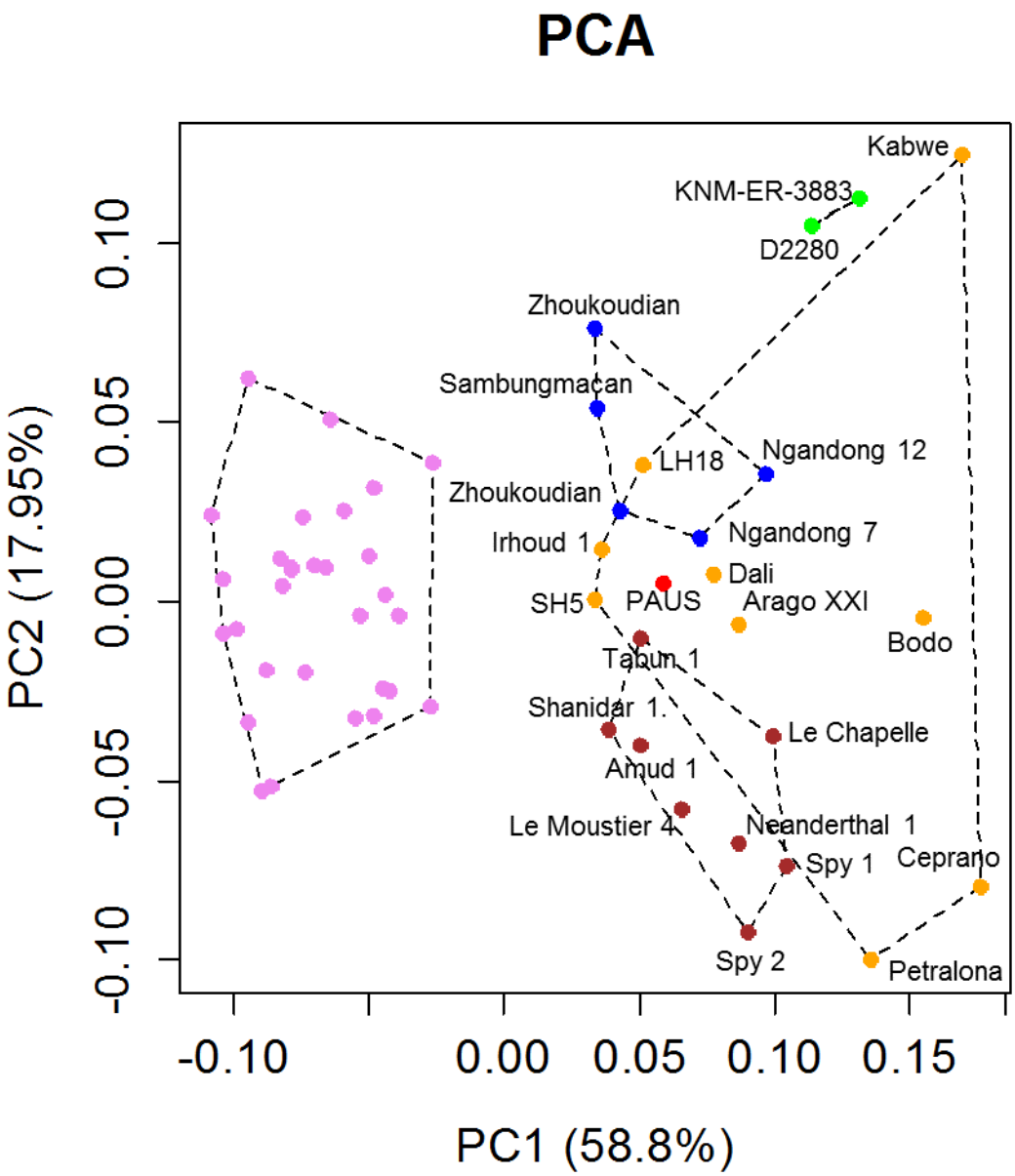

Figure 3.3.6: Plot of the first two Principal Components. For illustrating purpose the convex hull for species are reported (Fuchsia = *H. sapiens*; blue = *H. erectus*; red = Paus: brown = *H. neanderthalensis*; orange = H.heidelbergensis; green = H. ergaster).

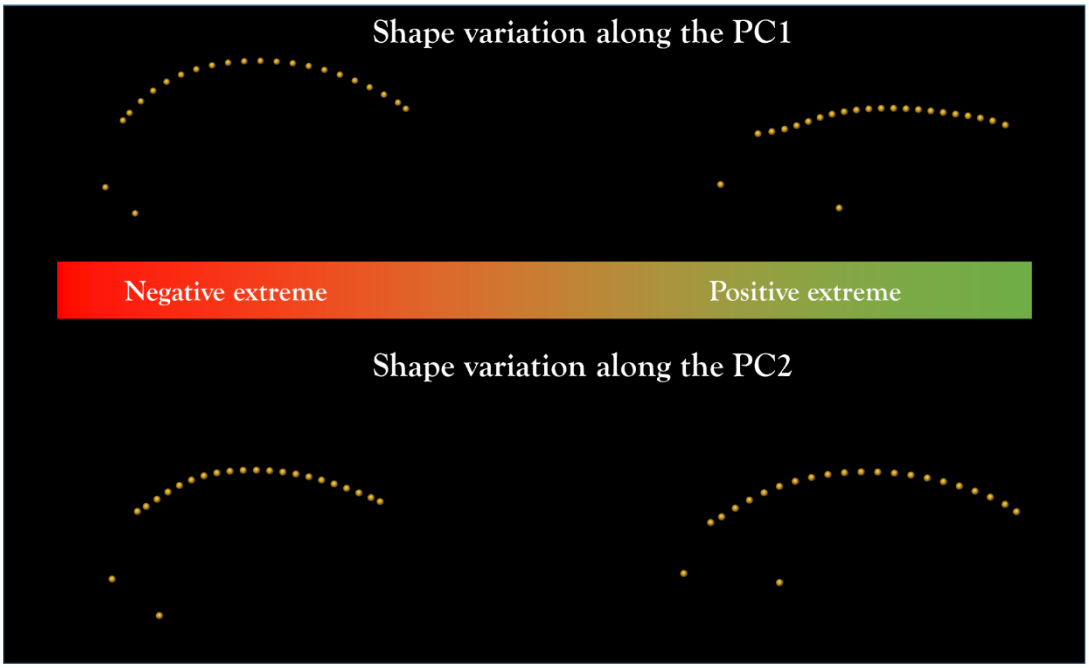

Figure 3.3.7: In the picture are reported the shape variation associated to extreme values observed in the range for the first principal components.

The shape analysis performed on the sagittal profile detects mainly the variations on the supratoral sulcus and the frontal bulging pattern. Specimens placed to negative values for the PC1 are characterize by the presence of a soft supratoral depression and a bulging developed in the anterior trait. The shape variations related to positive values of PC1 corresponding to specimens characterized by a marked supratoral depression and absence of frontal bulging. Along the PC1 the cluster related to *Homo sapiens* sub-sample is located on negative values, while the specimens of Kabwe (*Homo heidelbergensis*), D2280 (*Homo erectus*) and KNM ER 3883 (*Homo ergaster*) are situated at the positive extreme (fig. 3.3.6). The PC2 discriminates the Neanderthal morphology from those of other species. In fact at the positive extreme values of PC2 are combined to the presence of a marked supratoral depression and at the same time a frontal bulging developed in the middle trait, with a less curvature of the midsagittal profile in the trait near the bregma. The Pàus specimen is located between the clusters of *Homo neanderthalensis* (close to the specimens of Shanidar 1, Amud 1 and Tabun) and *Homo heidelbergensis* (fig. 3.3.6).

The morphology of the frontal squama of Pàus was analyse through the definition of 6 anatomical landmark (Table 3.3.3) and the building of a set of 100 semilandmark (function mesh2set of the "ctrlR" package). Before proceeding with the analysis, the damaged specimen have been restored through the TPSi and surface warping algorithms (Table 3.3.4).

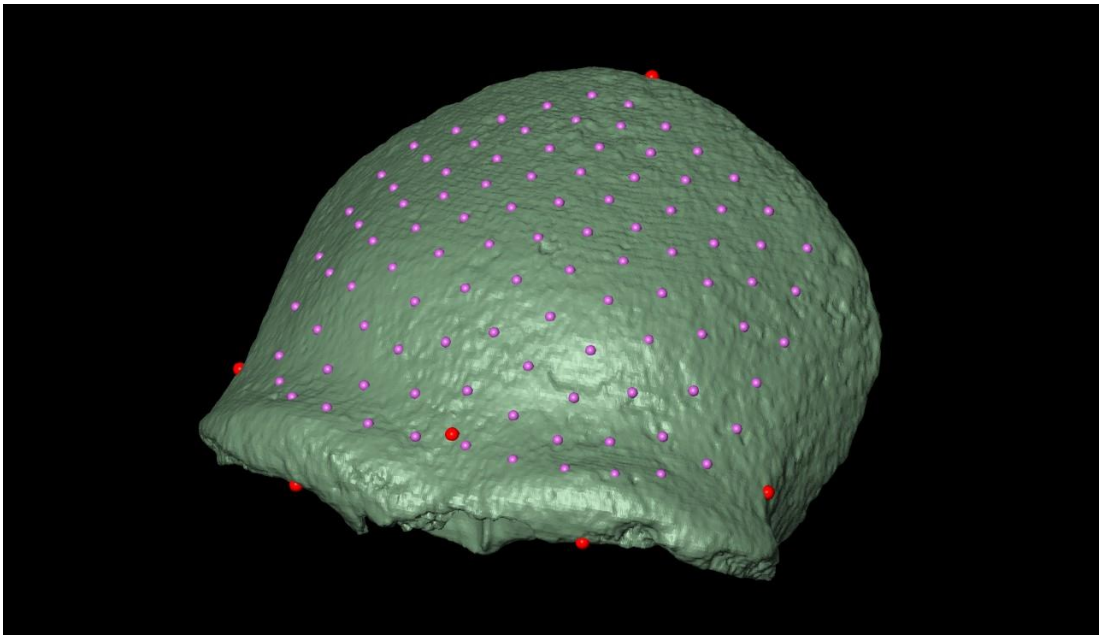

Figure 3.3.5: The landmark (in red) and semilandmark (in fuchsia) sets showed on Pàus.

A preliminary procedure was performed on each digital model using the following protocol (see R `sliding.protocol` demo):

- ✓ restoration of the missing portions;
- ✓ application of the algorithm `aro.smoth.tool` decimating the original 3D mesh (frontal squama) to 20000.

As mentioned above, a set of 100 semilandmark placed on the frontal squama was used in the multivariate analysis for the morphological study. In particular, the semilandmark set was built on the external surface of Pàus using the function `mesh2set` ("ctrlR" package). The semilandmark set and the Pàus 3D model were used as reference to place the set of 100 points (R function `placePatch` in Morpho package) (Schlager, 2013) on each specimen using the 6 homologous landmarks. Then, the SL-set placed on each specimen was subjected to sliding (Gunz, et al., 2005) (R function `slider3d` in Morpho package) (Schlager, 2014).

Table 3.3.4: Summary of the study sample (frontal midsagittal profile and squama) including the taxonomic allocation (OTU) and preliminary analyses done on mesh (decimation/smoothing and virtual restoration).

Specimen	OTU	Algorithm	Par.	Iter	Anatomical retrieval (%)	Restoration Type
Pàus	PAU	Tau	0.01	3	4.73	-
Ngandong 7	ERE	Fuj	0.06	1	20.01	-
Ngandong 12	ERE	Fuj	0.06	1	29.82	-
Sambungmacan 3	ERE	Fuj	0.01	1	0.57	-
Zhoukoudian 8	ERE	Tau	0.06	2	7.47	-
Zhoukoudian EI 3	ERE	Tau	0.02	1	0.06	-
KNM-ER 3883	ERG	Tau	0.11	9	12.12	-
D2280	ERG	-	-	-	-	-
Arago XXI	HEI	Fuj	0.19	1	7.78	-
Bodo	HEI	Ang	0.08	2	36.65	
Ceprano	HEI	Tau	0.01	1	4.62	TPS
Dali	HEI	Tau	0.01	3	14.55	-
Jebel Irhoud 1	HEI	-	-	-	-	-
Kabwe	HEI	-	-	-	-	-
LH18	HEI	-	-	-	-	-
Petralona	HEI	Tau	0.05	1	1.73	
Saldhana	HEI	Tau	0.10	3	9.89	-
SH5	HEI	Tau	0.05	1	8.51	-
Amud 1	NEA	Fuj	0.57	5	0.63	-
Le Chapelle	NEA	Tau	0.10	5	21.42	TPS
Guattari	NEA	Tau	0.15	1	6.45	Mirroring
Le Moustier 4	NEA	Fuj	0.57	1	8.57	TPS
Neanderthal 1	NEA	Ang	0.03	1	2.80	TPS
Shanidar 1	NEA	Tau	0.10	10	6.02	Fill
Spy 1	NEA	Tau	0.10	4	9.21	-
Spy 2	NEA	Tau	0.10	3	6.89	TPS
Tabun	NEA	Tau	0.01	1	0.17	TPS
Bolognese 2524	SAP	Tau	0.10	2	3.83	-
Bolognese 2525	SAP	Tau	0.15	1	2.81	-
Bolognese 2526	SAP	-	-	-	-	-
Bolognese 2527	SAP	Tau	0.15	2	5.40	-
Bolognese 2528	SAP	Tau	0.05	2	2.63	-
Bolognese 2529	SAP	Tau	0.01	1	1.15	-
Bolognese 2530	SAP	Tau	0.05	2	2.18	-
Bolognese 2531	SAP	Tau	0.05	4	5.72	-
Bolognese 2532	SAP	-	-	-	-	-
Bolognese 2533	SAP	Tau	0.10	7	17.29	-
Bolognese 2534	SAP	Fuj	0.06	1	3.61	-
Bolognese 2535	SAP	Tau	0.15	4	4.55	-
Bolognese 2536	SAP	Tau	0.15	3	18.35	-
Bolognese 2537	SAP	Ang	0.03	1	10.77	-
Bolognese 2538	SAP	Tau	0.10	2	0.77	-
Bolognese 2539	SAP	-	-	-	-	-
Bolognese 2540	SAP	Tau	0.10	10	10.08	-
Bolognese 2541	SAP	Tau	0.15	5	18.45	-
Bolognese 2542	SAP	-	-	-	-	-
Bolognese 2543	SAP	Ang	0.05	3	36.16	-
Bolognese 2544	SAP	Tau	0.05	4	5.78	-
Bolognese 2545	SAP	Ang	0.04	2	38.11	-
Bolognese 2546	SAP	Tau	0.10	7	8.66	-

Specimen	OTU	Algorithm	Par.	Iter	Anatomical retrieval (%)	Restoration Type
Bolognese 2547	SAP	Tau	0.20	1	8.30	-
Bolognese 2548	SAP	Tau	0.15	3	23.25	-
Bolognese 2549	SAP	Fuj	0.05	1	16.51	-
Bolognese 2550	SAP	Tau	0.01	2	6.23	-
Bolognese 2551	SAP	Ang	0.03	1	2.04	-
Bolognese 2552	SAP	Ang	0.03	1	9.48	-
Bolognese 2553	SAP	Tau	0.10	4	3.51	-

The 55 semilandmark configurations, after GPA, were subjected to the PCA. To the first two PCs are associated respectively with 52.36% and 27.06% of the total variance.

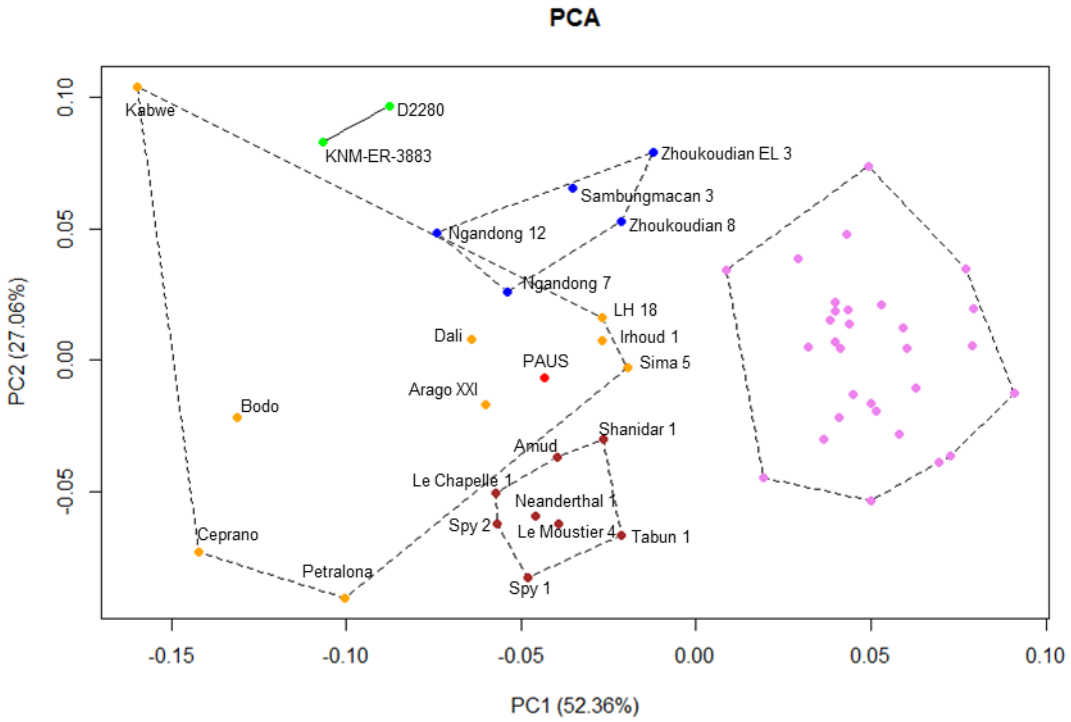

Figure 3.3.9: Plot of the first two Principal Components. For illustrating purpose the convex hull for species are otreported (Fuchsia = *H. sapiens*; blue = *H. erectus*; red = Paus: brown = *H. neanderthalensis*; orange = H.heidelbergensis; green = H. ergaster).

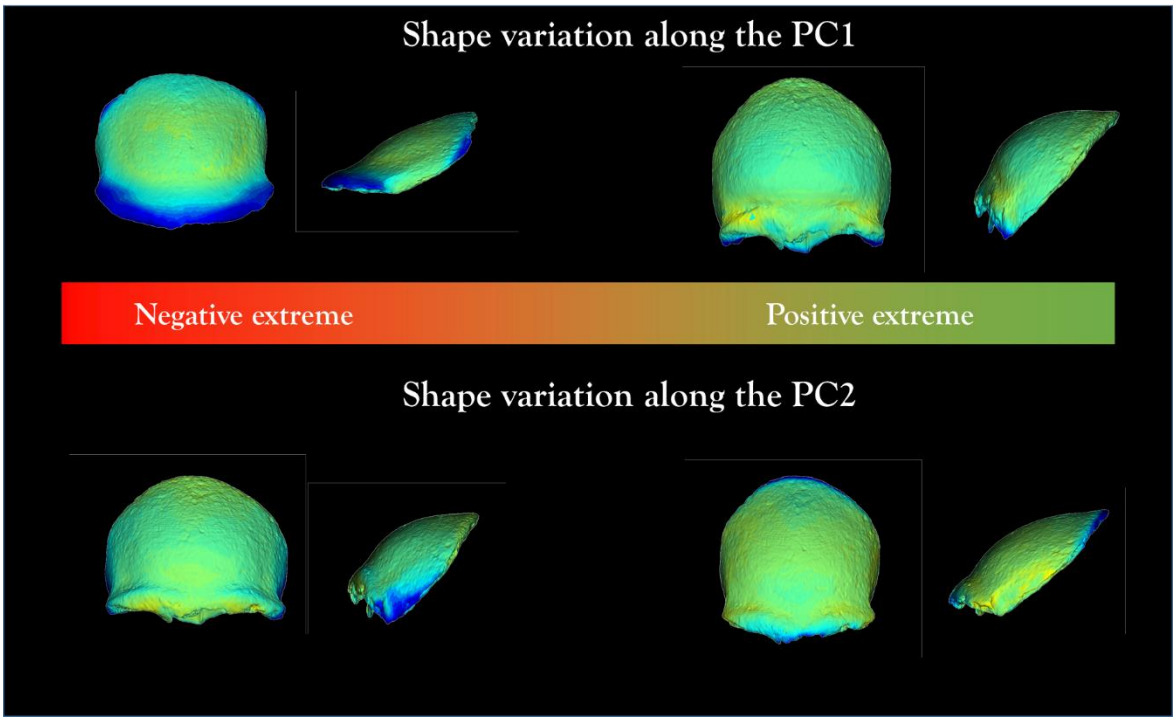

Figure 3.3.10: In the picture are reported the Pàus specimen warped to the extreme values observed in the range for the first principal components.

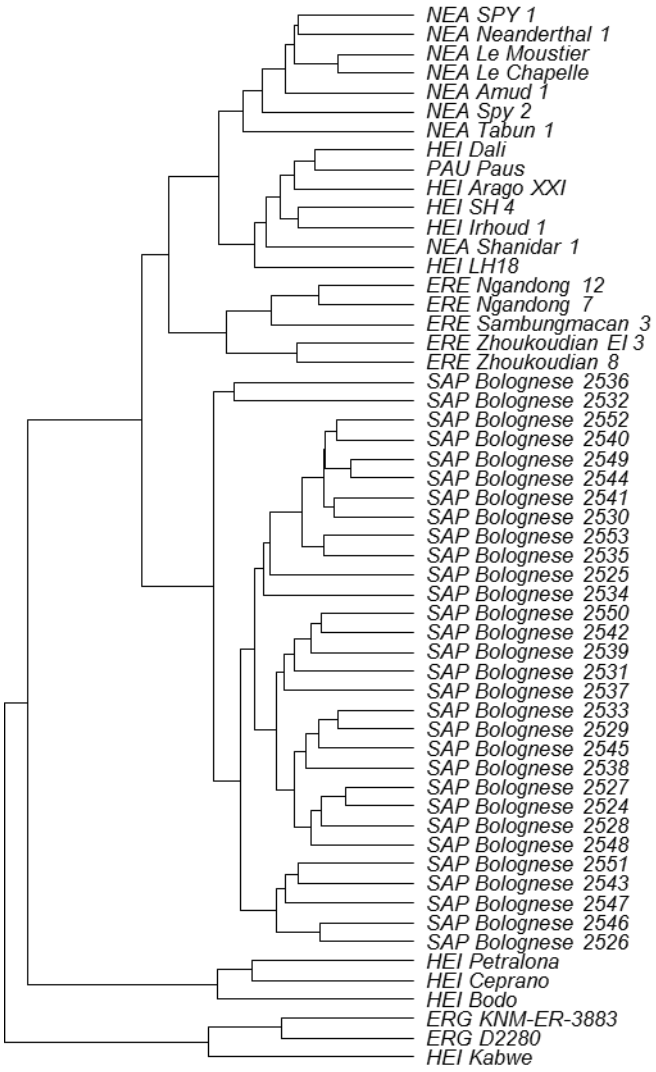

Figure 3.3.11: Cluster analysis (UPGMA) rooted (on KNM-ER-3883) performed on the shape of the frontal squama.

In the plot of the first two PCs (fig. 3.3.9-11) the groups for *Homo sapiens* and *Homo neanderthalensis* are separated from and nonoverlapped with the other clusters. The *Homo sapiens* cluster is placed to positive values for PC1 while other groups are positioned into negative values for this PC. The Neanderthal falls at positive values for PC2. Variabilities of *Homo erectus* and *Homo heidelbergensis* are partially overlapped, while the specimen from Dmanisi and the KNM-ER 3883 are external to variability of other groups. Regarding Pàus its morphospace is close to those *Homo neanderthalensis* and *Homo heidelbergensis*; in detail the values of PC1 and PC2 of Pàus are next to Jebel Irhoud, Sima de los Hueos 4, Shanidar and Amud.

The cluster of *Homo sapiens* is characterized by positive values for PC1 and negative for PC2; these values are associated to the presence of the frontal bulging in the middle region (along the midsagittal profile). Along the PC2, the values of *Homo sapiens* and *Homo neanderthalensis* groups are well separated; in fact in association to negative values of PC2 (*Homo sapiens*) is recorded the presence of the frontal bulging on the middle region, while for positive values (*Homo neanderthalensis*) the frontal bulging is located on the first trait between the curve ranged from the supratoral depression to the bregma. The PC1 discriminates the specimens characterized by a flat morphology of the frontal squama (e.g., Kabwe, KNM-ER 3733, D2280) along negative values, while on positive values the squama of the frontal bone is rounded.

3.4 The Gombore 2 cranial fragments

3.4.1 Introduction

African archaic humans dated to around 1,0 Ma share morphological affinities with *Homo ergaster* and appear distinct in cranio-dental morphology from those of the Middle Pleistocene that are referred to *Homo heidelbergensis*. This observation suggests a taxonomic and phylogenetic discontinuity in Africa that ranges across the Matuyama/Brunhes reversal (780 ka). Yet, the fossil record between roughly 900 and 600 ka is notoriously poor. In this context, the Early Stone Age site of Gombore II, in the Melka Kunture formation (Upper Awash, Ethiopia), provides a privileged case-study. In the Acheulean layer of Gombore II, somewhat more recent than 875 ± 10 ka, two large cranial fragments were discovered in 1973 and 1975 respectively: a partial left parietal (Melka Kunture 1) and a right portion of the frontal bone (Melka Kunture 2), which probably belonged to the same cranium. We present here the first detailed description and computer-assisted reconstruction of the morphology of the cranial vault pertaining to these fossil fragments.

The human fossil record bracketed between roughly 900 and 600 ka in sub-Saharan Africa is notoriously poor. Earlier cranial specimens such as the calvaria known as Daka in the Ethiopian region of the Middle Awash (Asfaw, et al., 2002, Gilbert and Asfaw, 2008), the cranium from Buia in the Eritrean Danakil depression (Abbate, et al., 1998, Macchiarelli, et al., 2004) and the cranial bone fragments from Olorgesaile in Kenya (Potts, et al., 2004), all dated around 1,0 Ma, share morphological affinities with *Homo ergaster*, despite signs of an advanced degree of encephalisation, with enlarged braincase and more vertical parietal walls.

At the same time, these African specimens of the late Early Pleistocene are different from those of the Middle Pleistocene that exhibit, in Africa as elsewhere, a variable combination of archaic and derived morphologies, including further broadening of the cranial vault, less flattened midsagittal profile, peculiar morphology of the supraorbital torus (e.g., Mounier, et al., 2011, Rightmire, 1998, Stringer, 2012). Humans of the Middle Pleistocene are therefore commonly ascribed to a different species referred to as *Homo heidelbergensis*. In a more speciose scenario, as far as the African fossil record is concerned, the nomen *Homo rhodesiensis* applies to specimens such as Bodo, Kabwe and Saldanha (or Elandsfontein), which are followed by more derived humans that are sometimes referred to another different deme (corresponding, at least in part, to the controversial *Homo helmei*; see Rightmire (2009), from which *Homo sapiens* probably emerged.

The taxonomic discontinuity occurring in Africa at the boundary between Early and Middle Pleistocene has a counterpart in Europe with the disappearance of *Homo antecessor*, as it has been described on the sample from Gran Dolina of Atapuerca in Spain (De Castro, et al., 1997)followed by the diffusion of a new kind of humans bearing the Acheulean and commonly referred to (not without controversies; e.g., (Balter, 2014) as

Homo heidelbergensis. Therefore, the time span around the Matuyama/Brunhes reversal of 780 ka should be regarded as a crucial time span for human evolution (Bastir, et al., 2011, Manzi, 2012), as it is also suggested by inferences based on mtDNA data (e.g., Green, et al., 2008, Krause, et al., 2010).

In this context, one of the localities in the Melka Kunture area (Upper Awash, Ethiopia) provides some relevant fossil remains. This is the Acheulean site of Gombore II, dated to about 850 ka, where two large cranial fragments were found in 1973 and 1975 respectively. Since their discovery, these fossil specimens have been considered as belonging to the same cranium and provide evidence for significant components of the morphology of the parietal and frontal bones respectively. In this paper, we provide the first detailed description of the two human specimens from Gombore II, a GM comparative analysis of their phenetic affinities, and a computer-assisted reconstruction of the morphology of the braincase that the two cranial fragments represent.

Gombore II is in the Melka Kunture archaeological area, which extends for about 6 km in the upper Awash Valley, at about 50 kilometres south of Addis Ababa, Ethiopia (Oromia Region, 8°41′0″N - 37°38′0″E), and at an altitude higher than 2,000 m above sea level (fig. 3.4.1). As a result of excavations carried out between 1970 and 1985 under the direction of Jean Chavaillon (Chavaillon and Berthelet, 2004), two distinct stratigraphic horizons have been recognized, with dating bracketed between 875 ± 10 and 709 ± 13 ka (Morgan, et al., 2012). The oldest date was found in localities 1, 3-5, over a volcanic layer called "Tuff B". The more recent date was found only in the locality 2, which is also known as the "butchery site".

The abundant stone tools referred to the Acheulean are mainly made of volcanic raw materials (Gallotti, et al., 2010, Saban, 1995). These include bifaces, cleavers, flakes and some choppers. Typical are the so-called "twisted handaxes" (Gallotti, et al., 2010) which are made of obsidian. These bifacial tools are of particular interest because they are almost unknown elsewhere in East Africa (Chavaillon, 1979) and show affinities with Lower Palaeolithic assemblages from England (White, 1998). Gombore II looks quite poor from a palynological perspective, but for the occurrence of Gramineae (Bonnefille, 1972). In contrast, the faunal fossil record is rich and includes: *Hippopotamus cf. amphibius*, *Diceros bicornis*, *Stylohipparion*, *Hypparion sp.*, *Equus cf. mauritanicum*, *Pelorovis oldowayensis*, *Connochaetes cf. taurinus*, *Damaliscus niro*, *Kobus cf. kob*, *Gazella sp.*, *Metridiochoerus compactus*, *Giraffa cf. jumae*, *Tachyoryctes konjiti*, *Hyaena hyaena*, *Canis sp.* and *Tadorna sp.* (Gallotti, et al., 2010, Geraads, 1979, Geraads, 1985).

The current chronology of more than 70 archaeological layers identified thus far in the Melka Kunture area was based on 40Ar/39Ar dating (Morgan, et al., 2012). Among the layers analysed at Gombore II (fig. 3.4.1), the unit 9959 is of particular interest because immediately below the Acheulean level (unit 9958) where the human remains were found. It is composed of a fine-grained white volcanic ash that gave a 40Ar/39Ar date of 875 ± 10 ka, while samples taken from the top of the sequence at locality 2 have provided a date of 709 ± 13 ka. The stratigraphic position of the human remains from Gombore II fits the chronological range interposed between these two dates, but it is

closer to the older one, suggesting a tentative chronology for the human fossils somewhat younger than 875 ka.

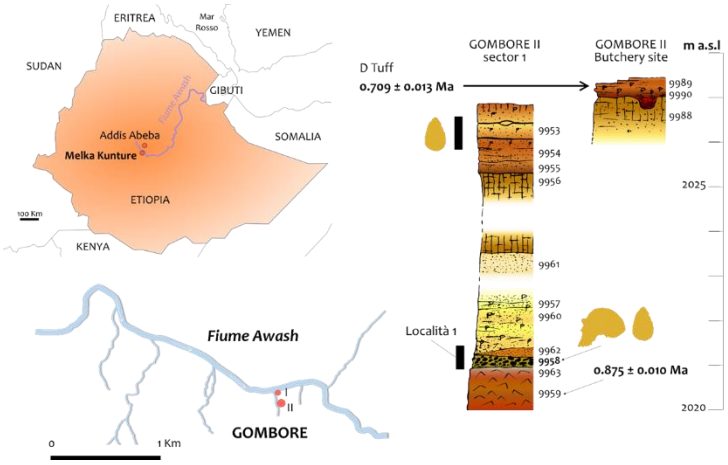

Figure 3.4.1: Geographical location of the Gombore sites I and II within the Melka Kunture area, south of Addis Ababa, Ethiopia. On the right, the stratigraphic section of Gombore II (modified from Raynal et al., 2004), with 40Ar/39Ar ages from Morgan and colleagues (2012). The archaeological levels (Acheulean) and the position of the human fossil specimens (cranial pieces) are indicated. Numbers from 9953 to 9990 refer to the stratigraphic units described by Raynal and colleagues (2004).

Paleomagnetic data support this interpretation (Tamrat, et al., 2014). The normal polarity (Brunhes) of the higher layers of Gombore II changes soon along the stratigraphic column, pointing to dates prior the Matuyama/Brunhes reversal, thus earlier than 780 ka, for the underlying levels including unit 9958. In conclusion, a reasonable chronology for the stratigraphic position of the human remains should be considered as bracketed between 780 and 875 ka, closer to the latter limit, thus ranging around 850 ka.

In 1973, during excavations in the Acheulean levels of locality 1, Claude Brahimi unearthed a partial left parietal, labelled MK73/GOM II - 6769 and formally referred to as Melka Kunture 1 (Oakley, et al., 1975), hereafter MK1. When discovered the find appeared strongly mineralized and encrusted with sandy material. It was classified as *Homo* cf. *erectus* (Chavaillon, et al., 1974, Chavaillon and Coppens, 1975, Chavaillon and Coppens, 1986) as it is also reported in the subsequent literature (e.g., Chavaillon and Berthelet, 2004, Coppens, 2004, Schwartz and Tattersall, 2005).

Two years later (1975), Rhorissa Delessa found a portion of human frontal bone just a few meters downstream of the area of excavation, in a narrow gorge that runs through the site with a seasonal stream (Chavaillon and Coppens, 1986). It was labelled MK76/GOM II - 576 (formally Melka Kunture 2, or MK2). Even according to the most recent interpretations (e.g., Chavaillon and Berthelet, 2004), it is likely that MK2 originated from the same layer where MK1 was previously found and was washed downstream by rain. The state of fossilization of the two finds, the patina and some morphological characteristics (the bone thickness in particular) provide evidence in support of this conclusion.

We directly examined the two original specimens at the National Museum of Ethiopia. These observations were integrated with the analysis of photographic documentation, high quality casts made by the Paleoanthropology Laboratory of the same museum, and CT digital data recorded in Addis Ababa.

MK1 is a left parietal (fig. 3.4.2), with missing areas of bone laterally and anteriorly. It appears massive, with considerable thickness varying from a maximum of 14.23 mm to a minimum of 5.85 mm. The sub-triangular apex facing the anatomical position of the temporal squama is bounded by fractures that represent the lateral margins of the specimen. These fractures exhibit sharp edges (fig. 3.4.2), whereas the more anterior border appears floated (fig. 3.4.2). Even the external and the endocranial surfaces are not eroded. Posteriorly, lambda is preserved, together with segments of the sagittal suture (for a length of about 71.5 mm) and the lambdoid suture (35 mm). Both sutures retain part of their indentations, whose incompleteness is probably due to synostosis, rather than to post-depositional damage. The synostosis is most evident on the endocranial margin of the posterior tract of the sagittal suture (obelic region), suggesting an age at death of the individual about 35-40 years, if compared to *Homo sapiens* (Meindl and Lovejoy, 1985).

Although the parietal is incomplete anteriorly, the anterior apex of the fragment would have been close to the coronal suture, as demonstrated by the reduction in thickness of the diploe and associated blending of the external and internal layers of compact bone visible along the fracture (see fig. 3.4.2). The length of the squama, measured parasagittally from this preserved portion close to the coronal suture to the corresponding margin along the lambdoidal suture, is 104.65 mm. In general, the diploe is strongly mineralized by infiltration, which confers a dark colour to it.

Figure 3.4.2: Exocranial and endocranial surfaces of the left parietal bone MK 1 (MK 73/GOM II 6769).The section of the anterior-lateral fracture (a) and of the preserved portion of the sagittal suture (b) are reported below, while in the box it is shown a detail of the floated margins along the anterior fracture. The colour version of this figure is available at the JASs website.

A short stretch of the temporal lines is visible on the external surface between the two major lateral fractures, in the area of greater convexity of the bone. The temporal lines run more medially and above the parietal eminence (i.e., the most prominent segment of the profile in coronal section). Posteriorly, in correspondence of the preserved portion of the sagittal suture (obelic region) the bone is visibly flattened, both longitudinally and parasagittally. The parietal foramen is absent (fig. 3.4.2).

The endocranial surface (fig. 3.4.2-3) includes impressions of the supero-lateral portions of the left parietal lobe, along with faint adjoining parts of the endocranial surface towards the postcentral gyrus (anteriorly) and the supramarginal gyrus (inferiorly). It is

possible to recognise the posterior portion of the superior sagittal sinus as well as convolutions of both the superior and inferior parietal lobule (fig. 3.4.3).

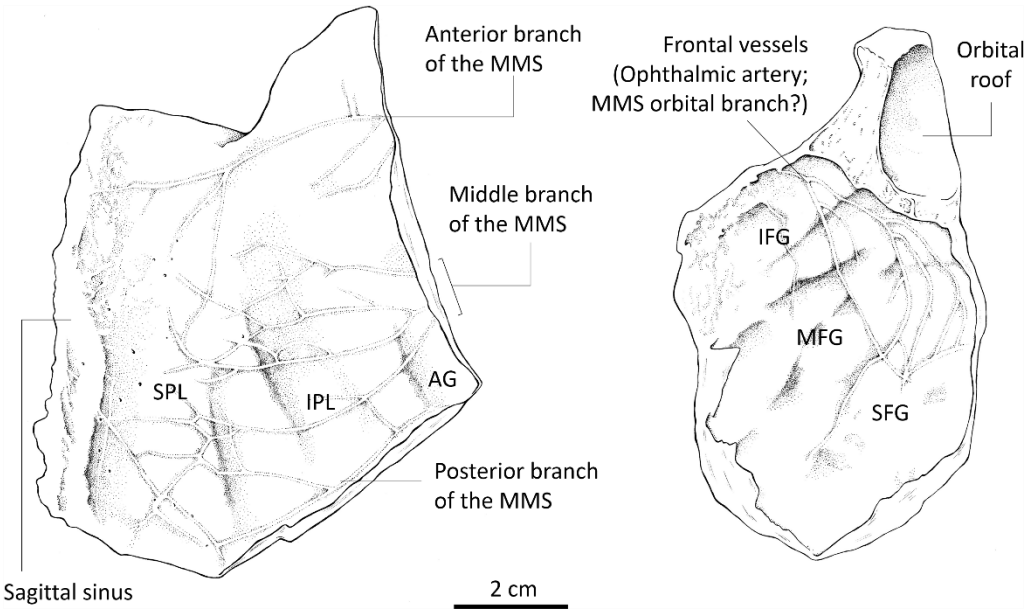

Figure 3.4.3: Representation of the endocranial surfaces of MK1 and MK2 showing the vascular patterns and the main cortical features. Legend: MMS = middle meningeal system; SPL = superior parietal lobule; IPL = inferior parietal lobule; AG = angular gyrus; IFG = inferior frontal gyrus; MFG = middle frontal gyrus; SFG = superior frontal gyrus.

The parietal lobe appears flat with a large depressed parasagittal area in correspondence of the superior parietal lobule. Also visible are impressions of the vascular middle meningeal system, represented by several deep branches almost reaching the sagittal edge of the bone. In particular, an anterior, rather isolated and deep groove is attributable to the bregmatic branch, while several anastomosing tracks related to the obelic branch occur more posteriorly. Only a brief impression of the lambdatic branch is visible, as the parietal angle is missing. The prevalence of the obelic or middle branch has to be remarked (fig. 3.4.3).

MK2 is a portion of the frontal bone (fig. 3.4.4), which preserves a large part of the right side of the squama and associated components of both the orbital roof and an incomplete frontal trigone, including the lateral wing of the torus and the zygomatic process with part of the zygomaticofrontal suture.

Figure 3.4.4: The partial frontal bone MK 2 (MK 73/GOM II 6769): exocranial and endocranial surfaces.

This specimen is massive, and considerably thick. A maximum thickness of 18.12 mm and a minimum of 6.87 mm were both measured on the squama, just behind the supraorbital region excluding the preserved part of the torus. The fracture close to the mid-sagittal plane has an irregular outline but a plain section, particularly in the more anterior portion (fig. 3.4.4), which appears rather fresh, i.e. not affected by taphonomic processes. The wide exposure of the internal structure of the bone shows that the diploe prevails over the inner and outer tables of compact bone. By contrast, the posterior fracture (toward the coronal margin of the bone) is affected by deep chipping of the outer surface, with oblique exposure of the underlying trabecular tissue. The coronal suture is not preserved, nor is most of the supraorbital torus (medial component of the trigone and the entire supraciliar arch (Cunningham, 1909) and the glabellar region. The frontal sinuses are missing.

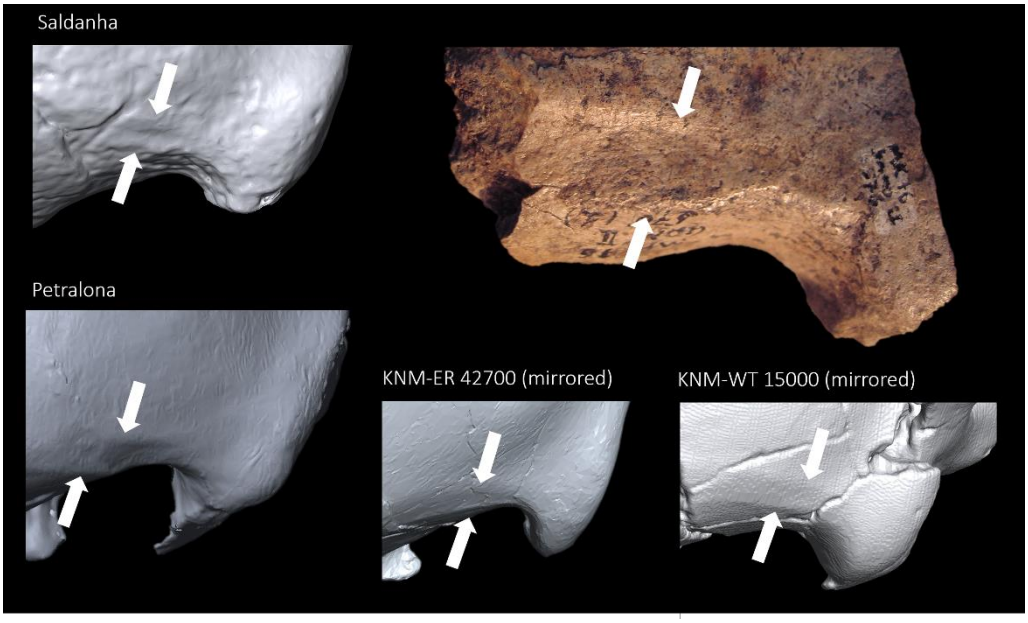

Figure 3.4.5: Detail of the temporal lines on MK2, diverging in the superior and inferior components since the frontal bone (arrows). This character is uncommon in both archaic and modern humans; digital comparisons (not at the same scale) are reported: Saldanha (top-left), Petralona (bottom-left), KNM-ER 42700 (bottom-centre), KNM-WT 15000 (bottom-right).

The supraorbital torus, judging by the size of the preserved portion (with a minimum thickness of 11.22 mm, measured in correspondence of the fracture involving the roof of the orbit), appears massive and laterally expanded. The post-orbital constriction appears marked and the supratoral sulcus shallow; with respect to it, the scale rises with modest inclination, while the external profile of the bone is gently and uniformly convex. Laterally, on the external surface, the temporal lines are clearly visible and characterized by a deep sub-triangular gap (fig. 3.4.5). The two lines, in fact, double soon in an inferior line, which originates from the posterior margin of the zygomatic process and continues nearly horizontal, and a clearly distinguished superior line, which diverges upward until a maximum separation (as far as the squama is preserved) of about 12.5 mm.

The endocranial surface (fig. 3.4.3) includes impressions of the anterior and medial portions of the right frontal lobe. It does not exhibit clear traces of the sagittal sinus and/or the frontal crest (given that the corresponding region of the bone is not preserved anteriorly), making difficult the secure identification of the sagittal plane. The superior and middle frontal gyri are well discerned, while only the more rostral portion of the inferior frontal gyrus is preserved (fig. 3.4.3); the frontal bec and the orbital portion are missing. Vascular impressions are also visible: in particular, there are five small branches transversally oriented, which we consider as vessels of the ophthalmic artery with the possible contribution of the orbital branch of the middle meningeal system (Saban, 1995). The position of the encephalic volumes appears posterior to the roof of the orbits.

3.4.2 The comparative samples

In the table 3.4.1, a complete list of comparative samples used in the various analyses performed in this paper is reported. The analyses involved features of both the parietal and the frontal bone, with reference to various extinct species or operational taxonomic units (OTUs) of the genus *Homo* – *Homo ergaster* (ERG), *Homo erectus* (ERE), *Homo heidelbergensis* (see below) and *Homo neanderthalensis* (NEA) – as well as to recent samples of *Homo sapiens* (SAP). We differentiated the representatives of *Homo heidelbergensis* in macro-regional OTUs – African (HAF), Asian (HAS) and European (HEU) – and, when possible, we made also a distinction between two evolutionary "grades" among the African specimens of the Middle Pleistocene, respectively referred to as HA1 and HA2 according to their chronology and morphology.

There is one (at least) controversial issue in this respect, regarding the attribution of specimens from Atapuerca Sima de los Huesos to Homo heidelbergensis, given that this impressive sample (e.g., (Arsuaga, et al., 2014, Arsuaga, et al., 2015)) shows to belong to the Neanderthal lineage more clearly than other European fossils of the same age (e.g., (Stringer, 2012)). Nevertheless, following previous analyses (Mounier, et al., 2011, Mounier, et al., 2009) and reviews of the available fossil and molecular evidence (e.g., (Bastir, et al., 2011)), we claim for a less speciose interpretation of the variability exhibited by African and Eurasian hominins of the Middle Pleistocene and support their common allocation within a single taxon, despite the apparent divergence in regional demes (or subspecies) that increases over time.

Table 3.4.1: Specimens sampled and sources of metric data.

* The parietal arc and chord values were acquired on original specimen, cast or 3D model, when not available in the literature:a: Kaifu et al., 2008; b: Santa Luca, 1980; c: Ascenzi et al., 2000; d: Rightmire et al., 2006; e: Lordkipanidze et al.,2006; f: Rightmire, 2013; g: Rightmire, 2008; h: Haile-Selassie et al., 2004; i: Asfaw et al., 2008.

** Specimen sampled for GMM analysis of the midsagittal curvature between lambda and bregma.R/L Right and/or Left side of the specimen that was sampled for GMM analysis of the inferior temporal line along thefrontal bone.

SPECIMEN	SPECIES	OTU	PARIETAL			FRONTAL (INF. TEMPORAL LINE)
			ARC	CHORD	GMM	GMM
Melka Kunture 1		MK1a	*	*	-	-
		MK1b	*	*	-	-
		MK1c	*	*	-	-
		MK1d	*	*	-	-
Melka Kunture 2		MK2a	-	-	-	R
		MK2b	-	-	-	R

SPECIMEN	SPECIES	OTU	PARIETAL			FRONTAL (INF. TEMPORAL LINE)
			ARC	CHORD	GMM	GMM
Bukuran	*Homo erectus*	ERE	a	a	-	-
Ngandong 1	*Homo erectus*	ERE	b	b	-	-
Ngandong 10	*Homo erectus*	ERE	b	b	-	-
Ngandong 11	*Homo erectus*	ERE	b	b	-	-
Ngandong 12	*Homo erectus*	ERE	b	b	**	R/L
Ngandong 3	*Homo erectus*	ERE	b	b	-	-
Ngandong 5	*Homo erectus*	ERE	b	b	-	-
Ngandong 6	*Homo erectus*	ERE	b	b	-	-
Ngandong 7	*Homo erectus*	ERE	b	b	**	R
Ngandong 9	*Homo erectus*	ERE	b	b	-	-
Sambungmacan 1	*Homo erectus*	ERE	a	a	-	-
Sambungmacan 3	*Homo erectus*	ERE	a	a	**	R/L
Sambungmacan 4	*Homo erectus*	ERE	a	a	-	-
Sangiran 10	*Homo erectus*	ERE	a	a	-	-
Sangiran 12	*Homo erectus*	ERE	a	a	-	-
Sangiran 17	*Homo erectus*	ERE	b	b	-	-
Sangiran 2	*Homo erectus*	ERE	c	c	**	L
Sangiran 38	*Homo erectus*	ERE	a	a	-	-
Sangiran IX (Tjg-1993.05)	*Homo erectus*	ERE	f	-	-	-
Zhoukoudian II	*Homo erectus*	ERE	-	-	**	-
Zhoukoudian III	*Homo erectus*	ERE	-	-	**	R/L
Zhoukoudian X	*Homo erectus*	ERE	c	c	**	-
Zhoukoudian XI	*Homo erectus*	ERE	c	c	**	R/L
Zhoukoudian XII	*Homo erectus*	ERE	c	c	**	-
Buia (UA 31)	*Homo ergaster*	ERG	*	*	-	-
D2280	*Homo ergaster*	ERG	d	d	**	R/L
D2282	*Homo ergaster*	ERG	d	d	**	L
D2700	*Homo ergaster*	ERG	d	d	-	-
D3444	*Homo ergaster*	ERG	e	e	-	-
Daka (BOU-VP-2/66)	*Homo ergaster*	ERG	i	i	-	-
KNM-ER 42700	*Homo ergaster*	ERG	f	-	-	-
KNM-ER-3733	*Homo ergaster*	ERG	c	c	**	L
KNM-ER-3883	*Homo ergaster*	ERG	c	c	**	-
KNM-WT 15000	*Homo ergaster*	ERG	d	d	-	L
OH9	*Homo ergaster*	ERG	-	-	-	L
Olorgesailie	*Homo ergaster*	ERG	-	-	-	R
Kabwe 1	*Homo heidelbergensis*	HA1	b	b	**	R/L
Bodo	*Homo heidelbergensis*	HA1	-	-	-	L

SPECIMEN	SPECIES	OTU	PARIETAL			FRONTAL (INF. TEMPORAL LINE)
			ARC	CHORD	GMM	GMM
Dali	*Homo heidelbergensis*	HAS	-	-	-	R/L
Zuttiyeh	*Homo heidelbergensis*	HAS	-	-	-	R/L
Saldanha	*Homo heidelbergensis*	HA1	g	g	**	L
Eliye Springs (KNM-ES 11693)	*Homo heidelbergensis*	HA2	h	h	**	-
Narmada	*Homo heidelbergensis*	HAS	-	-	-	R
Irhoud 1	*Homo heidelbergensis*	HA2	h	h	**	R/L
Ngaloba (LH 18)	*Homo heidelbergensis*	HA2	h	h	**	-
Omo Kibish 2	*Homo heidelbergensis*	HA2	g	g	**	R/L
Arago XXI/XLVII	*Homo heidelbergensis*	HEU	g	g	-	R/L
Ceprano	*Homo heidelbergensis*	HEU	*	*	-	L
Petralona	*Homo heidelbergensis*	HEU	g	g	**	R/L
Atapuerca Sima de los Huésos 4	*Homo heidelbergensis*	HEU	g	g	**	R/L
Atapuerca Sima de los Huésos 5	*Homo heidelbergensis*	HEU	g	g	**	-
Stenheim	*Homo heidelbergensis*	HEU	*	*	**	R
Swascombe	*Homo heidelbergensis*	HEU	*	*	**	-
Amud	*Homo neanderthalensis*	NEA	*	*	**	R/L
Gibraltar 1	*Homo neanderthalensis*	NEA	-	-	-	R
Guattari 1	*Homo neanderthalensis*	NEA	*	*	**	L
La Chapelle-aux-Saints	*Homo neanderthalensis*	NEA	b	b	**	R/L
La Ferrassie 1	*Homo neanderthalensis*	NEA	b	b	**	L
Neanderthal 1 (Feldhofer)	*Homo neanderthalensis*	NEA	-	-	-	L
La Quina 5	*Homo neanderthalensis*	NEA	b	b	-	R/L
Shanidar 1	*Homo neanderthalensis*	NEA	-	-	-	R
Saccopastore 1	*Homo neanderthalensis*	NEA	*	*	**	-
Spy1	*Homo neanderthalensis*	NEA	b	b	**	R

SPECIMEN	SPECIES	OTU	PARIETAL			FRONTAL (INF. TEMPORAL LINE)
			ARC	CHORD	GMM	GMM
Spy2	*Homo neanderthalensis*	NEA	b	b	**	R/L
Tabun C1	*Homo neanderthalensis*	NEA	b	b	-	R/L
CSIC-OL 1068	*Homo sapiens*	SAP	*	*	**	-
CSIC-OL 794	*Homo sapiens*	SAP	*	*	**	-
CSIC-OL 866	*Homo sapiens*	SAP	*	*	**	-
CSIC-OL 886	*Homo sapiens*	SAP	*	*	**	-
CSIC-OL1112	*Homo sapiens*	SAP	*	*	**	-
CSIC-OL1187	*Homo sapiens*	SAP	*	*	**	-
CSIC-OL1192	*Homo sapiens*	SAP	*	*	**	-
CSIC-OL1193	*Homo sapiens*	SAP	*	*	**	-
CSIC-OL1197	*Homo sapiens*	SAP	*	*	**	-
CSIC-OL1199	*Homo sapiens*	SAP	*	*	**	-
CSIC-OL1282	*Homo sapiens*	SAP	*	*	**	-
CSIC-OL1428	*Homo sapiens*	SAP	*	*	**	-
VA-003-CR	*Homo sapiens*	SAP	*	*	**	-
VA-004-CR	*Homo sapiens*	SAP	*	*	**	-
VA-005-CR	*Homo sapiens*	SAP	*	*	**	-
VA-006-CR	*Homo sapiens*	SAP	*	*	**	-
VA-010-CR	*Homo sapiens*	SAP	*	*	**	-
VA-011-CR	*Homo sapiens*	SAP	*	*	**	-
VA-012-CR	*Homo sapiens*	SAP	*	*	**	-
VA-013-CR	*Homo sapiens*	SAP	*	*	**	-
VA-014-CR	*Homo sapiens*	SAP	*	*	**	-
VA-016-CR	*Homo sapiens*	SAP	*	*	**	-
VA-017-CR	*Homo sapiens*	SAP	*	*	**	-
VA-020-CR	*Homo sapiens*	SAP	*	*	**	-
VA-021-CR	*Homo sapiens*	SAP	*	*	**	-
VA-022-CR	*Homo sapiens*	SAP	*	*	**	-
VA-023-CR	*Homo sapiens*	SAP	*	*	**	-
VA-024-CR	*Homo sapiens*	SAP	*	*	**	-
VA-026-CR	*Homo sapiens*	SAP	*	*	**	-
VA-027-CR	*Homo sapiens*	SAP	*	*	**	-
VA-029-CR	*Homo sapiens*	SAP	*	*	**	-
VA-030-CR	*Homo sapiens*	SAP	*	*	**	-
VA-031-CR	*Homo sapiens*	SAP	*	*	**	-
VA-032-CR	*Homo sapiens*	SAP	*	*	**	-

3.4.3 Parietal: mid-sagittal curvature (traditional morphometrics)

Since MK1 lacks the anterior part of the sagittal suture, four values of its parietal arc and chord were estimated. For this purpose, data referring to arc and chord lengths in different samples were used to explore size and shape of the biparietal profile along the mid-sagittal plane.

As reported in Figure 6A, the arc length in MK1 was considered intermediate between the variability of *Homo ergaster* (mean = 96.29 mm; s.d. = 8.89 mm) and that of African *Homo heidelbergensis* (mean = 123.17 mm; s.d. = 7.20 mm). This suggested that the more probable estimate lies between 96 mm and 123 mm. Then, we chose four different simulations with respect to a selection of pertinent African samples, that is the following mean values: 96.0 mm (ERG; MK1a), 103.0 mm (intermediate arc length between Buia and Daka; MK1b), 121.0 mm (HA1 subsample; MK1c), and 123.0 mm (HAF; MK1d). The estimated figures of MK1 were then compared to those of 88 specimens of different species/OTUs of *Homo*. Comparative data (see table 3.4.1) where obtained either from digital models or from first-quality casts, integrated with data available in the literature; on digital models (both CT and laser scan), measurements were acquired through the function "SurfacePathSet" of Amira 5.4.5, using a plane-cut connector set on "mesh triangles". On these bases, the chord value gave a measurement of size (fig. 3.4.6A), while the parietal index (chord/arc length; fig. 3.4.6B) furnished the mean curvature of the parietal bone along the midsagittal profile.

As shown in fig. 3.4.6B, *Homo neanderthalensis* and *Homo sapiens* are quite different from all the other OTUs, with the exception (at least in part) of the OTUs of *Homo heidelbergensis* (HA1 and HA2), whereas *Homo erectus* and *Homo ergaster* show lower degrees of curvature. The parietal indexes for MK1a and MK1b (estimated on *Homo ergaster*) are higher than means observed for all the other OTUs, entailing a low mean curvature value of the parietal bone along the mid-sagittal plane. In contrast, the two simulations performed on African *Homo heidelbergensis* (MK1c and MK1d) exhibit a parietal curvature intermediate between the means of ERG and HA1.

3.4.4 Parietal: mid-sagittal profile (geometric morphometrics)

In order to capture other components of the shape variation, as far as the mid-sagittal biparietal arc is concerned, a PCA on 49 evenly-spaced landmarks was performed (fig. 3.4.6C) on a sample of 65 specimens belonging to *Homo ergaster*, *Homo erectus*, *Homo heidelbergensis*, *Homo neanderthalensis* and *Homo sapiens* (see table 3.4.1). The 49 landmarks where defined as evenly-spaced points, after applying a Bézier curve (Olsen, 2015) on the original point set acquired for each specimen (Profico and Veneziano, 2015); the defined curve starts from bregma and ends to lambda. The data set was acquired either using the function "SurfacePathSet" of Amira 5.4.5 on high-resolution digital model, or a Microscribe (model G2X; time auto plot = 10 ms).

As for MK1, we calculated how many points would be missing (mp) in the four different simulations of the MK1 arc length described above, that is respectively close to mean values of the following African samples: ERG (MK1a: mp = 13), Buia and Daka (MK1b; mp = 15), HA1 subsample (MK1c: mp = 20) and HAF (MK1d; mp = 21). The missing points (Arbour & Brown, 2014) were estimated using a subsample belonging to HAF, HEU, and ERG, through the function "fixLMtps" of the "R" Morpho package (Schlager, 2013). The resultant 49 landmarks were used to calculate by an iterative process (i = 3) the intermediate points (N = 385), using the function "dec.curve" of the "R" Arothron package (Profico and Veneziano, 2015). The new matrix of points were used to define the final four evenly-spaced landmark sets for MK1.

The 3D landmark set of each specimen was aligned placing the origin on the bregma and the z axis along the mid-sagittal plane; the 3D data set was then projected in 2D, in order to remove any positional noise along the mid-sagittal plane, and a PCA (PCA) was finally performed on the Procrustes coordinates (69 configurations).

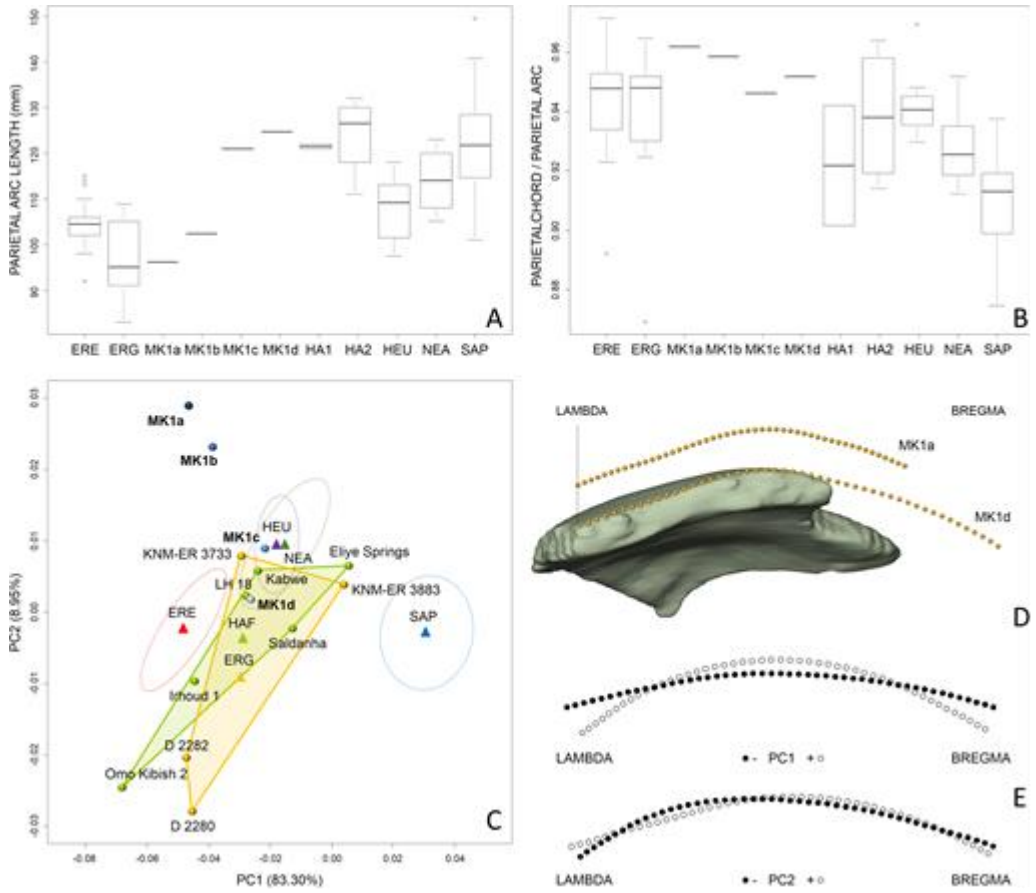

Figure 3.4.6: (A) Parietal arc length and (B) parietal curvature index in the OTUs reported in the Appendix; four different estimations for MK1 are shown: MK1a, MK1b, MK1c and MK1d (see text for details). C) PCA analysis (PC1 vs PC2) of landmark data taken on the mid-sagittal profile according to the configuration of landmarks "a" and "d" showed on the digital model of MK1 (D). E) Shape variations of the biparietal profile (from lambda to bregma) at the extremes of PC1 and PC2.

The first two PCs explains cumulatively more than 90% of the total variance (fig. 3.4.6C). In this framework, as expected, the cluster of *Homo sapiens* (SAP) is clearly separated by the remaining OTUs, occupying a morpho space defined for positive values of PC1 and neutral of PC2; by contrast, other groups show negative values for PC1, in particular ERE, ERG and HAF. As for the MK1 simulations, all of them have high values for PC2, while for PC1 both MK1a and MK1b display more negative values than those of MK1c, and MK1d.

The first principal component (PC1) mainly detects parietal curvature (fig. 3.4.6E), recording the mean curvature of the parietal arc, as highlighted by the linear regression with the parietal index (R^2=0.96, p-value=<0.001) whose values are reported in Figure 6B. PC2 deals with the flattening along the obelic trait of the biparietal profile (Fig. 6E, positive values of PC2). MK1c and MK1d are near the mean values of ERG and HAF variability along the PC1, while on PC2 they are close to African specimens of different taxonomy, being characterized by strong obelic flattening (such as Kabwe 1). We assume

therefore that these two estimates corresponds more closely to the real morphology of the complete parietal from Gombore II, in agreement also with the result obtained exploring size and shape of the biparietal arc by traditional morphometrics. At the same time, the configurations MK1a and MK1b fall outside the more relevant fields of variability.

3.4.5 Frontal: inferior temporal line (shape analysis)

On the frontal (MK2), the inferior temporal line is preserved from the fronto-temporo-malar (or fmt; i.e. the most external point of the zygomaticofrontal suture), but it does not reach stephanion (or st; i.e. the point where the inferior temporal line crosses the coronal suture). The contour of the inferior temporal line was analysed using a set of 25 3D evenly-spaced landmarks, estimating the stephanion in MK2 with a procedure similar to that used for the parietal arc. When possible, both right and left inferior temporal lines of the various specimens were sampled, mirroring the latter sub-sample before performing the analysis. Then, the Procrustes registration (function `procSym` of Morpho "R" package; Schlager, 2014) was performed. In MK2 the position of the st and the missing trait of the inferior temporal line were estimated two times (MK2a and MK2b), according to the mean length of two different species respectively: *Homo ergaster* and *Homo heidelbergensis*. In addition to MK2a and MK2b, the comparative sample consists of 54 fossil specimens belonging to *Homo ergaster*, *Homo erectus*, *Homo heidelbergensis* (including the OTUs HA1 and HA2) and *Homo neanderthalensis* (see table 3.4.1). Lengths of the inferior temporal line were measured through the function `Bèzier ArcLength` of the Bèzier "R" package (Olsen, 2015).

In the PCA of the Procrustes coordinates, the first principal component explains 64.57% of the total variance; it has been plotted against the length of the inferior temporal lines (fig. 3.4.7). Homo ergaster is characterized in mean by a long temporal line despite the lower cranial size of this OTU with respect to the others (Holloway, et al., 2004); MK2a falls at the extreme of the variability of this species (ERG), whereas MK2b is close to that of HA1 (early African Homo heidelbergensis). It has to be underlined that, although the length of MK2a and MK2b configurations were respectively estimated on the ERG and HA1 median length, the missing landmarks were obtained independently from these length simulations.

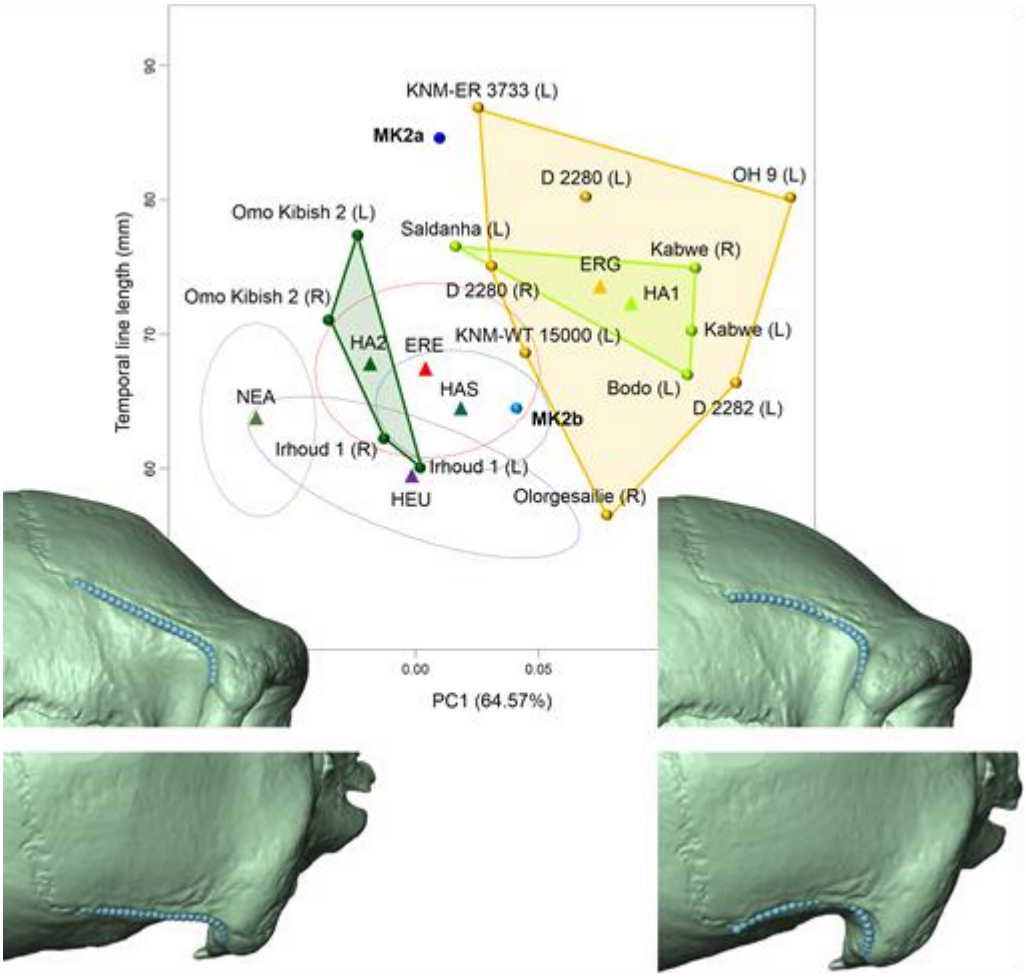

Figure 3.4.7: Bivariate plot comparing the variation in shape of the temporal line across the frontal bone (only PC1) and its total length in fossil human samples (OTUs and specimens as in table 3.4.1); the estimated extended profiles of MK2 (see text for details) are respectively referred to as MK2a and MK2b. Consistent shape changes are showed on Kabwe 1 at the extreme poles of the PC1 extension. Legend as in the Appendix; L = left side; R = right side.

Looking at the PC1 values only, MK2a falls near the centroid of *Homo erectus*, while MK2b is internal to the variability of both HA1 and ERG. This means that, as shown by the warpings of the line consistent to shape changes in the frontal region of a reference specimen (fig. 3.4.7), either MK2a or MK2b exhibit moderate postorbital constriction.

3.4.6 The digital alignment of the MK cranium

Given the affinities with African representatives of early Homo heidelbergensis (HA1) and particularly, as emerged from our results, with Kabwe 1, the MK cranial fragments were digitally placed on this specimen (see fig. 3.4.8), in order to have an idea of their anatomical placement and emphasize the observed patterns of curvature and thickness (fig. 3.4.8). The digital alignment (see subchapter 2.3.3) was performed using a landmark-based approach after scaling the landmark sets and the digital model belonging to Kabwe, using the parietal arc as scale factor (0.96). Following the same procedure, a restored virtual endocast of Kabwe was the guideline to estimate a probable cranial capacity of the MK cranium, which resulted to be around 1.080 cm3.

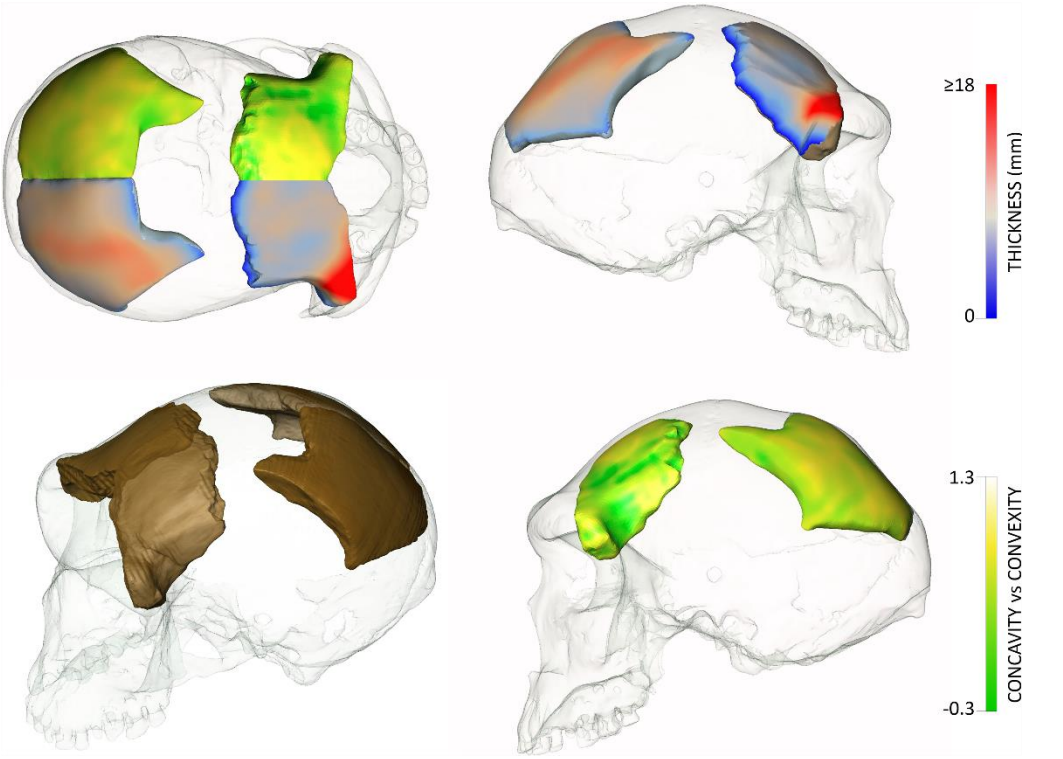

Figure 3.4.8: Virtual reconstruction of the MK cranium from Gombore II (MK1 + MK2), using a scaled version (0.96) of Kabwe 1. MK1 (left parietal) and MK2 (right frontal) are doubled by mirroring; colours representing the variation in hickness as well as the degree of curvature are reported (scales on the right); a more pictorial oblique view is also shown bottom-left).

3.4.7 MK cranium and the origin of *Homo heidelbergensis*

An increasing body of data suggests that bipedal hominids engaged in the first out-of-Africa diffusion were not derived, encephalised and technologically advanced humans, but definitively more archaic creatures, with a brain just above 500 ml and a morphology close to that of the so-called "early Homo" (e.g., Antón, 2012, Rightmire, et al., 2006). The same corpus of data suggests that their dispersal started well before the appearance of the Acheulean, thus earlier than 1.6 Ma (see references in Manzi (2012)). Now we understand that – driven by ecological, rather than by behavioural or "cultural" motives – these earliest representatives of the genus *Homo* had the tendency to diffuse and adapt to variable non-tropical environments and that these dispersals were followed by geographical isolation. Under this approach, *Homo erectus* should be viewed as a species of the Far East, distributed in the island of Java and in Northern China, whereas its African counterparts may be regarded as a distinct species (contra Asfaw, et al. (2002)), referred to as *Homo ergaster*, recognisable in the fossil record until about 1,0 Ma on the basis of specimens such as Daka, Buia and Olorgesailie (e.g., Manzi, et al., 2003, Manzi, 2004). At the same time, these crania of the late Early Pleistocene are distinct from those of the Middle Pleistocene that may be referred to *Homo heidelbergensis*, either in Africa (specimens like Bodo and Kabwe 1) in Europe (including the sample from Atapuerca SH, Petralona or Ceprano) or in mainland Asia (Narmada, Dali, Jinniushan).

These observations suggest a taxonomic and phylogenetic discontinuity that ranges across the Matuyama/Brunhes reversal of 780 ka, in possible relationship with the more general phenomenon known as the "Mid-Pleistocene revolution" (Maslin and Ridgwell, 2005) that, in turn, corresponds to the beginning of environmental changes related to the long and dramatic climatic breakdown of MIS 18-16. The phenetic distance between humans of the Early and the Middle Pleistocene in sub-Saharan Africa signals a crucial passage in the evolution of the genus *Homo* and probably represents a distinction at the species level. Although the period bracketed between approximately 900 and 600 ka is very poor of fossil evidence, it seems therefore that something crucial happened at that time, generating a new and more encephalised kind of humanity that spread quite rapidly in Africa and Eurasia. When viewed as a geographically widespread single taxon from which both Neanderthals and modern humans originated (e.g., Mounier, et al., 2011, Mounier, et al., 2009, Rightmire, 1998, Rightmire, 2008, Stringer, 2012), these humans of the Middle Pleistocene should be referred to as *Homo heidelbergensis* (Schoetensack, 1908), despite the scientific community still miss to find an agreement on this point (e.g., Arsuaga, et al., 2014, Arsuaga, et al., 2015, Balter, 2014).

Nevertheless, at present, the chronology, topology and phylogenetic dynamics related to the rather synchronous appearance of Middle Pleistocene humans that we may refer to *Homo heidelbergensis* are still unclear. As a matter of fact, we do not know when and from where the humans that were ancestral to both the Neanderthals in Europe and *Homo sapiens* in Africa originated (Rightmire, 1998, Rightmire, 2008). A possible answer about the time of emergence of this last common ancestor comes from the complete mtDNA

extracted from the phalanx of the Denisova cave in the Altai mountains, dated to 48-30 ka, which demonstrates the existence of humans that were different from both *Homo neanderthalensis* and *Homo sapiens*, but shared with them a common ancestor between 1.3 Ma and 779 ka (Desbrun, et al., 1999, Krause, et al., 2010, Meyer, et al., 2012).

As a working hypothesis, this suggests that the Denisova phalanx may represent a still unknown hominin that originated, together with the ancestor/s of Neanderthals and modern humans, before the beginning of the Middle Pleistocene and thus, interestingly, just before the appearance of *Homo heidelbergensis* in the fossil record. This scenario is integrated by inferences obtained when Neanderthals and modern humans are compared genetically. Their coalescence around 500 ka (Endicott, et al., 2010, Green, et al., 2008) is consistent with a more ancient common ancestor, as well as with the subsequent morphological divergence occurring between the European and African lineages during the Middle Pleistocene (as a number of studies demonstrated after Santa Luca, 1978 (Santa Luca, 1978)).

Indeed, looking at the hypodigm of *Homo heidelbergensis* as a whole, it is clear that a considerable amount of variability characterises this species (Mounier, et al., 2011, Mounier, et al., 2009), since populations of Africa, Asia and Europe respectively bore peculiar regional features, promoting distinctions at the sub-specific level (as suggested by Manzi (2012)). Moreover, there is considerable phenotypic variation even within the same macro-region, at least across time. The variability of the European fossil record of the Middle Pleistocene, in particular, has been greatly expanded by the revised chronology of the calvarium from Ceprano in Italy (Nomade, et al., 2011), a specimen that could document «the occurrence of an ancestral stock of Homo heidelbergensis/rhodesiensis» (Bruner, 2007), since it represents a mosaic morphological bridge between *Homo erectus* sensu lato, on one hand, and *Homo heidelbergensis*, on the other (Mounier, et al., 2011). Thus, despite its relatively recent age, the Italian specimen may represent the morphology of the yet undiscovered ancestral stock of *Homo heidelbergensis*, preserved in an isolated area of Southern Europe, while in other areas of the continent there the combination of derived features that characterise the so-called "Neanderthal lineage" was already appearing (e.g., (Arsuaga, et al., 2014))

Nevertheless, the best candidate for this crucial phylogenetic position should be more ancient than Ceprano and should not be in Europe. In this perspective, the fragmentary cranial remains from Gombore II (Melka Kunture, Ethiopia), respectively referred here to as MK1 (an incomplete left parietal) and MK2 (a right large frontal fragment), are in a privileged position in terms of both chronology (about 850 ka) and topology (sub-Saharan Eastern Africa). Our analysis supports the hypothesis that these distinct portions, probably belonging to the same heavy cranium (Fig. 8), demonstrate a morphology that is sufficiently distinct from *Homo ergaster*, despite the overlap of some features, and close to early representatives of African *Homo heidelbergensis*, particularly Kabwe 1 (or Broken Hill 1).

In sum, we underline that the morphology of the MK specimens fills the phenetic gap observed between *Homo ergaster* and *Homo heidelbergensis*. In view of the chronology of the

human cranial bones from Gombore II, this conclusion appears of extreme interest, suggesting that such a partial cranium represents at present the best, if not the unique candidate for the ancestral occurrence of *Homo heidelbergensis* around 800 ka, as well as an evidence that this species probably originated in Africa before its dispersal in Eurasia.

3.5 Cranial base morphology in fossil and extant Hominoids: foramen magnum positioning, allometry and phylogeny.

3.5.1 Introduction

The study of the cranial base district plays a central role in the understanding of phenomena characterizing the evolution of the genus *Homo* (Dean and Wood, 1984; Kimbel and Rak, 2010; Kimbel et al., 2014; Lieberman et al., 2000a; Lieberman et al., 2000b). Following the discovery of Taung's child (Dart, 1925), the cranial base morphology and the relative foramen magnum position were recognized as key factors in the evolution of bipedalism (Ahern, 2005, Ashton and Zuckerman, 1956, Biegert, 1963, Luboga and Wood, 1990).

The development of the planum occipitale is driven by four nuclei of ossification: basioccipital, sopraoccipital and paired exoccipitals. On the contrary, the ossification of the planum nuchale is intramembranous (Shapiro and Robinson, 1976).

Various methods have been proposed to measure the relative position of the foramen magnum (Luboga and Wood, 1990) including the "head-balancing index", which expresses the basion-inion distance as a percentage of the basion-prosthion length (Dart, 1925). The method commonly used is to project the anatomical points (e.g. basion, opisthion, opistocranion, prosthion) on the Frankfurt plane and to measure the horizontal distance between them (Howells, 1968, Luboga and Wood, 1990, Russo and Kirk, 2013). A third method to infer the position of the foramen magnum is that proposed by Ahern (2005), which consists in acquiring the horizontal distances, on the Frankfurt plane, from the basion to the bicarotid line.

In Hominini, the foramen magnum is positioned more anteriorly (rostral) and these evolutionary changes have been ascribed to bipedal locomotion.

This functional adaptation is more evident within genus *Homo* than *Australopithecus*. So, the index of foramen magnum position (Dart, 1925, Luboga and Wood, 1990, Russo and Kirk, 2013, Weidenreich, 1941) is used to infer and predict the locomotor habits and postural pattern in living and extinct human species. The cranial base is attached to the post-cranium via the atlanto-occipital joint, which allows flexion and extension movements of the head and, to a lesser degree, of lateral bending; different muscles involved in the support and rotation of the head are also inserted in the occipital bone (Aiello and Dean, 1990).

In addition, evolution of the human cranium is characterized by a massive reduction in facial and alveolar prognathism (especially in *Australopithecus* and *Paranthropus* and early *Homo*) and an increase in encephalic volume (in the genus *Homo*).

The modularity is a biological phenomenon that occurs jointly to development and evolution of the skull in human (e.g., Bastir, et al., 2010, Esteve-Altava, et al., 2015,

Lieberman, 2011, Ross, 2013) as well as in non-human primates (e.g., Goswami and Polly, 2010, Mitteroecker and Bookstein, 2008). This approach can be performed through the analysis of the shape covariation using GM (Klingenberg, 2008, Singh, et al., 2012) defining minimum two cranial modules (e.g., face, vault, and basicranium).

Considering the functional importance of the cranial base district, recent studies have focused on its morphology through traditional approaches (Ahern, 2005, Ashton and Zuckerman, 1956, Biegert, 1963, Kimbel and Rak, 2010, Kimbel, et al., 2014, Luboga and Wood, 1990) and GM (Bastir and Rosas, 2009, Bastir, et al., 2010, Bastir, et al., 2011, Singh, et al., 2012).

The position (central) of the foramen magnum in humans is perpendicular to the upright position of the head, while that of the posteriorly located foramen magnum in apes is such that the head is in line with the quadrupedal body (Ahern, 2005).

There is a great variability within Hominoidea of locomotor habits, including the arboreal and terrestrial quadrupedism, suspension, brachiation and bipedalism. Within the genera *Pan*, *Gorilla* and *Pongo* is observed change of preferential habit locomotor in the different ontogenetic stages (Doran, 1992, Thorpe and Crompton, 2006); in addition, various studies have shown that the placement of the foramen magnum varied during the ontogeny in the great Apes (Ashton and Zuckerman, 1956, Luboga and Wood, 1990).

The development of different species can be represented as an ontogenetic sequence (ontogenetic trajectory). In GM the variable CS establishes the size of the landmark configuration and these values can be used to analyse the effect of the allometric component on the morphological evolution of the cranial base.

The morphology of the skull base in great Apes varies, during ontogeny, depending on the functional demands present in each individual ontogenetic stage, and it is plausible that the same changes that have taken place during growth in apes will reoccur according to the same patterns in the course of human evolution.

In this subchapter the cranial base morphology and its variability in the Hominoidea taxon was tested on three different working hypothesis:

- ✓ the common anatomical traits of the skull mainly determinate the morphology of the cranial base morphology; in this view this the morphology of this district is mainly influenced by phylogenetic relationship;
- ✓ the locomotor habits and the foramen magnum position (postural pattern) affect the cranial base shape;
- ✓ the size of the skull influences the cranial base shape; in this perspective the allometric variations in the Homonidea determinates the morphology of the cranial base district.

In the last years, it has established a paradigm of multifactorial natural of the hypotheses to explain the biological changes under adaptive and evolutionary phenomena. In this

perspective, it has enhanced the ability to test scientific hypotheses about the linkages between the causes and the effect of anatomical changes that have occurred.

A fourth working hypothesis is that the morphology of the cranial base is determined by a combination of allometric, phylogenetic and functional factors (multifactorial hypothesis).

The purpose of this study is to analyse, by applying methods of GM and multivariate analysis, the district of the skull base using a 3D landmark set to extrapolate the morphological pattern in different species. The sample consists of a 3D model of Hominoidea belonging to living and fossil species. In addition, in this study we calculated the central position of the foramen magnum along the mid-sagittal profile of the skull (oriented on the Frankfurt plane) in such a way as to allow the relationship between the morphology of the skull base and position of the foramen magnum to be quantified in an ontogenetic and evolutionary perspective. A phylogenetic test was performed on univariate and multivariate variables using an evolutionary tree. A multifactorial approach (variation partitioning) was used to assessed the contribution of allometric, phylogenetic and functional factors on the cranial base shape, estimating the "pure" and total effects of these component. The total effect of each factor is intended as the sum of the "pure" effect in addition to the variance explained in sharing to other factors (Raia, et al., 2010).

3.5.2 The comparative sample and the landmark configuration

The sample includes 189 crania that belong to fossil and living species of Hominoidea. The sample was divided into different age groups using a discrete variable based on the teeth eruption pattern.

In detail, the living species include *Pan troglodytes*, *Gorilla gorilla*, *Pongo pygmaeus*, and *Homo sapiens*, while those in the fossil group include specimens attributable to *Australopithecus africanus*, *Paranthropus boisei*, *Paranthropus aethiopicus*, *Homo habilis*, *Homo floresiensis*, *Homo ergaster*, *Homo erectus*, *Homo heidelbergensis*, *Homo neanderthalensis* and *Homo sapiens*. The number of specimens and age distribution for each taxon are reported in Table 3.5.2.

The study sample consists of a 3D landmark set acquired on:

- ✓ 3D model (CT-scan, laser scanner and photogrammetry);
- ✓ physical specimens using a Microscribe 3D (model G2X digitizer).

The cranial base morphology was captured through 17 landmarks distributed on occipital (basioccipital, exoccipital and condylar region) and temporal bones (petrous region), while 3 landmarks (prosthion, opistocranion and left orbital) were acquired to estimate the relative position of the foramen magnum along the median sagittal axis of the skull oriented along the Frankfurt plane (fig. 3.5.1 and Table 3.5.1).

In order to calculate the asymmetry, the rotated, translate and scaled configuration (after GPA) was obtained in each specimen. The landmark sets were symmetrized using the function `symmetrize` of the Morpho R package (Schlager, 2013). The Euclidean distance between each original and symmetrized landmark set has been calculated on order to estimate the asymmetry between the both sides.

The missing landmarks (Arbour and Brown, 2013) were estimated by deforming a complete sub-sample into deficient configuration.

The estimation is performed by a TPS calculated by a thin-plate-spline interpolation (iTPS) calculated on the basis of the landmarks available using the function `fixLMtps` of the R package Morpho (Schlager, 2013); in particular, the 10 configurations closest to the deficient specimen was used to estimate the missing landmark.

Table 3.5.1: List of landmarks used in the 3D analysis with label and definitions. Nos. 1:3, 11:15 are midline points. Nos. 4:10,16 are bilateral points and acquired on both sides.

No.	Label	Type	Landmark definition
			Landmark for shape analysis
1	sph	2	The point where the midsagittal plane intersects the basilar suture.
2	bas	2	The midline point on the anterior margin of the foramen magnum.
3	ops	2	The midline point at the posterior margin of the foramen magnum.
4	aba	2	The most anterior and lateral point on basilar part of occipital bone.
5	car	2	The closest point to PMS of carotid canal margin
6	jlp	2	The most lateral point on the jugular process.
7	aoc	2	The most superior point on the occipital condyle.
8	ioc	2	The most inferior point on the occipital condyle.
9	loc	2	The most lateral point on the occipital condyle.
10	por	2	The uppermost point on the margin of the external acoustic meatus.
			Other landmarks used in this study
11	ids	1	The midline point at the inferior tip of the bony septum between the upper central incisors.
12	opc	3	The midline ectocranial point at the farthest chord length from glabella.
13	nsp	2	The lowest point on the inferior margin of the nasal aperture as projected in the mid-sagittal plane
14	upr	2	Upper points on the piriform opening along the mid-sagittal plane
15	gla	2	The most forwardly projecting point in the mid-sagittal plane at the lower margin of the frontal bone, which lies above the nasal root and between the superciliary arches.
16	orb	2	The point at the lowest part of the orbital margin

Table 3.5.2: Number of specimens for each species with dental age stage (1: partial deciduous dentition; 2: complete deciduous dentition; 3: eruption of the only first molar tooth; 4: eruption of the only first two molar teeth; 5: complete permanent dentition).
Repository: Museum "G.Sergi", Dipartimento di Biologia Ambientale, Sapienza University of Rome;
Digital Morphology Museum, Kupri http://dmm.pri.kyoto-u.ac.jp/dmm/WebGallery/index.html; Nespos database https://www.nespos.org/display/EVANS/Home; Smithsonian Museum;
http://www.peterbrown-palaeoanthropology.net/.

Species	Age					
	cl. 1	cl. 2	cl. 3	cl. 4	cl. 5	TOT
Pan troglodytes	1	5	9	2	21	38
Gorilla gorilla	0	0	4	3	21	28
Pongo pygmaeus	0	2	4	6	5	17
Pongo abelii	0	0	5	1	11	17
Hylobates klossii	0	0	0	2	5	7
Hylobates agilis	0	0	0	3	20	23
Symphalangus sindactilus	0	2	1	1	11	15
Homo sapiens	2	4	4	1	20	31
Australopithecus afarensis	0	0	1	0	1	2
Paranthropus boisei	0	0	0	0	1	1
Homo habilis	0	0	0	0	1	1
Homo floresiensis	0	0	0	0	1	1
Homo ergaster	0	0	0	1	1	2
Homo erectus	0	0	0	0	1	1
Homo heidelbergensis	0	0	0	0	2	2
Homo neanderthalensis	0	0	1	0	2	3

The most critical deficient configuration is that of the "Taung's Child" in fact, in a first stage was carried a landmark-based alignment of the neurocranial/endocast portion with that of the face. The second stage consists in the mirroring of the right-side on left-side (Gunz, et al., 2009). Therefore, the specimen, thus constructed, includes 12 of 17 landmark; the deficient configuration was completed using the first 10 specimens with a Procrustes distances more close to the original configuration.

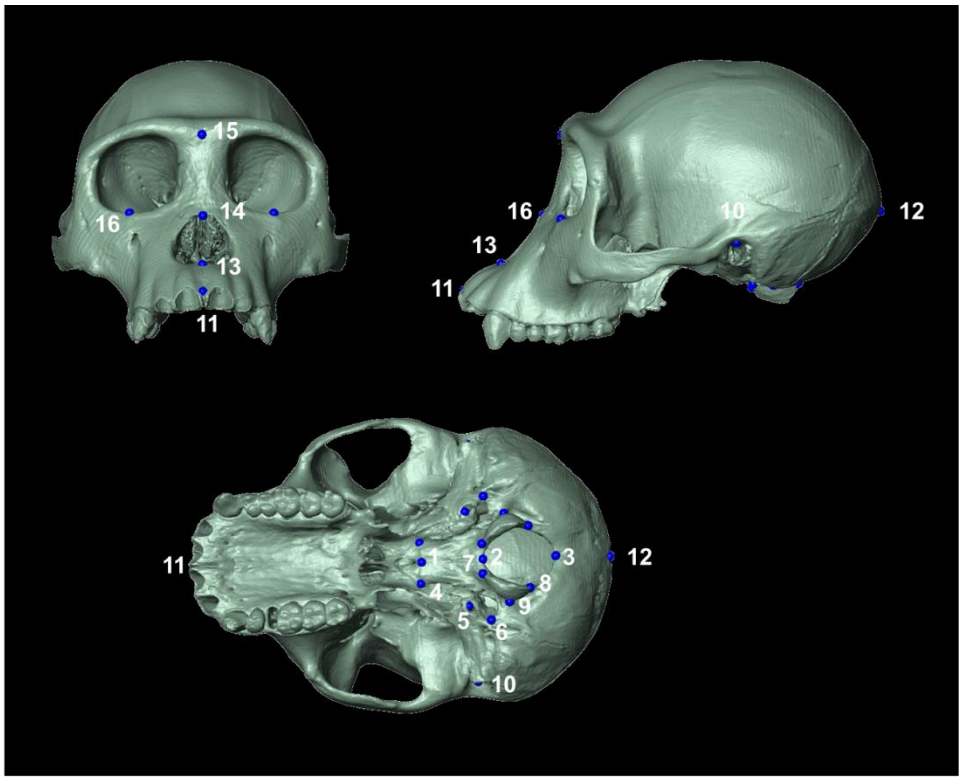

Figure 3.5.1 List numbered of landmarks used in this study on a specimen of *Pan troglodytes*. Nos. 1:3, 11:15 are midline points. Nos. 4:10,16 are bilateral points and acquired on both sides.

The projections of the landmarks prosthion, basion, opisthion and opistocranion on the Frankfurt plane were calculated to obtain information about the position of the foramen magnum along the skull. These configurations were scaled on a unit length and the position of the central point of the foramen magnum was acquired for each specimen (CFM); in this way, each configuration landmark was converted to a 2D-configuration using the Frankfurt plane as a reference plane. In order to confirms the data reported as boxplots has been tested the differences from the different locomotory habits using a Wilcoxon test (Wilcoxon and Wilcox, 1964)

This variable (CFM) was used in a multivariate regression analysis with the values of the Principal Component Scores (PCs) to evaluate the relationship between the morphology of the cranial base and the relative position of the foramen magnum.

A multiple regression analysis of the CS (CS log) on the PCs was executed to investigate the morphological changes, for each species, in relation to the growth. Has been performed the regression of the size on shape using the entire study sample and the only adult sub-sample (eruption of 3rd molar). Furthermore, the regression analysis on the entire sample was carried out respectively on the full data and on a species-pooled sample. In the latter case, the regression of the size was performed on the value of the PC scores corresponding one by one to the species *Homo sapiens*, *Pan troglodytes*, *Gorilla gorilla*, *Pongo pygmaeus* and *Pongo abelii*.

A quantification of the phylogenetic signal was performed on the PC scores, CS and

```
library("ctrlR")
data("FM.position")
Arr_pos_FM=array(NA,dim=c(5,2,dim(Hom.FM.position)[3]))
for(i in 1:dim(Hom.FM.position)[3]){
proj=points2plane(Hom.FM.position[,,i], v1=Hom.FM.position[5,,i],
normal = NULL, v2 = Hom.FM.position[6,,i], v3 =
Hom.FM.position[7,,i])
  FMm=(proj[2,]+proj[3,])/2
  OP_PR=sqrt(sum(proj[4,]-proj[1,])^2)
  OP_BS=sqrt(sum(proj[4,]-proj[2,])^2)
  OP_OS=sqrt(sum(proj[4,]-proj[3,])^2)
  OP_FM=sqrt(sum(proj[4,]-FMm)^2)
  dis_OP_PR=100
  dis_OP_BS=(100*OP_BS)/OP_PR
  dis_OP_OS=(100*OP_OS)/OP_PR
  dis_OP_FM=(100*OP_FM)/OP_PR
  coo_op=c(0,0)
  coo_pr=c(100,0)
  coo_bs=c(dis_OP_BS,0)
  coo_os=c(dis_OP_OS,0)
  coo_fm=c(dis_OP_FM,0)
  coo_tot=rbind(coo_op,coo_os,coo_fm,coo_bs,coo_pr)
  names=c("Ops","Opi","FMm","Bas","Pro")
  Arr_pos_FM[,,i]=coo_tot
}
dimnames(Arr_pos_FM)[[3]]=substr(dimnames(Hom.FM.position)[[3]],1,3)
```

CFM using only an adult average (for species) sub-sample (dental stage equals to 5) and the divergence time between treated species. The adult sub-sample was subject to GPA subsequently was calculated the mean shape for each species. The presence of the phylogenetic signal was tested on these sets obtained in this way.

The phylogenetic tree (fig. 3.5.2) tested is in this study was estimated from molecular data available on the 10KTrees website (Arnold, et al., 2010).

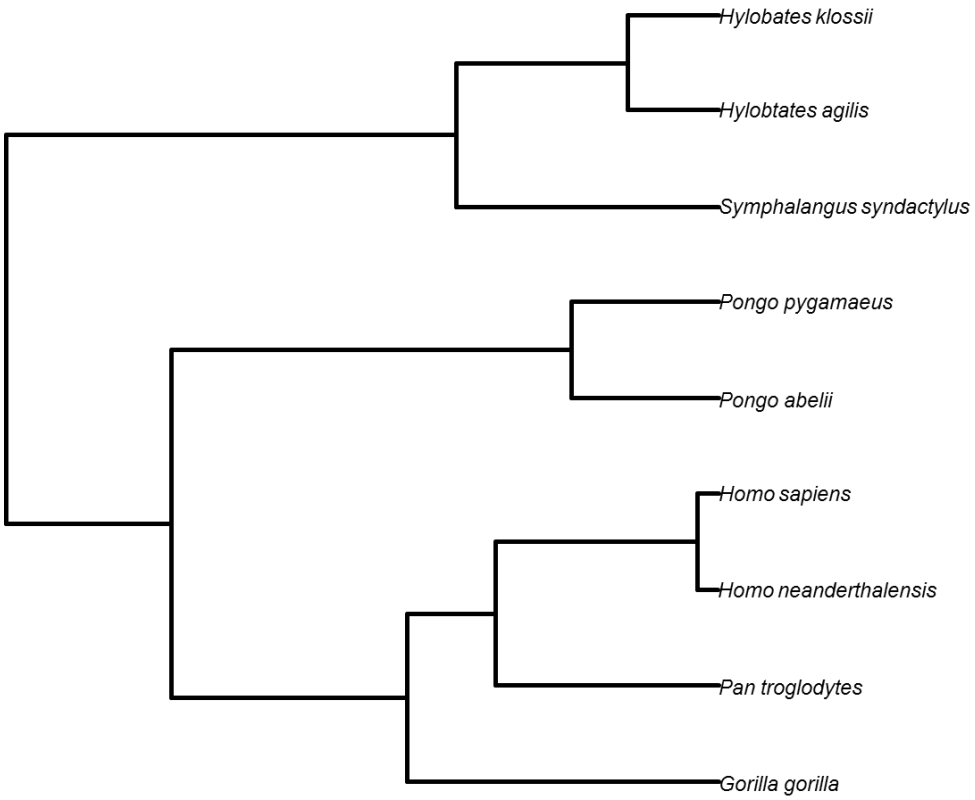

Figure 3.5.2: Phylogenetic tree tested in this study.

The Phylogenetically Independent Contrasts (PIC) was invented by Joe Felsenstein (1985). This method uses the phylogenetic information to transform the original tip into values statistically independent and identically distributed (contrasts). Therefore, the phylogenetic effect is removed from original data.

The PIC assumpions (Diaz-Uriarte and Garland, 1996, Garland, et al., 1993) are:

- ✓ correct topology;
- ✓ branch-lengths measured in units of expected variance of character evolution;
- ✓ Brownian motion model of character evolution.

Phylogenetic signal is the tendency of related species to resemble each other more than species drawn at random from the same tree. To test the phylogenetic signal in shape coordinates the consensus tree can be from molecular data available in dataset online (e.g., the 10kTrees project).

In GM, the two common methods to quantify the phylogenetical signal are the K statistics of Blomberg et al. (2003) and the Pagel's lambda (Pagel, 1993).

Often, through these methods, the presence of phylogenetic signal in univariate (e.g., CS) and multivariate variables (e.g., PCs) is tested.

The K statistic compares the variance observed with that of expected under Brownian motion (Blomberg, et al., 2003). Blomberg's K expresses the strength of phylogenetic signal as the ratio of the mean squared error of the tip data measured from the phylogenetic corrected mean and the mean squared error based on the variance–covariance matrix derived from the given phylogeny under the assumption of Brownian motion (Münkemüller, et al., 2012). In a case in which the similarity of trait values is well predicted by the phylogeny, the simulated evolution under Brownian motion will be small and thus the Blomberg's K large.

The Pagel's lambda is the multiplier of the off diagonal elements of the covariance matrix (Pagel, 1993, Pagel, 1999). Pagel's lambda returns a value corresponding to the comparison between the phylogenetic tree with the same without phylogenetic structure:

- ✓ Lambda equals to 0, lacking of phylogenetic correlation;
- ✓ Lambda equals to 1, full correlation with phylogenetic tree.

The test was carried out using the functions stored in R packages "geomorph" (Adams and Otárola-Castillo, 2005) and "phytools" (Revell, 2012). The phylogenetic signal was assessed using the "K" (Blomberg, et al., 2003) and "lambda" (Pagel, 1993) methods; the analyses were performed setting 1000 iterations among the tips of the phylogeny.

3.5.3 Foramen magnum position and allometry

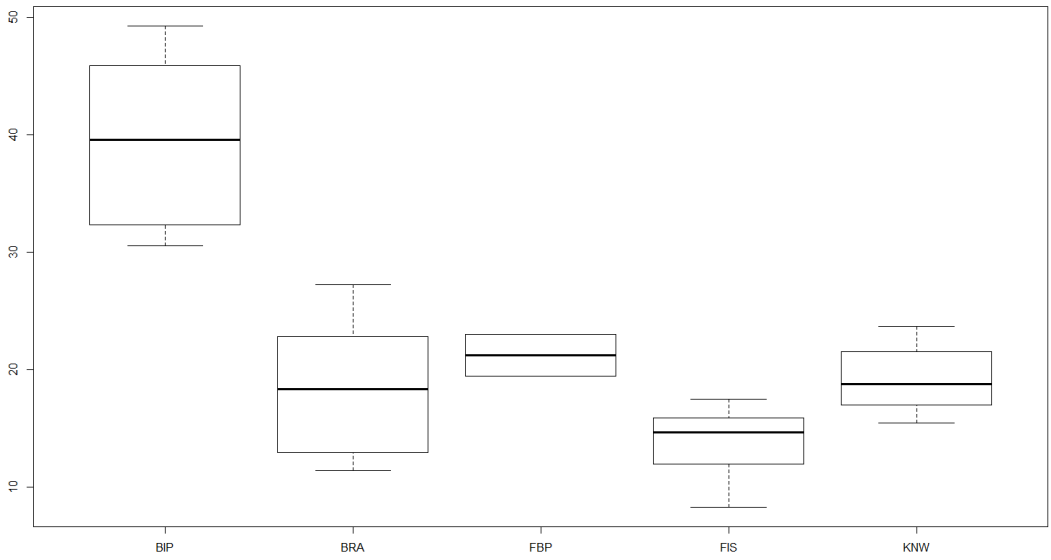

Figure 3.5.X: Boxplot of the values of CFM measured on the adult sample pooled by locomotor habits (BIP=bipedalism; BRA= brachiation; FBP=facultative bipedalism; FIS=fist-walking; KNW=knucke-walking).

Table 3.5.3: Results of the Wilcoxon test for the foramen magnum position performed between the different locomotory habits. The significant p-values (in bold) indicate the presence of statistically significant of the locomotory habits in relation to the position of the foramen magnum. KNW="Knuckle walking", FIS="Fist walking", BRA="Brachiation", FBP = "facultative bipedalism", BIP = "bipedalism".

	KNW	FIS	BRA	FBP	BIP
KNW	-				
FIS	**<0.01**	-			
BRA	0.78	**0.02**	-		
FBP	0.44	**0.03**	0.57	-	
BIP	**<0.01**	**<0.01**	**<0.01**	**0.02**	-

The Wilcoxon test (Table 3.5.3) highlights as the bipedalism (genus *Homo*) and fist walking (genus *Pongo*) locomotion results statistically significant from other locomotor habits, while the facultative bipedalism results not different from the locomotion associated to *Gorilla gorilla* and *Pan troglodytes*. The brachiation (Hylobatidae) and Knuckle walking results indistinguishable each other from the position of foramen magnum.

The output of the regressions of size (CS) on the shape for the adult-sub sample are reported in Table 3.5.4. The first two components of the PCA correlate with the CS variable. The same analyses performed on the all sample (including infants and juveniles

specimens) show a consistent correlation of the PC2 with the allometric factor (R squared equals to 0.60). When considering the single species, we found a significant and high allometric component on the genera *Pan*, *Gorilla* and *Pongo* in both PC1 and PC2. The correlation between CS and shape is statistically significant in *Homo sapiens* only for the PC1 (Table 3.5.4). In addition, a linear regression of CFM on CS was performed (Table 3.5.4). The variable CFM is statistically correlated with the variable CS.

Table 3.5.4: Output of the multivariate linear regression performed to test the effect of size and the position of foramen magnum on cranial base shape.

FM		
Adult sub-sample		
Variable	R squared	P-value
PC1	**0.66**	**<0.01**
PC2	0.005	0.40
PC3	0.011	0.21
PC4	-0.02	0.87
PC5	-0.0006	0.33
CS	0.05	0.05
Regression by OTU on Adult sub-sample		
CS (*Hylobatidae*)	**0.70**	**<0.01**
CS (*Hominins*)	-0.07	0.53
CS (*Great Apes*)	-0.05	0.96
CS		
Adult sub-sample		
Variable	R squared	P-value
PC1	**0.16**	**<0.01**
PC2	**0.44**	**<0.01**
PC3	<0.01	0.74
PC4	**0.07**	**<0.01**
PC5	0.03	0.03
All sample (including infants and juvenile)		
PC1	0.02	0.03
PC2	**0.60**	**<0.01**
PC3	0.12	0.07
PC4	0.01	0.11
PC5	0.02	0.04
Regression by species (from all sample)		
PC1 (*Pan troglodytes*)	**0.63**	**<0.01**
PC2 (*Pan troglodytes*)	**0.37**	**<0.01**
PC1 (*Homo sapiens*)	**0.27**	**<0.01**
PC2 (*Homo sapiens*)	0.05	0.11
PC1 (*Gorilla gorilla*)	**0.51**	**<0.01**
PC2 (*Gorilla gorilla*)	**0.50**	**<0.01**
PC1 (*Pongo pygmaeus*)	**0.58**	**<0.01**
PC2 (*Pongo pygmaeus*)	**0.57**	**<0.01**
PC1 (*Pongo abelii*)	**0.35**	**<0.01**
PC2 (*Pongo abelii*)	**0.51**	**<0.01**

The figure 3.5.4 shows the boxplot for the value of the CS for the species considered in this study. It is clear that the district of the cranial base is larger in the genera *Homo*

(except *Homo floresiensis*) and *Gorilla*, while the species belonging to the taxon Hylobatidae present the lowest CS values.

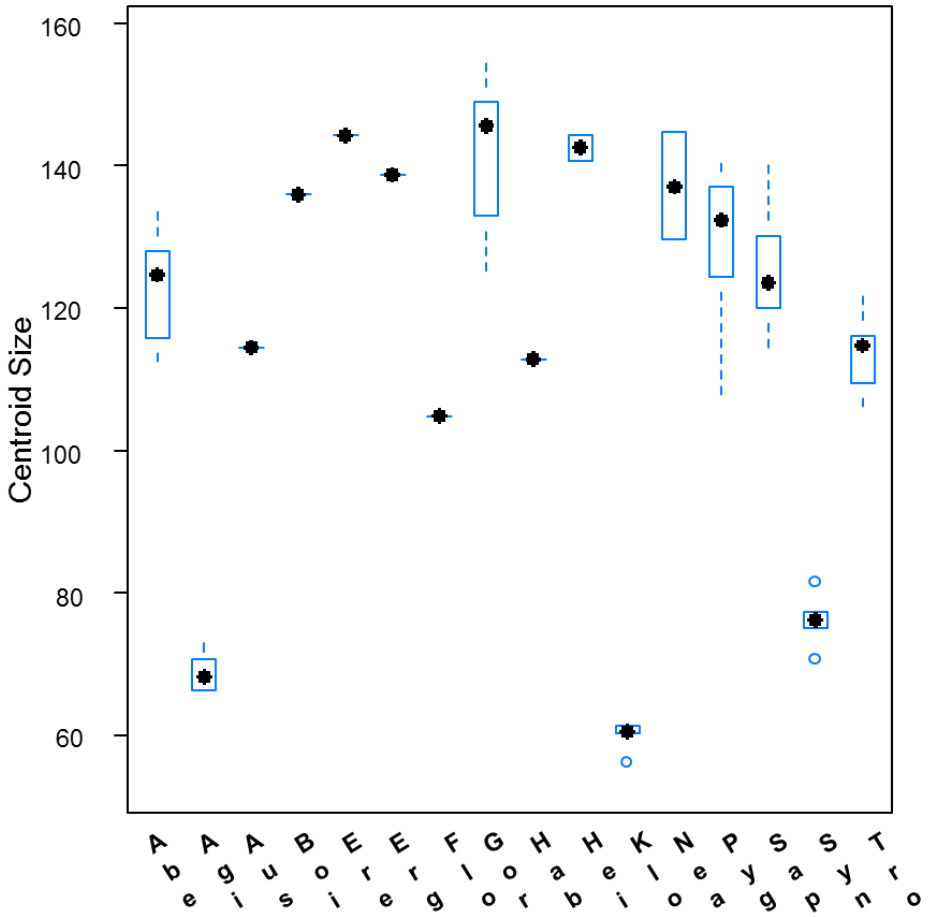

Figure 3.5.4: Boxplot of the Centroid Size of the cranial base species-pooled.

The correlation between this variable and phylogenetic information is statistically significant, as is shown by the fact that:

- Bloomberg's K for the CS variable is equal to 1.51 (p.value=<0.01; iterations=10000);
- Pagel's lambda is equal to 0.95 (p.value =<0.01; iterations= 10000);
- the log likehood confirms the previous result (logL= -38.48; logL1 = -43.17; logL0 = -35.34).

The function "contMap" (R package "phytools") has been used to plot (fig. 3.5.5) the average CS for species on the phylogenetic tree.

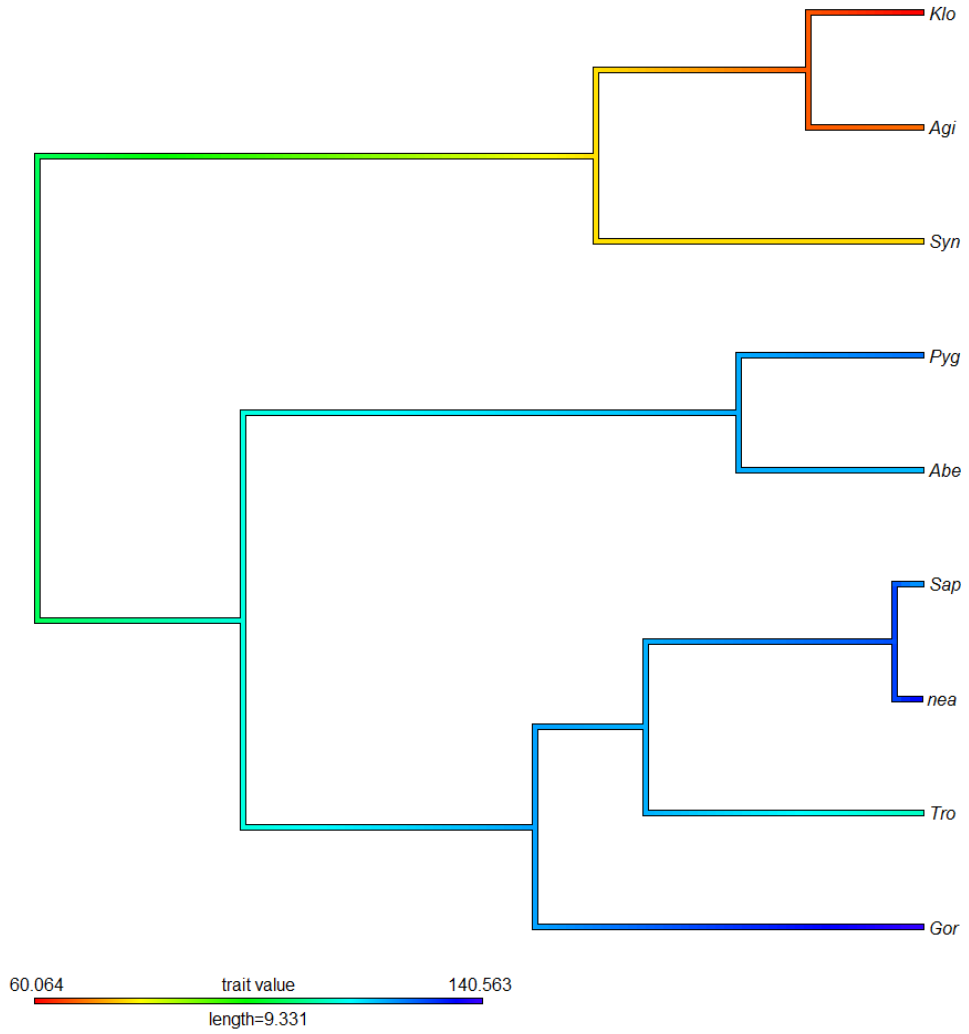

Figure 3.5.5: Plot of the variable Centroid Size on the phylogenetical tree.

The position index of the foramen magnum calculated on a pooled adult sub-sample species highlights:

- ✓ an advanced position of occipital foramen in the genus *Homo;*
- ✓ values for the genera *Australopithecus* and *Paranthropus* that are consistent with those observed in the genera *Pan* and *Gorilla*;
- ✓ the genera *Pongo* and *Symphalangus* present low values for the position of the foramen magnum.

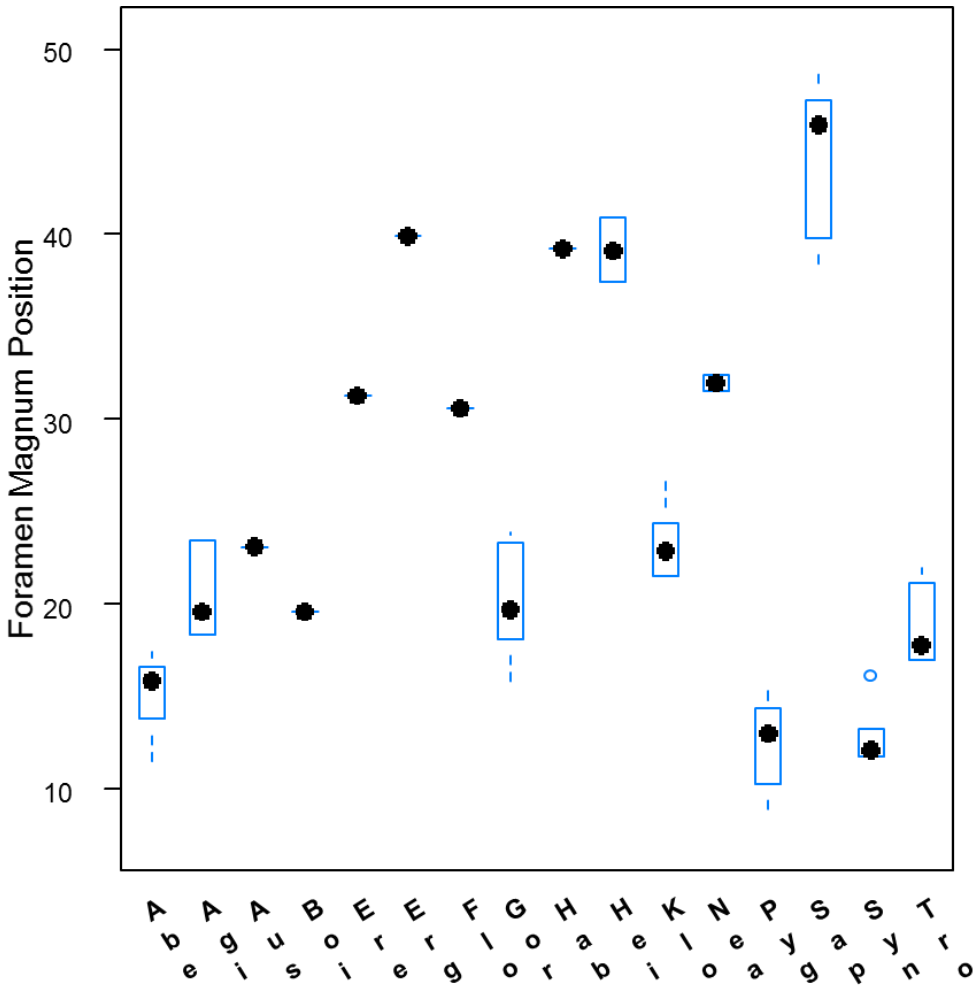

Figure 3.5.6: Boxplot of the foramen magnum positioning in the species considered in this study (only adults specimens).

Bloomberg's K (after 10000 iteration) is equal to 0.32 (p-value= 0.42); this result suggests the absence of correlation between the foramen magnum position and the phylogenetic component. This result is fully supported by the output of the phylogenetic signal performed using the "lambda" method (`phylosig` R function); in fact, Pagel's lambda is equal to 0.51 (p-value=0.56).

3.5.4 Shape analysis

The first two PCs accounted for about the 50% of the variation in the sample; the plot shown in figure 3.5.6 highlights the presence of two distinct trajectories. The first for the great Apes group with the adult specimens yielding a negative value of PC1 (31.79%) and slightly positive-neutral value of PC2 (15.39%). The wireframe used to display shape variations shows how the adult specimen of great Apes are characterized by a long and narrow basioccipital, a relatively small foramen magnum and a minor flexion of the basioccipital. The infant great Apes occupy a morpho-space of negative values for PC2 and neutral values for PC1, being characterized by the presence of a larger foramen magnum, a shorter basioccipital region, and the position of biporion line more closed to basion than the sub-sample of great Apes adult.

The three sampled species belonging to *Hylobatidae* yield mainly negative value for both first two PCs.

The *Homo sapiens* cluster is largely located around the positive value of PC1 and around the neutral value for PC2 with adult specimen on the positive value and the infant specimens on the negative value. The same pattern is present Middle-to-Late fossil Specimens (MLS). Therefore, we can state that the cranial base morphology in *Homo sapiens* and MLS (including LB1) are characterized by a flexed, short and large basioccipital and a broader foramen magnum; these shape pattern are more evident in infant specimens.

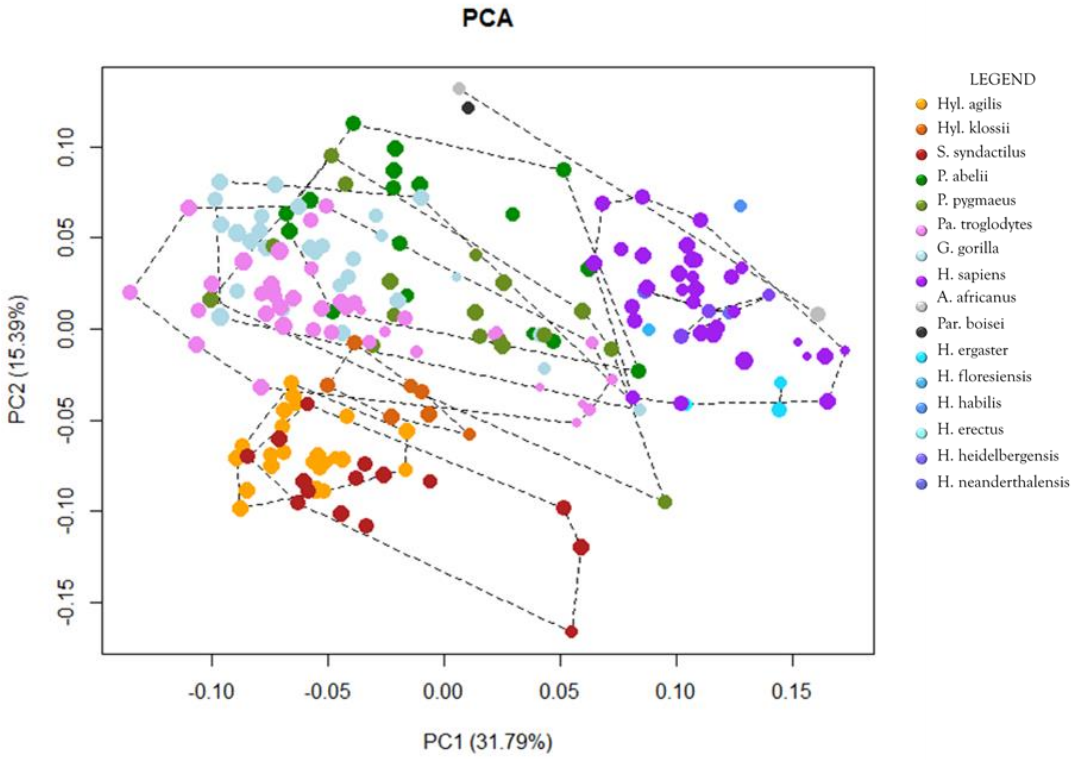

Figure 3.5.7: Plot of the first two Principal Components.

Adult specimens belong to early *Homo*, *Paranthropus* and *Australopithecus* that stand out from the *Homo sapiens* cluster because they are characterized by the presence of a large and moderately long basioccipital in association with a minor flexed basioccipital, a medium size of foramen magnum area and a moderately high value for the porion-jugular process-condylar angle.

All these shape features correspond to the extreme positive value for PC2. The estimated configurations for "Taung's child" fall closer to the infant bipedal Hominoidea than to the not bipedal.

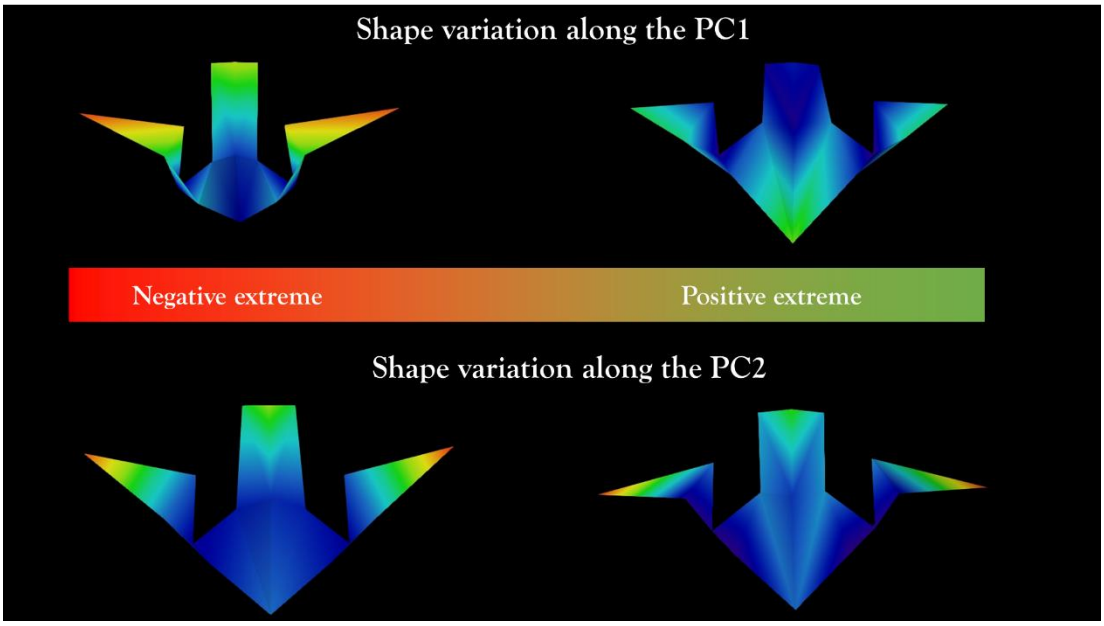

Figure 3.5.8: Shape variation associated to extremes value for PC1 (above) and PC2 (below). The false colours (rainbow palette) are associated to the mesh distances of the extremes values of the first two Principal Components to the mean shape: from blue to red respectively for null and maximum mesh distance.

As described above, a quantification of phylogenetic signal was performed by calculating Bloomberg's K and Pagel's lambda for the overall shape (all the PCs) and for the first five components (Tab. 3.5.5).

Table 3.5.5: Detailed results of phylogenetic signal. Are reported the values of Bloomberg's K, Pagel's λ, the log-likelihood, the log-likelihood for λ=0 and the log-likelihood for λ=1.

Variable	K	p-value (K)	Lambda	p-value (λ)	logL	logL0	logL1
CFM	0.32	0.42	0.51	0.56	-- 33.06	-33.23	-32.97
CS	1.51	0.08	0.95	<0.01	-38.48	-43.17	-35.34
Shape	0.34	0.13					
PC1	0.85	0.05	0.95	<0.01	-38.48	-43.17	10.91
PC2	0.86	0.02	0.95	0.05	16.10	14.11	13.38
PC3	0.10	0.90	6.61e^-5	1	23.61	23.61	13.33
PC4	0.10	0.91	6.61e^-5	1	24.69	24.69	13.87
PC5	0.13	0.81	6.61e^-5	1	24.30	24.30	14.76

3.5.5 Variation partitioning

Therefore, in addition to analyses previously described, in this study have been used the variation partitioning (Desdevises, et al., 2003). This method divides the total variation

of a dependent variable into two or more sets of explanatory. The variation partitioning involve a number of linear regressions followed by subtractions. In this analysis the shape of the cranial base, intended as the PC scores calculated after PCA performed on a sub-sample of only adult specimens. The PC scores has been averaged across the assessed species. The variable CS was calculated on the configuration landmark (N=17) used for the shape analysis; the phylogenetic variable consists in the first component of the scores of a Principal Coordinates Analysis after obtaining a distance matrix (patristic distances) from the tips of the phylogenetic tree (Raia, et al., 2010).

We studied the partitioning of the cranial base shape variation for three independent variables (fig. 3.5.9): the CS of the cranial base, the phylogeny and the position of the foramen magnum. Have been performed 7 linear regression of the dependent variable (shape intended as the matrix of PC scores) on FMP, CS, and phylogeny, and their multiple combinations. Each of these regressions produced a portion of the total variation explained by the independent variable. In this way have been obtained the values of variation explained by each independent variable (or their combinations) with respective statistically significance (Table 3.5.5).

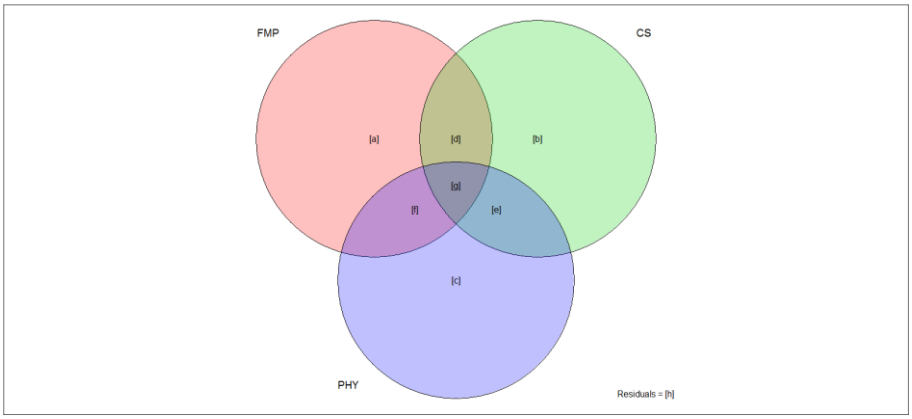

Figure 3.5.9: Schematic depiction of the three factors analyzed in partition variation meant to illustrate both their individual contribution to shape variance (i.e., fractions a, b, and c) and their interacting components.

Table 3.5.5: Results of partition variation analyses.

Partition table				
	Df	R.square	Adj.R.square	p-value
[a+d+f+g] = FMP	1	0.37	0.28	0.027
[b+d+e+g]= CS	1	0.16	0.04	0.245
[c+e+f+g]= PHY	1	0.24	0.13	0.092
[a+b+d+e+f+g]=FMP+CS	2	0.50	0.34	0.033
[a+c+d+e+f+g]=FMP+PHY	2	0.56	0.42	0.013
[b+c+d+e+f+g]=CS+PHY	2	0.41	0.21	0.188
[a+b+c+d+e+f+g]=FMP+CS+OTU	3	0.67	0.47	0.004
[a]= ”pure” FMP	1	0.26	0.25	0.069
[b]= ”pure” CS	1	0.10	0.05	0.206
[c]= ”pure” PHY	1	0.16	0.13	0.063
[d]			0.03	
[e]			0.01	
[f]			0.05	
[e]			-0.05	
[h]=Residuals			0.53	

The “pure” effect independent variables are 25.0%, 5.0% and 1.3% respectively for the FMP, CS and PHY (independent variable). The total contribution of FMP is the 28.0% of cranial base shape and it is statistically significant. In addition, the CS and PHY (not statistically significant) explain the 3% 14% respectively.

4. Discussion

Recent advances in 3D model digital acquisition techniques (e.g., CT scan, laser scanner and photogrammetry) have led to an increase in virtual model production. In addition, the digitisation process has resulted in the establishment of scientific digital collections and the setting-up of virtual museums (e.g., Kupri museum, Morphosource, Digimorph, Smithsonian museum).

Topological artefacts due to digital acquisition have been often corrected through the application of smoothing filter (e.g., Guskov and Wood, 2001, Wood, et al., 2002).

This thesis highlights the detrimental effects that a surface undergoes when smoothing is applied without any specific criteria. Any excessive iteration can generate a loss of information which may be remarkable: without a high-resolution surface acting as a reference for comparisons, the recovery of anatomical information through smoothing cannot be assured. In this case, the choice of the algorithm is a key step in the whole process and the setting of its parameters may be used to balance between faceting elimination and information recovery.

The assessment of a smoothing filter can be applied only in cases in which a higher resolution model is available (e.g., decimation). On the other hand, a decimation processing can be desirable to uniform the geometrical complexity of the sample study and is mandatory in specific analysis such as the Finite Element Analysis (e.g., Cirak, et al., 2000, Piras, et al., 2015).

The various examples provided are sufficient to show that the curvature of the anatomical region of interest is a factor of utmost importance, in accordance to Taubin (1995). Moreover, the smoothing procedure can also affects the size of the specimen, acting differently on different anatomical curvatures: this alteration is of greater importance when the anatomical district of interest is associated with small size variability (e.g. human teeth, inner ear structure).

When a high-resolution version of a specimen is not available, the best choice is to act with caution: few iterations of smoothing may be applied using "taubin", while other algorithms have to be used with extreme moderation, their effects being completely erratic; alternatively, one may not smooth at all: the data held by a low-resolution surface is still information coming from the real object, while smoothing inevitably transforms it to an unpredictable extent. In addition, the scale dependent algorithms (i.e., "angWeight" and "FujiLaplace") may drastically change the topological structure of a 3D model subjected to smoothing, and in this case the only way to apply these algorithm is by using the smoothing tool.

When a high-resolution reference is available for the specimen of interest, an empirical approach should be preferred over the guidelines proposed here. The comparison between the reference and the smoothed low-resolution/simplified surfaces can be used to identify the algorithm and the settings resulting in the highest information recovery possible. The tool described here is specifically conceived for this purpose. It works in

R and requires a reference surface in its low-resolution/simplified version: the desired level of simplification can be attained by directly using the functions provided in the tool; one landmark set and one semilandmark set are also needed. The analyses work automatically and the output is a specimen with the maximal recovery (or the minimal loss) of information: the level of decimation, the algorithm used, the parameters setting and the iteration of smoothing are returned.

GM is currently applied to highly detailed anatomical structures, often extracted through manual segmentation (e.g. ear ossicles, brain endocasts) and many different fields are benefiting from the spread of virtual imaging techniques, ranging from palaeontology and anatomy to engineering and medical science. The delicate questions addressed by these fields of research require a considerable amount of attention on how the data are generated and each step of the virtual imaging needs to be standardised. Since the smoothing of surfaces may cause the information of a specimen to be reduced considerably, further research should be focused on understanding the features which are most likely to be affected: these studies should take into account the geometry of the object itself and how different geometries are related to optimal levels of smoothing. In addition, future research may try to improve the steps of virtual acquisition and rendering, for example working on the isosurface algorithm (Livnat, et al., 1996), in order to solve the problems due to faceting and thus make the application of smoothing unessential.

Another advantage of the digital acquisition procedure is the possibility to restore the original shape of a damaged specimen. In the last decade, this procedure has been applied on numerous occasion to repair damaged fossil specimens (e.g., Amano, et al., 2015, Gunz, et al., 2009, Ponce De León and Zollikofer, 1999, Zollikofer, et al., 2005). Different methods (e.g., Gunz, et al., 2009, Kikuchi and Ogihara, 2013, Tallman, et al., 2014) of digital operations can be used to restore the original shape of the specimen, before it was altered by damage and distortion due to post-depositional process. No nomenclature has yet been proposed to discriminate between commonly used methods. In the subchapter 2.3 a distinction is proposed between the terms reconstruction and restoration. The term "reconstruction" could be used in all those case where the recovery of the specimen is computed with the insertion of "surface" not belonging to the fossil (e.g., from other specimen derived from TPS); the terms "restoration" is appropriate when the recovery of the original shape is achieved by using "parts" of the same specimen (e.g., retrodeformation, mirroring). A third type of surface recovery proposed in this thesis is the digital alignment, or the digital placement of portions of a specimen by means of a complete (or opportune) model as reference using the GM methods. A subtype of this procedure is that of mirroring by digital alignment when a deficient side (entirely or part of it) is recovered using the GM methods to mirror and place the preserved side to recover the missing morphology.

The procedure of retrodeformation was developed to correct the asymmetric between the right and left side, using a method called "symmetrization" (Bookstein and Mardia, 2003, Gunz, et al., 2009, Mardia, et al., 2000). Common protocols exploit the definition

of two sets of landmarks that are placed on either side. The landmark sets are reflected and relabelled to compute a symmetric average between the original and the mirrored landmark set; the 3D model is then warped to the landmark sets thus obtained with Thin-Plate-Spline (TPS) (Bookstein, 1989). The methodology developed thanks to the collaboration between the Laboratory of Palaeoanthropology and Bio-Archaeology (Sapienza University in Rome) and the University of Freiburg has been applied on the neanderthalian skull of Saccopastore 1. This method uses a denser bilateral cloud of points than other methods thanks to the introduction, besides the landmark set, of the curve and patch of semilandmark sets. This procedure involves symmetrisation, by TPS, of the 3D model through the definition of bilateral sets of points that are homologous from an anatomical or geometrical point of view. The model obtained in this way is perfectly symmetrical, and thus overcomes the distortion of anatomical asymmetry (fluctuant symmetry) (Savriama and Klingenberg, 2011) and post-depositional (taphonomic distortion) process.

Fossils deformed by taphonomic processes are recurrent in the fossil record, and usually being excluded from the sample (Arbour and Brown, 2013). Alternatively, some taphonomic alterations often simulate certain evolutionary changes, which can lead to errors in interpretation, such as the expansion of the wall during the encephalization process, placement of the foramen magnum and the flexion of the skull base (White, 2003).

In this thesis has been described the first application of the protocol of retrodeformation on the cranium of Saccopastore 1 using 88 bilateral landmark (44 on each side), 6 curves (140 semilandmarks) and 10 patches (438 semilandmarks), yielding a total of 666 anatomical/geometrical points (333 on each side). The output of the R function (stored in the Morpho package) (Schlager, 2013) returns a retrodeformed model of the neanderthalian skull of Saccopastore 1. The Euclidean distances of the corresponding landmarks of the "original" and "retrodeformed" versions of Saccopastore 1 ranged between 0.28 and 6.60 mm, thus highlighting the low rate of deformation recognisable in the 3D model. As a matter of fact, the principal axes of variation, due to taphonomic/biological processes, cross the region of the left parietal bone, portions of the mastoid region of the right temporal bone and part of the right side of the maxilla, suggesting that a phenomenon of compression occurred during post-depositional processes. Generally, the application of the retrodeformation algorithms make available those deformed specimens to GM analysis; finally, this protocol based on a denser cloud of landmarks allows more efficient retrodeformation.

An unquestionable advantage of digital acquisition is the physical preservation of the specimen. The acquisition by means of a CT-scan allows the full acquisition of the morphological information, thereby allowing the specimen to be subjected to other analyses whose invasive/destructive. In the case of the human fossil specimen of Pàus a first digital acquisition was performed using a medical computerized tomography at an interslice resolution of 0.6 mm, followed by a sample of "fossil powder" being taken (50

mg) for ancient DNA analysis. After the "fossil powder" sample, a micro-CT scan was perfomed to obtain a high-resolution model (voxel size of 41 μm). "Globally, the paleogenetic data indicate that in the sample is still detectable endogenous degraded ancient DNA, and that this DNA is from a Neanderthal" (Caramelli and Lari, 2015).

The morphology of Pàus analysed, both a semilandmark curve (21 landmark) and semilandmark (100 semilandmark) sets, it is intermediate between the variability range detected on *Homo neanderthalensis* and *Homo heidelbergensis* variability. The neanderthalian specimens closest to Pàus are those of Amud, Shanidar 1 and Tabun, which are representatives of an archaic morphotype of this species (e.g., absence of occipital bun) but are different from the Wurmian European sample characterized by a derivate morphology. The shape variation associated with the morphology of Pàus is compatible with that of Neanderthal as regards the morphology of the supratoral depression and the fronto-temporal constriction, respectively, while the morphology of the frontal bulging in the middle trait is intermediate between the information observed in *Homo neanderthalensis* and *Homo heidelbergensis*. While waiting for the study on dating, and considering that Pàus was found more closely to the Alpine moraines relative to Wurm and Riss glaciation, it is likely that this specimen lived in an interglacial period: Riss-Wurm (MIS5e) or in the Mindel-Riss (MIS7).

Another case of a morphological study of a human fossil specimen included in this thesis is that of Melka Kunture. The cranial fragments from Gombore II, dating about 850 ka, consist in an extraordinary human fossil record that is the only one found between 900 and 600 ka in Africa. Unfortunately, despite the large size of the cranial fragments, only an anatomical landmark on MK1 (the *lambda*) and MK2 (the *fronto-temporo-malar*) are recognisable on the exocranial surface. For this reason has been excluded a traditional GM approach (landmark-based), opting instead for the acquisition of two sets of evenly-spaced semilandmark. The semilandmark sets were deficient in MK1 and MK2 owing to the lack of the *stefanion* and *bregma* landmarks; we simulated 5 curve sets of the midsagittal profile (ranged between the *lambda* and *bregma*) and 2 curve sets of the inferior temporal lines (between the landmarks *fronto-temporo-malar* and *stefanion*). Since all the curves obtained in this way would include some semilandmark sets that are more likely than others, we preferred to analyse the raw geometry without introducing a sliding procedure; it should be remembered that under no circumstances did obtained the real configuration of curves acquired on the cranial fragments of MK1 and MK2.

Our analysis supports the hypothesis that these distinct portions, probably belonging to the same heavy cranium, demonstrate a morphology that is sufficiently distinct from *Homo ergaster*, despite the overlap of some features, and close to early representatives of African *Homo heidelbergensis*, particularly Kabwe 1 (or Broken Hill 1).

This conclusion is supported by the following points that emerge from the study of the cranial fragment MK1 and MK2:

- ✓ both the parietal MK1 and the frontal MK2 should be referred to the genus *Homo* and, when combined, represent a single cranium (MK cranium) whose various features point an "archaic" morphology, including the degree and shape of the curvature of both the sagittal and transversal profiles, the absence of the parietal foramen, the development of the obelic branch of the middle meningeal vessels, the temporal lines that along the parietal run medially to the parietal eminence, the marked the temporal lines on the frontal bone and the occurrence of a heavy frontal torus;
- ✓ peculiar features of the MK cranium are both the remarkable thickness of the cranial bones – which is unusual among African specimens either of *Homo ergaster* or *Homo heidelbergensis*, whereas it is in common with Ceprano– and the strong divergence of the temporal lines behind the postorbital constriction.
- ✓ it is rather obvious (but not without importance) that the MK cranium shows the greatest affinities with African demes (of both *Homo ergaster* and *Homo heidelbergensis*), while there are more clear distances with the Neanderthals and their European ancestors (HEU) as well as with *Homo sapiens* and, in part, with *Homo erectus*;
- ✓ the parietal MK1 exhibits curvature and shape of the midsagittal profile that approximates the *Homo ergaster* variability only when its arc length is elongated to values that are external to the same variability, whereas (given our estimation of the position of the bregma) it is closer to the field of variation of African *Homo heidelbergensis* for absolute dimensions, degree of the curvature and shape;
- ✓ MK1 has a strong and extended flattening of the obelic region on the external surface, very similar to that observed in Kabwe 1, and shows a marked depression of the endocast more laterally and anteriorly, where the thickness of the bone is higher than in other parts of the same parietal;
- ✓ the consequently flattened parietal lobe of the endocast, combined with the dominance of the more posterior branches of the middle meningeal network, is a further feature that is shared among archaic varieties of the genus *Homo* in general (Bruner, et al., 2015);
- ✓ in the frontal MK2, the shape of the inferior temporal line corresponds to the field of variability that is shared by *Homo ergaster* and early African *Homo heidelbergensis* (HA1);
- ✓ MK2 does not exhibit either an extended lateral wing of the frontal torus or a strong postorbital constriction.

MK1 and MK2 were aligned using a digital alignment after scaling of the landmark sets and the digital model belonging to Kabwe, using the parietal arc as scale factor (0.96). Following the same procedure, a restored virtual endocast of Kabwe was used as a

guideline to estimate the cranial capacity of the MK cranium, which was found around 1.080 cm3.

To sum up, we wish to point out that the morphology of the MK specimens fills the phenetic gap observed between *Homo ergaster* and *Homo heidelbergensis*. In view of the chronology of the human cranial bones from Gombore II, this conclusion appears of extreme interest, suggesting that such a partial cranium represents at present the best, if not the unique candidate for the ancestral occurrence of *Homo heidelbergensis* around 800 ka, as well as providing evidence that this species probably originated in Africa before its dispersal in Eurasia.

The last case study is on the cranial base morphology in the Hominoidea, in relation to phylogenetic, functional and allometric factors, using a large comparative sample consisting of 3D model obtained by applying photogrammetry, laser scanner, CT-scan and Micro CT-scan.

The sample used in this study highlights that the cranial base serves as an optimal district to analyse adaptations to different locomotor habits and postural pattern within the superfamily of Hominoidea. Furthermore, a study sample composed by infant, juvenile and adult categories may shed light on some aspects concerning the evolution of bipedalism as well as on individual growth trajectories in the species being considered.The study of the morphology by means of PCA found the existence of two distinct groups: the first for the genus *Homo*, *Australopithecus* and *Paranthropus* (bipedal form), the second for non-bipedal species. The last group can be subdivided into one group containing the genera *Pan*, *Gorilla* and *Pongo* and another containing the Hylobatidae groups. We interpreted the existence of non-overlapped clusters in relation to different locomotor habits that lead to the evolution of a functional morphology. This assumption is confirmed by the result of the statistically significant linear regression performed between the CFM on the PC1. The positioning of foramen magnum acquired along the Frankfurt plane has been found to depend on postural and locomotor habits (e.g., Ahern, 2005, Dean and Wood, 1984, Luboga and Wood, 1990), especially when with the phylogenetic signal, while it emerged as a phylogenetic signal for the shape variable only on the first Principal Component. to distinguish bipedal from no bipedal forms (Russo and Kirk, 2013). The CS is correlated with the phylogenetical signal, while for what concern the shape variable only on the first Principal Component is detected a phylogenetical signal. The phylogenetic signal recorded on CS variable demonstrates a trend of increasing size for the cranial base district; these values probably due to the increase in body size during the evolution of the Hominoidea according to Smith and Cheverud (2002). Furthermore, the validity of Rensch's rule (Rensch, 1950) within Primates (Smith and Cheverud, 2002) has been demonstrated. Besides sexual dimorphism, an increase in body size in Hominoidea may be due to a change above all in locomotor habits, as the fact that terrestrial Primates are usually larger than ones arboreal ones (Fleagle, 1999). As far as the intraspecific allometry is concerned, we observed that trajectories were stressed to a greater extent in the genera *Pongo*, *Gorilla* and *Pan* than species *Homo sapiens*. In addition, the slopes of the CS regressions on the PC

scores for the single species are higher in the Great Apes than in *Homo sapiens*. The position in the PCA of Taung Child's is close to the cluster of *Homo sapiens*, thus suggesting that the (probably) allometric trajectories of Australopithecus are parallel to those of *Homo sapiens* but more marked (due to ontogenetic changes). The results of variation partitioning show how the cranial base district is strongly influenced by many variables. The most evident result is the effect of the phylogenetic component that describes 13% of the cranial base shape, while the positioning of the foramen magnum explains 28% of the morphological variation. The phylogenetic signal identified for the variable CS and CFM is perfectly compatible with the results of the variation partitioning, indeed, the evolution of the Hominoidea was accompanied by a general increase in body size (Lindenfors and Tullberg, 1998, Smith and Cheverud, 2002) that influenced the type of locomotor habits adopted. Studies in the literature (e.g., Doran, 1997, Doran, 1992, Thorpe and Crompton, 2006) describe (as a percentage) the extent to which locomotion habits changed during ontogeny in the species *Gorilla gorilla* and *Pongo pygmaeus* as a consequence of the negative interference between CS and arboreal locomotion. Combining the result of the percentage explained by the "pure" effect of the CFM variable and the observed values in genera *Australopithecus* and *Paranthropus* suggests that caution should be taken when inferring locomotor habits (especially bipedalism) from the position of the foramen magnum alone. Combining the results of the linear regression to shape variation associated to extreme values of PC scores, the main differences between the morphology of the cranial base of a bipedal Hominoidea compared and a non-biped may be described as follows:

- ✓ large foramen magnum size;
- ✓ a shortened basioccipital;
- ✓ a different orientation of the occipital condyles;
- ✓ more advanced position of the foramen magnum (only in genus *Homo*).

BibliographyPrimary Sources

Secondary Sources

Uncategorized References

https://cran.r-project.org/.

https://github.com/Arothron/ctrlR.Profico/.

Abbate, E., Albianelli, A., Azzaroli, A., Benvenuti, M., Tesfamariam, B., Bruni, P., Cipriani, N., Clarke, R.J., Ficcarelli, G., Macchiarelli, R., 1998. A one-million-year-old Homo cranium from the Danakil (Afar) Depression of Eritrea, Nature 393, 458-460.

Abel, R.L., Parfitt, S., Ashton, N., Lewis, S.G., Scott, B., Stringer, C., 2011. Digital preservation and dissemination of ancient lithic technology with modern micro-CT, Computers & Graphics 35, 878-884.

Adams, D.C., Otárola-Castillo, E., 2005. geomorph: an R package for the collection and analysis of geometric morphometric shape data, Methods in Ecology and Evolution 4, 393-399.

Ahern, J.C.M., 2005. Foramen magnum position variation in Pan troglodytes, Plio-Pleistocene Hominids, and recent Homo sapiens: implications for recognizing the earliest Hominids, American Journal of Physical Antrhopology 127, 267-276.

Aiello, L., Dean, C., 1990. An Introduction to Human Evolutionary Anatomy, Academic Press, London.

Amano, H., Kikuchi, T., Morita, Y., Kondo, O., Suzuki, H., Ponce de León, M.S., Zollikofer, C.P., Bastir, M., Stringer, C., Ogihara, N., 2015. Virtual reconstruction of the Neanderthal Amud 1 cranium, American Journal of Physical Anthropology 158, 185-197.

Antón, S.C., 2012. Early *Homo*: Who, When, and Where, Current Anthropology 53, S278-S298.

Arbour, J.H., Brown, C.M., 2013. Incomplete specimens in geometric morphometrics analyses, Methods in Ecology and Evolution.

Arnold, C., Matthews, L.J., Nunn, C.L., 2010. The 10kTrees website: a new online resource for primate phylogeny, Evolutionary Anthropology: Issues, News, and Reviews 19, 114-118.

Arsuaga, J.L., Martınez, I., Gracia, A., Lorenzo, C., 1997. The Sima de los Huesos crania (Sierra de Atapuerca, Spain). A comparative study, Journal of Human Evolution 33, 219-281.

Arsuaga, J.L., Martínez, I., Arnold, L.J., Aranburu, A., Gracia-Téllez, A., Sharp, W.D., Quam, R.M., Falguères, C., Pantoja-Pérez, A., Bischoff, J., Poza-Rey, E., Parés, J.M., Carretero, J.M., Demuro, M., Lorenzo, C., Sala, N., Martinón-Torres, M., García, N., Alcázar de Velasco, A., Cuenca-Bescós, G., Gómez-Olivencia, A., Moreno, D., Pablos, A., Shen, C.C., Rodríguez, L., Ortega, A.I., García, R., Bonmatí, A., Bermúdez de Castro, J.M., Carbonell, E., 2014. Neandertal roots: Cranial and chronological evidence from Sima de los Huesos, Science 344, 1358-1363.

Arsuaga, J.L., Carretero, J.-M., Lorenzo, C., Gómez-Olivencia, A., Pablos, A., Rodríguez, L., García-González, R., Bonmatí, A., Quam, R.M., Pantoja-Pérez, A., Martínez, I.,

Aranburu, A., Gracia-Téllez, A., Poza-Rey, E., Sala, N., García, N., Alcázar de Velasco, A., Cuenca-Bescós, G., Bermúdez de Castro, J.M., Carbonell, E., 2015. Postcranial morphology of the middle Pleistocene humans from Sima de los Huesos, Spain, Proceedings of the National Academy of Sciences 112, 11524-11529.

Asfaw, B., Gilbert, W.H., Beyene, Y., Hart, W.K., Renne, P.R., WoldeGabriel, G., Vrba, E.S., White, T.D., 2002. Remains of Homo erectus from Bouri, Middle Awash, Ethiopia, Nature 416, 317-320.

Ashton, E.H., Zuckerman, S., 1956. Age changes in the position of the foramen magnum in hominoids, Proceedings of the Zoological Society of London, pp. 215-326.

Bade, R., Haase, J., Preim, B., 2006. Comparison of Fundamental Mesh Smoothing Algorithms for Medical Surface Models, SimVis, Citeseer, pp. 289-304.

Balter, M., 2014. RIP for a key *Homo* species?, Science 345, 129-129.

Bastir, M., Rosas, A., 2009. Mosaic Evolution of the Basicranium in *Homo* and its Relation to Modular Development, Evol Biol 36, 57-70.

Bastir, M., Rosas, A., Stringer, C., Cuétara, J.M., Kruszynski, R., Weber, G.W., Ross, C.F., Ravosa, M.J., 2010. Effects of brain and facial size on basicranial form in human and primate evolution, Journal of Human Evolution 58, 424-431.

Bastir, M., Rosas, A., Gunz, P., Peña-Melian, A., Manzi, G., Harvati, K., Kruszynski, R., Stringer, C., Hublin, J.J., 2011. Evolution of the base of the brain in highly encephalized human species, Nature Communication 2.

Bates, K., Falkingham, P., Rarity, F., Hodgetts, D., Purslow, A., Manning, P., 2010. Application of high-resolution laser scanning and photogrammetric techniques to data acquisition, analysis and interpretation in palaeontology, International Archives of the Photogrammetry, Remote Sensing, and Spatial Information Sciences, 68-73.

Benazzi, S., Coquerelle, M., Fiorenza, L., Bookstein, F., Katina, S., Kullmer, O., 2011. Comparison of dental measurement systems for taxonomic assignment of first molars, American journal of physical anthropology 144, 342-354.

Benazzi, S., Fornai, C., Buti, L., Toussaint, M., Mallegni, F., Ricci, S., Gruppioni, G., Weber, G.W., Condemi, S., Ronchitelli, A., 2012. Cervical and crown outline analysis of worn Neanderthal and modern human lower second deciduous molars, American journal of physical anthropology 149, 537-546.

Biegert, J., 1963. The evaluation of characteristics of the skull, hands and feet for primate taxonomy, Classification and human evolution, 116-145.

Blomberg, S.P., Garland Jr, T., Ives, A.R., Crespi, B., 2003. Testing for phylogenetic signal in comparative data: behavioral traits are more labile, Evolution 57, 717-745.

Bona, F., Corbetta, C., 2009. Mammalofaune quaternarie delle alluvioni del Po:(province di Cremona, Lodi, Piacenza e Parma); analisi paleontologica e ricostruzione paleoambientale, Provincia di Cremona.

Bonhomme, V., Picq, S., Gaucherel, C., Claude, J., 2014. Momocs: Outline Analysis Using R, Journal of Statistical Software 56, 1-24.

Bonnefille, R., 1972. Associations polliniques actuelles et quaternaires en Ethiopie (vallées de l'Awash et de l'Omo), Bonnefille.

Bookstein, F., Strauss, R., Humphries, J., Chernoff, B., Elder, R., Smith, G., 1982. A comment upon the uses of Fourier methods in systematics, Systematic Zoology, 85-92.

Bookstein, F.L., 1978. The measurement of biological shape and shape change, Springer, Berlin.

Bookstein, F.L., 1982. Multivariate discrimination by shape in relation to size, Systematic biology 30, 291-308.

Bookstein, F.L., 1989. Principal warps: Thin-plate splines and the decomposition of deformations, IEEE Transactions on Pattern Analysis & Machine Intelligence, 567-585.

Bookstein, F.L., 1997a. Landmark methods for forms without landmarks: morphometrics of group differences in outline shape, Medical image analysis 1, 225-243.

Bookstein, F.L., 1997b. Morphometric tools for landmark data geometry and biology, University Press, Cambridge.

Bookstein, F.L., Mardia, K.V., 2003. The five components of directional asymmetry, in: Aykroyd, R.G., Mardia, K.V. (Eds.), Stochastic Geometry, Biological Structure, and Images, Dept. of Statistics, University of Leeds, pp. 35-40.

Bookstein, F.L., 2005. After landmarks, in: Slice, D.E. (Ed.), Modern Morphometrics in Physical Anthropology, Kluwer Academic/Plenum Publishers, New York, pp. 49-71.

Breuil, H., Blanc, A.C., 1936. Le nouveau crâne néanderthalien de Saccopastore (Rome), Masson et Cie.

Brooks, R.A., Di Chiro, G., 1976. Beam hardening in x-ray reconstructive tomography, Physics in medicine and biology 21, 390.

Bruner, E., Manzi, G., 2006. Saccopastore 1: the earliest Neanderthal? A new look at an old cranium, Neanderthals revisited: new approaches and perspectives, Springer, pp. 23-36.

Bruner, E., 2007. Cranial shape and size variation in human evolution: structural and funcional perspectives, Child's nervous system 23, 1357-1365.

Bruner, E., Athreya, S., de la Cuétara, J.M., Marks, T., 2013. Geometric variation of the frontal squama in the genus Homo: frontal bulging and the origin of modern human morphology, American journal of physical anthropology 150, 313-323.

Bruner, E., Grimaud-Hervé, D., Wu, X., de la Cuétara, J.M., Holloway, R., 2015. A paleoneurological survey of Homo erectus endocranial metrics, Quaternary International 368, 80-87.

Caloi, L., Manzi, G., Palombo, M., 1998. Saccopastore, a stage-5-site within the city of Rome, SEQS Symposium (INQUASEQS'98)," The Eemian–Local sequeces, global perspectives"(Kerkrade, The Netherlands, September 1998), abstracts.

Caramelli, D., Lari, M., 2015.

Chavaillon, J., Brahimi, C., Coppens, Y., 1974. Première découverte d'hominidé dans l'un des sites acheuléens de Melka Kunturé (Ethiopie).

Chavaillon, J., Coppens, Y., 1975. Découverte d'Hominidé dans un site acheuléen de Melka-Kunturé, Bulletins et Mémoires de la Société d'Anthropologie de Paris 2, 125-128.

Chavaillon, J., 1979. Un site acheuléen près du lac Langano (Ethiopie) in Documents pour servir à l'Histoire de la Civilisation Ethiopienne, Documents pour servir à l'Histoire des Civilisations Ethiopiennes Paris, 57-74.

Chavaillon, J., Coppens, Y., 1986. Nouvelle découverte d'Homo erectus à Melka Kunturé (Ethiopie), Comptes rendus de l'Académie des sciences. Série 2, Mécanique, Physique, Chimie, Sciences de l'univers, Sciences de la Terre 303, 99-104.

Chavaillon, J., Berthelet, A., 2004. The archaeological sites of Melka Kunture, Studies on the Early Paleolithic site of Melka Kunture, Ethiopia. Origines, Firenze, 25-80.

Cirak, F., Ortiz, M., Schroder, P., 2000. Subdivision surfaces: a new paradigm for thin-shell finite-element analysis, International Journal for Numerical Methods in Engineering 47, 2039-2072.

Claude, J., 2008. Morphometrics with R.

Condemi, S., 1992. Les hommes fossiles de Saccopastore et leurs relations phylogénétiques, CNRS éditions.

Coppens, Y., 2004. The hominids of Melka Kunture. Some general reflections, Studies on the Early Paleolithic Site of Melka Kunture, Ethiopia. Origines, Istituto Italiano di Preistoria e Protostoria, Florence, 685-686.

Cunningham, D., 1909. XII.—The Evolution of the Eyebrow Region of the Forehead, with Special Reference to the Excessive Supraorbital Development in the Neanderthal Race, Transactions of the Royal Society of Edinburgh 46, 283-311.

Cunningham, J.A., Rahman, I.A., Lautenschlager, S., Rayfield, E.J., Donoghue, P.C.J., 2014. A virtual world of paleontology, Trends in Ecology & Evolution 29, 347-357.

Dart, R.A., 1925. Australopithecus africanus: the man-ape of South Africa, Nature 115, 195-199.

De Castro, J.M.B., Arsuaga, J.L., Carbonell, E., Rosas, A., Martìnez, I., Mosquera, M., 1997. A hominid from the Lower Pleistocene of Atapuerca, Spain: possible ancestor to Neandertals and modern humans, Science 276, 1392-1395.

de León, M.S.P., Zollikofer, C.P., 2001. Neanderthal cranial ontogeny and its implications for late hominid diversity, Nature 412, 534-538.

Dean, M.C., Wood, B.A., 1984. Phylogeny, neoteny and growth of the cranial base in Hominoids, Folia Primatologica 43, 157-180.

Desbrun, M., Meyer, M., Schröder, P., Barr, A.H., 1999. Implicit fairing of irregular meshes using diffusion and curvature flow, Proceedings of the 26th annual conference on Computer graphics and interactive techniques, ACM Press/Addison-Wesley Publishing Co., pp. 317-324.

Desdevises, Y., Legendre, P., Azouzi, L., Morand, S., 2003. Quantifying phylogenetically structured environmental variation, Evolution 57, 2647-2652.

Di Vincenzo, F., Bernardini, F., Biddittu, I., Profico, A., Zaio, P., Zanolli, C., Rubini, M., Tuniz, C., Manzi, G., 2014. The Ceprano calvarium, twenty years later. A new generation of (digital) studies, PESHE, 4, Florence, p. 61.

Diaz-Uriarte, R., Garland, T., 1996. Testing hypotheses of correlated evolution using phylogenetically independent contrasts: sensitivity to deviations from Brownian motion, Systematic Biology 45, 27-47.

Doran, D., 1997. Ontogeny of locomotion in mountain gorillas and chimpanzees, Journal of Human Evolution 32, 323-344.

Doran, D.M., 1992. The ontogeny of chimpanzee and pigmy chimpanzee locomotor behavior: a case study of paedomorphism and its behavioral correlates, Journal of Human Evolution 23, 139-157.

Edelsbrunner, H., Kirkpatrick, D.G., Seidel, R., 1983. On the shape of a set of points in the plane, IEEE Transactions on Information Theory 29, 551-559.

Endicott, P., Ho, S.Y.W., Stringer, C., 2010. Using genetic evidence to evaluate four palaeoanthropological hypotheses for the timing of Neanderthal and modern human origins, Journal of Human Evolution 59, 87-95.

Esteve-Altava, B., Boughner, J.C., Diogo, R., Villmoare, B.A., Rasskin-Gutman, D., 2015. Anatomical Network Analysis Shows Decoupling of Modular Lability and Complexity in the Evolution of the Primate Skull.

Falkingham, P.L., 2012. Acquisition of high resolution three-dimensional models using free, open-source, photogrammetric software, Palaeontologia Electronica 15, 15.

Felsenstein, J., 1985. Phylogenies and the comparative method, American Naturalist, 1-15.

Fleagle, J.G., 1999. Primate Adaptation and Evolution, Academic Press, London.

Forrest, A.R., 1972. Interactive interpolation and approximation by Bézier polynomials, The Computer Journal 15, 71-79.

Friess, M., Marcus, L.F., Reddy, D.P., Delson, E., 2002. The use of 3D laser scanning techniques for the morphometric analysis of human facial shape variation, BAR Int Series 1049, 31-35.

Friess, M., 2012. Scratching the Surface? The use of surface scanning in physical and paleoanthropology, Journal of Anthropological Sciences 90, 1-26.

Gallotti, R., Collina, C., Raynal, J.-P., Kieffer, G., Geraads, D., Piperno, M., 2010. The early Middle Pleistocene site of Gombore II (Melka Kunture, Upper Awash, Ethiopia) and the issue of Acheulean bifacial shaping strategies, African Archaeological Review 27, 291-322.

Garland, T., Dickerman, A.W., Janis, C.M., Jones, J.A., 1993. Phylogenetic analysis of covariance by computer simulation, Systematic Biology 42, 265-292.

Geraads, D., 1979. La faune des gisements de Melka-Konturé: artiodactyles, primates, Abbay X, 21-50.

Geraads, D., 1985. La faune des gisements de Melka Kunturé (Éthiopie), Colloque internat, Singer-Polignac, pp. 165-174.

Ghosh, D., Amenta, N., Kazhdan, M., 2010. Closed-form Blending of Local Symmetries, Computer Graphics Forum, Wiley Online Library, pp. 1681-1688.

Gilbert, W.H., Asfaw, B., 2008. Homo erectus: Pleistocene Evidence from the Middle Awash, Ethiopia, Univ of California Press.

Gilissen, E., 2009. Museum collections, scanning, and data access, Journal of Anthropologicl Science 87, 223-226.

Goswami, A., Polly, P.D., 2010. The influence of modularity on cranial morphological disparity in Carnivora and Primates (Mammalia), PLoS One 5, e9517-e9517.

Green, R.E., Krause, J., Ptak, S.E., Briggs, A.W., Ronan, M.T., Simons, J.F., Du, L., Egholm, M., Rothberg, J.M., Paunovic, M., Pääbo, S., 2008. Analysis of one million base pairs of Neanderthal DNA, Nature 444, 330-336.

Gunz, P., Mitteroecker, P., Bookstein, F.L., 2005. Semilandmarks in three dimensions, Modern morphometrics in physical anthropology, Springer, pp. 73-98.

Gunz, P., Mitteroecker, P., Neubauer, S., Weber, G.W., Bookstein, F.L., 2009. Principles for the virtual reconstruction of hominin crania, Journal of Human Evolution 57, 48-62.

Guskov, I., Wood, Z.J., 2001. Topological noise removal, 2001 Graphics Interface Proceedings: Ottawa, Canada, 19.

Harcourt-Smith, W.E., 2016. Early Hominin Diversity and the Emergence of the Genus Homo, Journal of Anthropological Sciences 94, in press.

Holloway, R.L., Broadfield, D.C., Yuan, M.S.-T., 2004. The Human Fossil Record: Brain Endocasts the Paleoneurological Evidence, Wiley-Liss, New York.

Howells, W., 1968. The cranium and maxillary dentition of australopithecus (Zinjanthropus) boisei. By PV Tobias. With a foreword by Sir WE LeGros Clark. Olduvai Gorge, ed. by LSB Leakey. Vol. 2. 264+ xvi pp., 39 text figures, 42 plates. $17.50 Cambridge Univ. Press, Wiley Online Library.

Jin, S., Lewis, R.R., West, D., 2005. A comparison of algorithms for vertex normal computation, The Visual Computer 21, 71-82.

Kaesler, R.L., Waters, J.A., 1972. Fourier analysis of the ostracode margin, Geological Society of America Bulletin 83, 1169-1178.

Kikuchi, T., Ogihara, N., 2013. Computerized assembly of neurocranial fragments based on surface extrapolation, Anthropological Science 121, 115-122.

Kimbel, W.H., Rak, Y., 2010. The cranial base of Australopithecus afarensis: new insights from the female skull, Philosophical Transactions of the Royal Society B: Biological Sciences 365, 3365-3376.

Kimbel, W.H., Suwa, G., Asfaw, B., Rak, Y., White, T.D., 2014. Ardipithcus ramidus and the evolution of the human cranial base, Proceedings of the National Academy of Sciences 111, 948-953.

Klingenberg, C.P., Barluenga, M., Meyer, A., 2002. Shape analysis of symmetric structures: quantifying variation among individuals and asymmetry, Evolution 56, 1909-1920.

Klingenberg, C.P., 2008. Morphological integration and developmental modularity, Annual review of ecology, evolution, and systematics, 115-132.

Kobbelt, L., Campagna, S., Seidel, H.-P., 1998. A general framework for mesh decimation, Graphics interface, pp. 43-50.

Krause, J., Fu, Q., Good, J.M., Viola, B., Shunkov, M.V., Derevianko, A.P., Pääbo, S., 2010. The complete mitochondrial DNA genome of an unknown hominin from southern Siberia, Nature 464, 894-897.

Kuhl, F.P., Giardina, C.R., 1982. Elliptic Fourier features of a closed contour, Computer graphics and image processing 18, 236-258.

Lieberman, D., 2011. The evolution of the human head, Harvard University Press.

Lindenfors, P., Tullberg, B.S., 1998. Phylogenetic analyses of primate size evolution: the consequences of sexual selection, Biological Journal of the Linnean Society 64, 413-447.

Livnat, Y., Shen, H.-W., Johnson, C.R., 1996. A near optimal isosurface extraction algorithm using the span space, Visualization and Computer Graphics, IEEE Transactions on 2, 73-84.

Luboga, G.G., Wood, B.A., 1990. Position and Orientation of the Foramen Magnum in Higher Primates, American Journal of Physical Anthropology 81, 67-76.

Lyman, R.L., 1994. Vertebrate taphonomy, Cambridge University Press.

Macchiarelli, R., Bondioli, L., Chech, M., Coppa, A., Fiore, I., Russom, R., Vecchi, F., Libsekal, Y., Rook, L., 2004. The late early Pleistocene human remains from Buia, Danakil depression, Eritrea, Rivista Italiana di Paleontologia e Stratigrafia 110, 133-144.

Macrini, T.E., De Muizon, C., Cifelli, R.L., Rowe, T., 2007. Digital cranial endocast of Pucadelphys andinus, a Paleocene metatherian, Journal of Vertebrate Paleontology 27, 99-107.

Manzi, G., Passarello, P., 1991. Anténéandertaliens et néandertaliens du Latium (Italie centrale), L'Anthropologie 95, 501-522.

Manzi, G., Bruner, E., Passarello, P., 2003. The one-million-year-old Homo cranium from Bouri (Ethiopia): a reconsideration of its H. erectus affinities, Journal of Human Evolution 44, 731-736.

Manzi, G., 2004. Human evolution at the Matuyama-Brunhes boundary, Evolutionary Anthropology: Issues, News, and Reviews 13, 11-24.

Manzi, G., 2012. On the trail of the genus Homo between archaic and derived morphologies, Journal of anthropological sciences= Rivista di antropologia: JASS/Istituto italiano di antropologia 90, 99-116.

Mardia, K.V., Bookstein, F.L., Moreton, I.J., 2000. Statistical assessment of bilateral symmetry of shapes, Biometrika, 285-300.

Mark, W.R., McMillan, L., Bishop, G., 1997. Post-rendering 3D warping, Proceedings of the 1997 symposium on Interactive 3D graphics, ACM, pp. 7-ff.

Marra, F., Ceruleo, P., Jicha, B., Pandolfi, L., Petronio, C., Salari, L., 2015. A new age within MIS 7 for the Homo neanderthalensis of Saccopastore in the glacio-eustatically forced sedimentary successions of the Aniene River Valley, Rome, Quaternary Science Reviews 129, 260-274.

Maslin, M.A., Ridgwell, A.J., 2005. Mid-Pleistocene revolution and the 'eccentricity myth', Geological Society, London, Special Publications 247, 19-34.

Mathys, A., Brecko, J., Semal, P., 2013. Comparing 3D digitizing technologies: what are the differences?, Digital Heritage International Congress (DigitalHeritage), 2013, IEEE, pp. 201-204.

Meindl, R.S., Lovejoy, C.O., 1985. Ectocranial suture closure: A revised method for the determination of skeletal age at death based on the lateral-anterior sutures, Am. J. Phys. Anthropol. 68, 57-66.

Meyer, M., Kircher, M., Gansauge, M.-T., Li, H., Racimo, F., Mallick, S., Schraiber, J.G., Jay, F., Prüfer, K., de Filippo, C., Sudmant, P.H., Alkan, C., Fu, Q., Do, R., Rohland, N.,

Arti Tandon, Siebauer, M., Green, R.E., Bryc, K., Briggs, A.W., Stenzel, U., Dabney, J., Shendure, J., Kitzman, J., Hammer, M.F., Shunkov, M.V., Derevianko, A.P., Patterson, N., Andrés, A.M., Eichler, E.E., Slatkin, M., Reich, D., Kelso, J., Pääbo, S., 2012. A high-coverage genome sequence from an archaic Denisovan individual, Science 338, 222-226.

Mitteroecker, P., Bookstein, F., 2008. The evolutionary role of modularity and integration in the hominoid cranium, Evolution 62, 943-958.

Morgan, L.E., Renne, P.R., Kieffer, G., Piperno, M., Gallotti, R., Raynal, J.-P., 2012. A chronological framework for a long and persistent archaeological record: Melka Kunture, Ethiopia, Journal of human evolution 62, 104-115.

Mounier, A., Condemi, S., Manzi, G., 2011. The stem species of our species: a place for the archaic human cranium from Ceprano, Italy, PloS One 6, e18821.

Mounier, A.l., Marchal, F.o., Condemi, S., 2009. Is *Homo heidelbergensis* a distinct species? New insight on the Mauer mandible, Journal of Human Evolution 56, 219-246.

Münkemüller, T., Lavergne, S., Bzeznik, B., Dray, S., Jombart, T., Schiffers, K., Thuiller, W., 2012. How to measure and test phylogenetic signal, Methods in Ecology and Evolution 3, 743-756.

Ni, X., Flynn, J.J., Wyss, A.R., 2012. Imaging the inner ear in fossil mammals: High-resolution CT scanning and 3-D virtual reconstructions, Palaeontol Electron 15, 1-10.

Niven, L., Steele, T.E., Finke, H., Gernat, T., Hublin, J.-J., 2009. Virtual skeletons: using a structured light scanner to create a 3D faunal comparative collection, Journal of Archaeological Science 36, 2018-2023.

Nomade, S.b., Muttoni, G., Guillou, H., Robin, E., Scardia, G., 2011. First 40 Ar/39 Ar age of the Ceprano man (central Italy), Quaternary Geochronology 6, 453-457.

Oakley, K.P., Campbell, B.G., Molleson, T.I., 1975. Catalogue of fossil hominids, British Museum (Natural History).

Ogihara, N., Nakatsukasa, M., Nakano, Y., Ishida, H., 2006. Computerized restoration of nonhomogeneous deformation of a fossil cranium based on bilateral symmetry, American journal of physical anthropology 130, 1-9.

Olsen, A., 2015. bezier: The bezier package is a toolkit for working with Bezier curves and splines. The package provides functions for point generation, arc length estimation, degree elevation and curve fitting., 1.1 ed., CRAN.

Pagel, M., 1993. Seeking the evolutionary regression coefficient: an analysis of what comparative methods measure, Journal of Theoretical Biology 164, 191-205.

Pagel, M., 1999. Inferring the historical patterns of biological evolution, Nature 401, 877-884.

Piras, P., Sansalone, G., Teresi, L., Moscato, M., Profico, A., Eng, R., Cox, T.C., Loy, A., Colangelo, P., Kotsakis, T., 2015. Digging adaptation in insectivorous subterranean eutherians. The enigma of Mesoscalops montanensis unveiled by geometric morphometrics and finite element analysis, Journal of morphology 276, 1157-1171.

Ponce De León, M.S., Zollikofer, C.P., 1999. New evidence from Le Moustier 1: Computer-assisted reconstruction and morphometry of the skull, The Anatomical Record 254, 474-489.

Potts, R., Behrensmeyer, A.K., Deino, A., Ditchfield, P., Clark, J., 2004. Small Mid-Pleistocene Hominin Associated with East African Acheulean Technology, Science 305, 75-78.

Profico, A., Veneziano, A., Lanteri, A., Manzi, G., 2014. Smoothing procedures in Geometric Morphometrics: a critical assessment, Proceedings of the European Society for the study of Human Evolution: Florence (Italy), 18-20 September 2014 3, 135.

Profico, A., Di Vincenzo, F., Bernardini, F., Caramelli, D., M., C., G., G., Martini, F., Persico, D., Ravara, S., Zanolli, C., Tuniz, C., Manzi, G., 2015. The hominin frontal bone recently discovered in the Po Valley, Northern Italy, Unravelling the Palaeolithic, Oxford, 22-23 April.

Profico, A., Veneziano, A., 2015. Arothron: R Functions for Geometric Morphometrics Analyses.

Raia, P., Carotenuto, F., Meloro, C., Piras, P., Pushkina, D., 2010. The shape of contention: adaptation, history, and contingency in ungulate mandibles, Evolution 64, 1489-1503.

Rensch, B., 1950. Die Abhängigkeit der relativen Sexualdifferenz von der Körpergrösse, Bonner Zoologische Beiträge 1, 58-69.

Revell, L.J., 2012. phytools: an R package for phylogenetic comparative biology (and other things), Methods in Ecology and Evolution 3, 217-223.

Rightmire, G.P., 1998. Human evolution in the Middle Pleistocene: The role of *Homo heidelbergensis*, Evol. Anthropol. 6, 218-227.

Rightmire, G.P., Lordkipanidze, D., Vekua, A., 2006. Anatomical descriptions, comparative studies and evolutionary significance of the hominin skulls from Dmanisi, Republic of Georgia, Journal of Human Evolution 50, 115-141.

Rightmire, G.P., 2008. Homo in the Middle Pleistocene: hypodigms, variation, and species recognition, Evolutionary Anthropology: Issues, News, and Reviews 17, 8-21.

Rightmire, G.P., 2009. Middle and later Pleistocene hominins in Africa and Southwest Asia, Proceedings of the National Academy of Sciences 106, 16046-16050.

Rohlf, F., 2010. tpsRelw, version 1.49. Department of Ecology and Evolution, State University of New York, Stony Brook, NY, USA.

Rohlf, F.J., Bookstein, F.L., 1990. Proceedings of the Michigan morphometrics workshop, University of Michigan Museum of Zoology.

Rohlf, F.J., 2015. The tps series of software, Hystrix 26.

Ross, C.F., 2013. Complexity, Modularity, and Integration in the Human Head. The Evolution of the Human Head, Journal of Human Evolution 1, 56-67.

Russo, G.A., Kirk, C.E., 2013. Foramen magnum position in bipedal mammals, Journal of Human Evolution 66, 656-670.

Saban, R., 1995. Image of the human fossil brain: endocranial casts and meningeal vessels in young and adult subjects, in: Changeux, J.-P., Chavaillon, J. (Eds.), Origins of the human brain, Oxford University Press, New York & Oxford pp. 11-41.

Santa Luca, A.P., 1978. A re-examination of presumed Neandertal-like fossils, Journal of Human Evolution 7, 619-636.

Savriama, Y., Klingenberg, C.P., 2011. Beyond bilateral symmetry: geometric morphometric methods for any type of symmetry, BMC evolutionary biology 11, 280.

Schlager, S., 2013. Morpho: Calculations and visualizations related to Geometric Morphometrics, R package version 0.23 3.

Schlager, S., 2014. Manipulations of Triangular Meshes Based on the VCGLIB API, R package version 0.10.1.

Schoetensack, O., 1908. Der unterkiefer des homo heidelbergensis: aus den sanden von mauer bei Heidelberg, W. Engelmann.

Schwartz, J.H., Tattersall, I., 2005. The human fossil record, craniodental morphology of genus *Homo* (Africa and Asia), John Wiley & Sons, New York.

Sergi, S., 1929. La Scoperta di un cranio del tipo di Neanderthal presso Roma, Società romana di antropologia.

Sergi, S., 1944. Craniometria e craniografia del prima paleoantropo di Saccopastore, Ricerche di Morfologia 20-21, 733-791.

Sergi, S., 1948. L'uomo di Saccopastore, Paleontographia Italica XLII, 25-164.

Shapiro, R., Robinson, F., 1976. Embryogenesis of the human occipital bone, American Journal of Roentgenology 126, 1063-1068.

Shipman, P., 1981. Life History of a Fossil and Introduction To Taphonomy and Paleoecology.

Singh, N., Harvati, K., Hublin, J.J., Klingenberg, C.P., 2012. Morphological evolution through integration: A quantitative study of cranial integration in *Homo*, *Pan*, *Gorilla* and *Pongo*, Journal of Human Evolution 62, 155-164.

Slizewski, A., Friess, M., Semal, P., 2010. Surface scanning of anthropological specimens: nominal-actual comparison with low cost laser scanner and high end fringe light projection surface scanning systems, Quartar 57, 179-187.

Smith, R.J., Cheverud, J.M., 2002. Scaling of sexual dimorphism in body mass: a phylogenetic analysis of Rensch's rule in primates, International Journal of Primatology 23, 1095-1135.

Stringer, C., 2012. The status of *Homo heidelbergensis* (Schoetensack 1908), Evol. Anthropol. 21, 101-107.

Tallman, M., Amenta, N., Delson, E., Frost, S.R., Ghosh, D., Klukkert, Z.S., Morrow, A., Sawyer, G.J., 2014. Evaluation of a New Method of Fossil Retrodeformation by Algorithmic Symmetrization: Crania of Papionins (Primates, Cercopithecidae) as a Test Case.

Tamrat, E., Thouveny, N., Taieb, M., Brugal, J.P., 2014. Magnetostratigraphic study of the Melka Kunture archaeological site (Ethiopia) and its chronological implications, Quaternary International 343, 5-16.

Taubin, G., 1995. Curve and surface smoothing without shrinkage, Computer Vision, 1995. Proceedings., Fifth International Conference on, IEEE, pp. 852-857.

Taubin, G., 2002. Dual mesh resampling, Graphical Models 64, 94-113.

Thorpe, S.K.S., Crompton, R.H., 2006. Orangutan Positional Behavior and the Nature of Arboreal Locomotion in Hominoidea, American Journal of Physical Anthropology 131, 384-401.

Urbanová, P., Hejna, P., Jurda, M., 2015. Testing photogrammetry-based techniques for three-dimensional surface documentation in forensic pathology, Forensic science international 250, 77-86.

Venables, W., Smith, D., 2010. the R Development Core Team.(2008) An Introduction to R, Network Theory Limited, Bristol.

Vollmer, J., Mencl, R., Mueller, H., 1999. Improved laplacian smoothing of noisy surface meshes, Computer Graphics Forum, Wiley Online Library, pp. 131-138.

Weber, G.W., 2001. Virtual anthropology (VA): a call for glasnost in paleoanthropology, The Anatomical Record 265, 193-201.

Weber, G.W., 2013. Another link between archaeology and anthropology: Virtual anthropology, Digital Applications in Archaeology and Cultural Heritage 1, 3-11.

Weber, G.W., 2014. Another link between archaeology and anthropology: virtual anthropology, Digital Applications in Archaeology and Cultural Heritage 1, 3-11.

Weidenreich, F., 1941. The brain and its role in the phylogenetic transformation of the human skull, Transactions of the American Philosophical Society 31, 321-442.

Weyrich, T., Pauly, M., Keiser, R., Heinzle, S., Scandella, S., Gross, M., 2004. Post-processing of scanned 3D surface data, Eurographics symposium on point-based graphics, pp. 85-94.

White, M.J., 1998. Twisted ovate bifaces in the British Lower Palaeolithic: some observations and implications, OXBOW MONOGRAPH, 98-104.

White, T., 2003. Early hominids--diversity or distortion?, Science 299, 1994.

Wilcoxon, F., Wilcox, R.A., 1964. Some rapid approximate statistical procedures, Lederle Laboratories.

Wood, Z., Hoppe, H., Desbrun, M., Schröder, P., 2002. Isosurface topology simplification, Microsoft Research MSR-TR-2002 28.

Zhou, T., Shimada, K., 2000. An Angle-Based Approach to Two-Dimensional Mesh Smoothing, IMR, pp. 373-384.

Zollikofer, C.P., de León, M.S.P., Lieberman, D.E., Guy, F., Pilbeam, D., Likius, A., Mackaye, H.T., Vignaud, P., Brunet, M., 2005. Virtual cranial reconstruction of Sahelanthropus tchadensis, Nature 434, 755-759.

Parts of subchapter 3.1 appear in:

Profico A., Veneziano A.,Lanteri A.,Manzi G., 2014. Smoothing procedures in Geometric Morphometrics: a critical assessment. In: Meeting della European Society for the study of Human Evolution. Proceedings of the European Society for the Study of Human Evolution, vol. 3, p. 135, ISSN: 2195-0776, Firenze, 18-20 settembre.

Profico A. & Veneziano A., 2015. Arothron: R Functions for Geometric Morphometrics Analyses. DOI 10.5281/zenodo.28194.

Parts of the subchapter 3.3 appear in:

Tuniz C., Bernardini F., Caramelli D., Cremaschi M., Di Vincenzo F., Galli C., Giacobini G., Gigli E., Lari M., Lo Vetro D., Martini F., Muscolino F., Persico D., Poggiani Keller R., **Profico A**., Ravara S., Ravazzi C., Zanolli C., Manzi G., 2014. Frontal bone of Neanderthal morphology recently discovered in the Po valley, northern Italy. Cell Symposium: Evolution of Modern Humans - From Bones to Genomes. March 16 - 18, 2014, Hotel Meliá, Sitges, Spain.

Profico A, Di Vincenzo F., Bernardini F., Caramelli D.,Cremaschi M.,Giacobini G.,Martini F.,Persico D., Ravara S.,Zanolli C.,Tuniz C.,Manzi G., 2015. Once in a while: the first non-modern human fossil specimen in the Po Valley (Cremona, Italy). In: Unravelling the Palaeolithic . Oxford, 22-23 April 2015

Manzi G., Bernardini F., Caramelli D, Cremaschi M., Di Vincenzo F.,Galli C.,Giabobini G., Gigli E., Lari M., Lo Vetro D., Martini F., Muscolino F., Persico D., Poggiani Keller R., **Profico A**, Ravara S., Ravazzi C., Zanolli C., Tuniz C., 2014. The hominin frontal bone recently discovered in the Po Valley, Northern Italy. Proceedings of the European Society for the Study of Human Evolution, ISSN: 2195-0776 ,Florence, 18-20 september.

Parts of the subchapter 3.4 appear in:

Profico A., Di Vincenzo F., Gagliardi L., Piperno M., Manzi G., 2016. Filling the gap. Human cranial remains from Gombore II (Melka Kunture, Ethiopia; ca. 850 ka) and the origin of Homo heidelbergensis. Journal of Anthropological Sciences, 94: 1-24.

Parts of the subchapter 3.5 appear in:

Profico A., Di Vincenzo F., Piras P., Di Chiara A., Manzi G., 2013. Morfologia della base del cranio: un confronto tra scimmie antropomorfe e ominini fossili. Museologia Scientifica e Naturalistica, 9(1): 97- 98.

Profico A., Di Vincenzo F., Piras P., Di Chiara A., Manzi G., 2013. Cranial base variations in extant Hominoidea and fossil Hominins. Proceeding of: III Annual European Society for the Study of Human Evolution, 78.

Profico A.,Di Vincenzo F.,Piras P.,Manzi G., 2014. An ontogenetic perspective on cranial base variations in extant Hominoidea and fossil Hominins. In: Atapuerca, XVII World UISPP Congress. Burgos, 1-7 September

Profico A., Buzi C., Landi F., Lattarini F., Veneziano A., Di Vincenzo F., Manzi. G., 2015. Morphological integration and modularity in the cranium of extant and fossil Hominoidea: a 3D geometric-morphometric approach. Proceedings of the European Society for the Study of Human Evolution, vol. 4, p. 181, ISSN: 2195-0776, London, 10-12 september.